Eidgenössische Technische Hochschule Zürich
Swiss Federal Institute of Technology Zurich

Increased Antihydrogen Production in GBAR towards a first Lamb-Shift Measurement in Antihydrogen

Master Thesis

Laurin Tim Koller
19-921-659

September 08, 2024

Advisors: Prof. P. Crivelli, Dr. C. Regenfus, P. Blumer
Department of Physics, ETH Zürich

Abstract

The GBAR experiment at CERN aims for precision measurements of gravitational effects on antihydrogen. Therefore, large numbers of antihydrogen atoms will be produced with a significant ratio in the $2S$ state, allowing for the determination of the antiproton charge radius by a precise determination of the $2S_{1/2} \rightarrow 2P_{1/2}$ Lamb shift of antihydrogen. First tests of the Lamb shift setup, consisting of an arrangement of two microwave chambers and a Lyman alpha detector to probe the transitions in the GHz range, were performed using a hydrogen beam created by a proton source and a thin carbon foil. The work described here extended these tests to more realistic experimental conditions in the GBAR apparatus using the H^- beam from CERN/ELENA, which has similar beam parameters as the antiproton beam. A clear signal from Lyman alpha photons with a statistical significance of 5.6 standard deviations can be seen when comparing microwave-off data to data with one of the microwave apparatuses set to the centre of the Lamb Shift transition 1060 MHz. From this signal, the detection efficiency of Lyman alpha photons was estimated to be roughly around $(4.12 \pm 1.60) \times 10^{-3}$. This detection efficiency was measured to be around 0.16 some years ago when the setup was new. The decline in the efficiency stems from deterioration of the ageing MCPs and damaged Cesium Iodide coating of the MCPs. There was also a quick measurement performed with the microwave system scanning over a frequency range to explore the lineshape of the transition, but no meaningful results could be achieved due to too large statistical fluctuations.

First estimations of the improved antihydrogen production at GBAR in 2024 were also made, and it was found that around 0.018 ± 0.008 antihydrogen are detected per $\overline{p}$ spill. This would be roughly a six-fold increase compared to 2022. A better determination of the $\overline{H}$ production rate is the main subject of the rest of the 2024 beam time, allowing for the further use of the data analysis code developed in this work. With the current numbers, a measurement of the Lamb shift of $\overline{H}$ in the 2024 beam time is not realistic, but plans exist to increase the antihydrogen production rate significantly over the next months. In addition, the detection efficiency of Lyman alpha photons will also be improved and a first detection of antihydrogen Lyman alpha photons is projected for 2025.

Contents

Contents ii

1 Introduction 1
- 1.1 Proton Charge Radius from Scattering Experiments . . . 1
- 1.2 Proton Charge Radius from Energy Level Measurements . . . 1
  - 1.2.1 Fine Structure of Hydrogen . . . 2
  - 1.2.2 Hyperfine Structure of Hydrogen . . . 2
- 1.3 Antiproton Charge Radius . . . 4

2 Setup of the Experiment 6
- 2.1 Positron Line . . . 6
  - 2.1.1 Positron Production [14] . . . 6
  - 2.1.2 Trapping of the Positrons [13] . . . 7
- 2.2 Antiproton Production and Cooling before the GBAR Experiment . . . 8
  - 2.2.1 Cooling of Antiprotons in the AD ring . . . 8
    - 2.2.1.1 Radiofrequency Cooling . . . 8
    - 2.2.1.2 Stochastic Cooling . . . 8
    - 2.2.1.3 Electron Cooling . . . 8
  - 2.2.2 Cooling in the ELENA Ring . . . 9
- 2.3 Antiproton Beam Line at the GBAR Experiment . . . 9
  - 2.3.1 Cooling of Antiprotons at the GBAR Experiment . . . 9
    - 2.3.1.1 Einzel Lens . . . 9
    - 2.3.1.2 Cooling the Beam in a Drift Tube . . . 10
    - 2.3.1.3 Reducing Beam Emittance with a Penning-Malmberg Trap 10
  - 2.3.2 Reaction Chamber . . . 11
  - 2.3.3 Lamb Shift Setup . . . 12
    - 2.3.3.1 Microwave Apparatus Setup and Circuit . . . 14
    - 2.3.3.2 Efficiency of the MWS at different Frequencies . . . 14
    - 2.3.3.3 Microchannel Plate Detector (MCP) . . . 15
  - 2.3.4 Beam Line after the Lamb Shift Setup . . . 16
- 2.4 Beam Line Modifications for a H^- Beam . . . 17

3 General Analysis Methods **18**
3.1 Error Estimations and Propagation . . . 18
3.2 Finding Clusters on MCP5 . . . 18

4 Carbon Foil **20**
4.1 Data used for the Carbon Foil Properties . . . 20
4.1.1 Carbon Foil Thickness . . . 20
4.1.2 Scattering on the Carbon Foil . . . 20
4.2 Analysis Methods for the Carbon Foil . . . 20
4.2.1 Carbon Foil Thickness . . . 20
4.2.2 Scattering on the Carbon Foil . . . 21
4.2.2.1 Scattering of low Energetic Particles on a thin foil using Meyer's Theory [33] . . . 21
4.2.2.2 Scattering obtained using the Scattering Constant from Allegrini [5] . . . 23
4.2.2.3 Distribution of the Particles on MCP5 . . . 24
4.3 Carbon foil Results . . . 25
4.3.1 Results for the Thickness of the Carbon Foil . . . 25
4.3.2 Results for the Scattering on the Carbon Foil . . . 26
4.3.2.1 Scattering obtained using Meyer's Theory [33] . . . 26
4.3.2.2 Scattering obtained using the Scattering Constant from Allegrini [5] . . . 27
4.3.2.3 Faults and Gain Map of MCP5 . . . 28
4.3.2.4 Distribution of the Particles on MCP5 . . . 30
4.4 Discussion of the Carbon Foil Properties . . . 31
4.4.1 Carbon Foil Thickness . . . 31
4.4.2 Scattering on the Carbon Foil . . . 31

5 Lamb Shift Setup Tests **34**
5.1 Datasets from the Lamb Shift Setup . . . 34
5.1.1 Microwave on/off Dataset (Dataset 1) . . . 34
5.1.2 First Microwave Scanning Dataset (Dataset 2) . . . 35
5.1.3 Second Microwave Scanning Dataset (Dataset 3) . . . 35
5.1.4 Data for the LEDs in front of the Lyman Alpha Detector . . . 36
5.2 Lamb Shift Data Analysis Methods . . . 37
5.2.1 Determining the Voltage Pulses in the Lyman Alpha MCPs . . . 37
5.2.1.1 Ringing in the MCP Voltages from Particle Impacts . . . 37
5.2.1.2 Distinguishing Pulses with a lot of Background . . . 38
5.2.1.3 Final Determination of the Voltage Pulses . . . 39
5.2.2 Analysis of the Signals on the Lyman Alpha MCPs from the LEDs 40
5.2.3 Estimating the Number of Clusters on MCP5 depending on the Beam Intensity . . . 41

5.2.4 Analysis of the Lyman Alpha Pulse Data . . . 41
5.2.4.1 Time of Flight (TOF) Cuts . . . 41
5.2.4.2 Scaling of Pulse Height Distributions at different MWS Frequencies . . . 42
5.2.4.3 Determination of the Lamb Shift from the Voltage Pulses 44
5.2.5 Estimating the Number of available H in the 2S state in the Lyman Alpha Detector . . . 44
5.3 Lamb Shift Setup Results . . . 45
5.3.1 TOF Cuts of the Voltage Pulses . . . 45
5.3.2 Signals on the Lyman Alpha MCPs from the LEDs . . . 45
5.3.3 Microwave on/off (Dataset 1) Results . . . 46
5.3.4 Microwave Scan 1 (Dataset 2) Results . . . 50
5.3.5 Microwave Scan 2 (Dataset 3) Results . . . 51
5.4 Discussion of the Lamb Shift Setup Tests . . . 52
5.4.1 Problems and Possible Improvements for the Pulse Finding Algorithm 52
5.4.2 Signals from the LEDs on the Lyman Alpha MCPs . . . 53
5.4.3 MWS Line Shape and Power Spectrum . . . 54
5.4.4 Dataset 1 Results Discussion . . . 54
5.4.5 Dataset 2 Results Discussion . . . 55
5.4.6 Dataset 3 Results Discussion . . . 57
5.4.7 Methods to Improve the Detection Efficiency of Lyman Alpha Photons 57

6 $\overline{\text{H}}$ Production Rate in 2024 at GBAR 59
6.1 Data for the $\overline{\text{H}}$ Production Analysis . . . 59
6.2 $\overline{\text{H}}$ Production Rate Analysis Methods . . . 60
6.2.1 Determining $\overline{\text{H}}$ Production Rate from Voltage Pulses in MCP5 . . 60
6.2.2 Determining $\overline{\text{H}}$ Production Rate from Clusters on MCP5 . . . 61
6.3 $\overline{\text{H}}$ Production Rate Results . . . 61
6.3.1 $\overline{\text{H}}$ Production Rate from Pulses in the Voltage of MCP5 . . . 61
6.3.2 $\overline{\text{H}}$ Production Rate from Clusters on MCP5 . . . 62
6.4 Discussion of the $\overline{\text{H}}$ Production Rate . . . 63

7 Conclusion 66

Bibliography 69

Appendix 75
Scattering on the Carbon Foil from Meyer's Theory [33] . . . 75
Signals from the LEDs at the Lyman Alpha MCPs . . . 76
Dataset 2 Plots . . . 77

Chapter 1

Introduction

The proton charge radius r_p is of great importance for both quantum chromodynamics (QCD) at low energies and quantum electrodynamics (QED) calculations of atomic energy levels. The first measurements of the proton charge radius were performed by R. Hofstadter and R. W. McAllister using the elastic scattering of electrons off of protons [24]. They arrived at a value of $r_p = (7.4 \pm 2.4) \times 10^{-14}\,\text{cm} = (0.74 \pm 0.24)\,\text{fm}$.

1.1 Proton Charge Radius from Scattering Experiments

Detailed calculations on how to calculate the proton charge radius using scattering experiments can be found in [21], for which a short summary follows. To find the proton charge radius with elastic scattering, the proton electric form factor G_{Ep} has to be determined from the scattering cross-section. G_{Ep} can be expressed using Taylor expansions at low momentum transfer $-Q^2$ as:

$$G_{Ep}(-Q^2) = 1 - \frac{1}{6} r_p^2 Q^2 + \mathcal{O}(Q^4) \tag{1.1}$$

Therefore, the slope of Equation (1.1) at $Q^2 = 0$ can be used to determine r_p:

$$r_p^2 = -6 \left. \frac{dG_{Ep}}{dQ^2} \right|_{Q^2=0} \tag{1.2}$$

Since it is impossible to perform experiments at $Q^2 = 0$, the values of G_{Ep} in this region have to be approximated using the available measurements at higher Q^2. Detailed calculations for this have been performed by X. F. Yan and can be found at [45]. With this method, a value of $r_p = 0.831 \pm 0.0007_{stat} \pm 0.012_{syst}$ was found by W. Xiong and others [44].

1.2 Proton Charge Radius from Energy Level Measurements

Another method to determine r_p is by using the Lamb shift. The Lamb shift is the difference between the energy levels of the 2S and 2P states of hydrogen. The energy levels of hydrogen should only depend on the principal quantum number n according to the Schrödinger equation. However, in 1947 Willis E. Lamb Jr. and Robert C. Retherford found a difference in the energy levels of the $2S_{1/2}$ and $2P_{1/2}$ hydrogen atom states of about

1050 MHz, which they called the Lamb shift [31]. Shortly after, Hans A. Bethe published the first nonrelativistic calculations of the Lamb shift [9], assuming it was caused by interactions with the vacuum field, which are responsible for around $\sim$ 96% of the measured Lamb shift. Other contributions are vacuum polarization effects, finite nuclear mass effects and nuclear structure effects [32]. For precise Lamb shift measurements, the fine and hyperfine structure of hydrogen also has to be considered.

1.2.1 Fine Structure of Hydrogen

The fine structure is caused by the electron spin and relativistic corrections to the nonrelativistic Schrödinger equation. It splits the energy levels into further discrete values. Detailed calculations for the fine splitting can be found in chapter 6 of [23], from which a short summary follows. To find the number of energy levels from fine splitting, we use the total angular momentum operator $\hat{\mathbf{J}}$. This operator is defined as $\hat{\mathbf{J}} = \hat{\mathbf{L}} + \hat{\mathbf{S}}$ and its z-component, $\hat{J}_z = \hat{L_z} + \hat{S_z}$ where $\hat{\mathbf{L}}$ is the orbital angular momentum operator and $\hat{\mathbf{S}}$ the spin angular momentum operator, with $\hat{L_z}$ and $\hat{S_z}$ their corresponding z components. $\hat{\mathbf{J}}$ and $\hat{J}_z$ have the eigenvalue j with eigenstates $|jm_j\rangle$. For these we have:

$$\hat{\mathbf{J}}^2 |jm_j\rangle = j(j+1)\hbar^2 |jm_j\rangle \; ; \quad \hat{J}_z |jm_j\rangle = m_j\hbar |jm_j\rangle \, . \tag{1.3}$$

Consequently, $\hat{\mathbf{J}}$ has $2+1$ possible orientations, which characterize $\hat{J}_z$ through:

$$m_j = -j, -j+1, \ldots, +j. \tag{1.4}$$

Thus, m_j has $2j+1$ different possible values. Furthermore, we have for $\hat{\mathbf{J}}$, $\hat{\mathbf{L}}$ and $\hat{\mathbf{S}}$:

$$|\hat{\mathbf{J}}| = \sqrt{j(j+1)}\,\hbar \, ; \quad |\hat{\mathbf{L}}| = \sqrt{l(l+1)}\,\hbar \, ; \quad |\hat{\mathbf{S}}| = \sqrt{s(s+1)}\,\hbar \tag{1.5}$$

with the azimuthal quantum number $l = 0, 1, 2, \ldots, n-1$, the principal quantum number n and the electron spin s. With Equation (1.5) we also have the so-called triangular relation:

$$|l-s|, |l-s|+1, \ldots, \leq j \leq |l+s|. \tag{1.6}$$

We get $2s$ fine structure levels, each $2j+1$-fold degenerate.

1.2.2 Hyperfine Structure of Hydrogen

The hyperfine structure is caused by the energy of the nuclear magnetic dipole moment interacting with the magnetic field generated by electrons and the energy of the nuclear electric quadrupole moment in the electric field gradient. We can follow the steps in chapter nine of [23] for the fundamentals of hyperfine splitting. Similarly to the total angular momentum operator for the fine splitting, the nuclear spin operator $\hat{\mathbf{I}}$, for which $|\hat{\mathbf{I}}| = \sqrt{i(i+1)}\,\hbar$ and the total angular momentum operator of the electron charge cloud $\hat{\mathbf{J}}$ can be used to define the total angular momentum operator of the whole atom:

$$\hat{\mathbf{F}} = \hat{\mathbf{I}} + \hat{\mathbf{J}} \quad \text{with} \quad |\hat{\mathbf{F}}| = \sqrt{f(f+1)}\hbar \tag{1.7}$$

with $f = |i-j|, |i-j|+1, \ldots, i+j$. It follows that $\hat{\mathbf{F}}$ has $2f+1$ possible orientations described by $m_f = -f, -f+1, \ldots, f$. Thus, we get $2j+1$ energy levels if $j \leq i$ and $2i+1$ if $i \leq j$, each $2f+1$-fold degenerate.

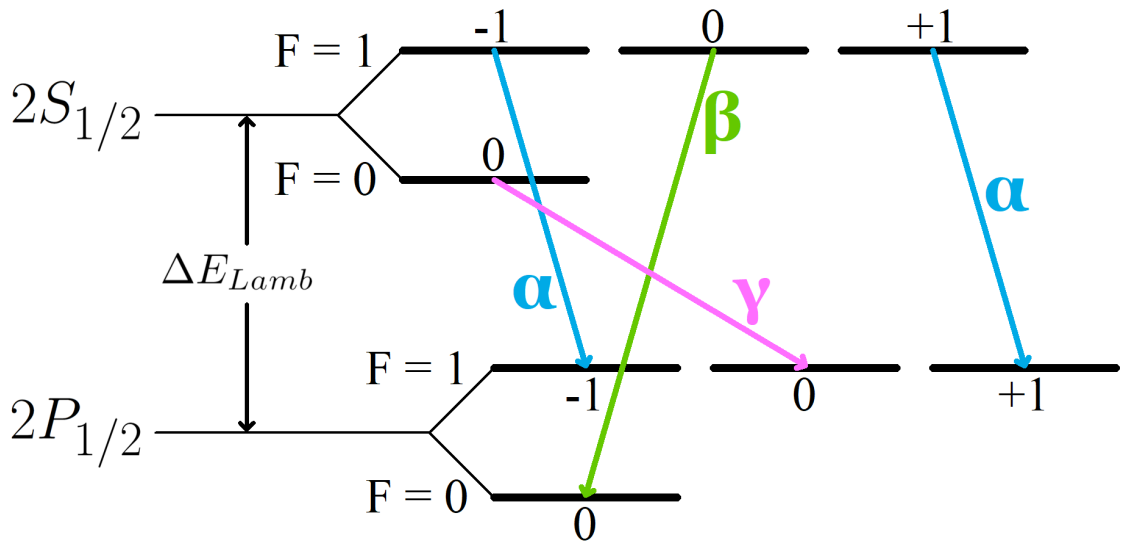

Figure 1.1: Hyperfine transition between the $2S_{1/2}$ and $2P_{1/2}$ states. The α, β and γ transition frequencies are 1087 MHz, 1147 MHz and 910 MHz respectively, using the energy levels calculated in [25].

This means that the lamb shift is made up of the transition from the $2S_{1/2}$ hyperfine states to the $2P_{1/2}$ hyperfine states. An illustration of these transitions can be found in Figure 1.1. The hydrogen energy levels without fine structure splitting are given by [22]:

$$E_n = -\left[\frac{m_e}{2\hbar}\left(\frac{e^2}{4\pi\varepsilon_0}\right)^2\right]\frac{1}{n^2}, \quad n = 1, 2, 3, \ldots \tag{1.8}$$

where m_e is the mass of an electron, $\hbar = \frac{h}{2\pi}$ the reduced Planck constant, e the elementary charge, ε_0 the vacuum permittivity and n the principal quantum number. For $n = 1$ this is equal to $E_1 = 13.6\,\text{eV}$, so Equation(1.8) can be written as

$$E_n = \frac{13.6}{n^2}, \quad n = 1, 2, 3, \ldots \tag{1.9}$$

If fine splitting is also considered, we get the correction [22]:

$$E_{FS} = -\frac{13.6}{n^4}\alpha^2\left(\frac{n}{j+1/2} - \frac{3}{4}\right) eV \tag{1.10}$$

with $\alpha \approx 137$ the fine structure constant and $j = l \pm 1/2$ the total angular momentum quantum number. With hyperfine splitting, we get the first order correction [22]:

$$E_{HF} = \frac{\mu_0 g_p e^2}{8\pi m_p m_e}\left\langle\frac{3(\mathbf{S}_p \cdot \hat{r})(\mathbf{S}_e \cdot \hat{r}) - \mathbf{S}_p\mathbf{S}_e}{r^3}\right\rangle + \frac{\mu_0 g_p e^2}{e m_p m_e}\langle\mathbf{S}_p \cdot \mathbf{S}_e\rangle|\psi(0)|^2 \tag{1.11}$$

where μ_0 is the vacuum permeability, $g_p \approx 5.59$ is the proton g-factor, $g_e \approx 2.00$ is the electron g-factor, m_p is the proton mass, $\mathbf{S}_p$ is the proton spin, $\mathbf{S}_e$ is the electron spin, r is the distance from the centre of the proton for which $\langle \frac{1}{r} \rangle = \frac{1}{n^2 a}$ with a the Bohr radius and $|\psi(0)|$ is the value of the electron wave function at the nucleus. For general states with $l = 0$, the wave function is spherically symmetric and the first expectation value in Equation(1.11) vanishes. Specifically for $n = 0$ we have $|\psi(0)|^2 = \frac{1}{\pi a^3}$. If we now also use that with spin-spin coupling the valid states for the proton and electron spin are eigenvectors of the total spin $\mathbf{S} = \mathbf{S}_p \cdot \mathbf{S}_e$, we get $\mathbf{S}_p \cdot \mathbf{S}_e = \frac{1}{2}(S^2 - S_e^2 - S_p^2)$. Since both the electron and proton have spin 1/2, we have $S_e^2 = S_p^2 = \frac{3}{4}\hbar^2$. For S^2, we need to differentiate between the triplet and the singlet state. In the triplet state we have $S^2 = 2\hbar^2$ and in the singlet state $S^2 = 0$. This means that for $n = 0$ the hyperfine correction can be written as:

$$E_{HF,n=0} = \frac{4 g_p \hbar^4}{3 m_p m_e^2 c^2 a^4} \begin{cases} +1/4, & \text{triplet} \\ -3/4, & \text{singlet} \end{cases} \tag{1.12}$$

Since the proton is not point-like, there is also a correction relating to its finite size [41]:

$$E_{r_p} = -\frac{2}{3}\frac{\alpha^4}{n^3} m_r^3 c^6 \left(\frac{r_p}{\hbar c}\right)^2 \tag{1.13}$$

The final energy levels are the combination of Equations (1.9), (1.10), (1.11) and (1.13):

$$E_{njlf} = E_n + E_{FS} + E_{HF} + E_{r_p} \tag{1.14}$$

Using Equations (1.13) and (1.14) we get the expression for the proton charge radius

$$r_p^2 = -\frac{3}{2}\frac{n^3 \hbar^2}{\alpha^4 m_r^3 c^4}(E_n + E_{FS} + E_{HF}) \tag{1.15}$$

The above calculations are all lower-order approximations. Much more detailed calculations to get a more accurate value for r_p can be found in [25]. In [11], these calculations are used to get a value of $r_p = (0.833 \pm 0.010)\,\text{fm}$. It is also possible to measure the energy levels of muonic hydrogen to get the proton charge radius. Since a muon is much heavier than an electron, it orbits much closer to the nucleus. This means, that the contribution from the proton charge radius to the energy levels is around 6.4×10^6 times larger than for ordinary hydrogen [21], and thus more precise measurements of r_p can be performed. For muonic hydrogen, a value of $r_p = (0.840\,87 \pm 0.000\,39)\,\text{fm}$ has been found by measuring the transition energies from the $2S_{1/2}^{F=0}$ to $2P_{3/2}^{F=1}$ and $2S_{1/2}^{F=1}$ to $2P_{3/2}^{F=2}$ states [7].

1.3 Antiproton Charge Radius

With the proton charge radius being known quite precisely, a measurement for the antiproton charge radius $r_{\bar{p}}$ would be a great test for CPT invariance. Precise measurements of the energy levels of antihydrogen would allow the determination of $r_{\bar{p}}$ without

referring to any non antimatter measurements. The ALPHA experiment at CERN has delivered some results for the fine structure of antihydrogen by measuring the transition frequencies from the $1S_{1/2}$ to the $2S_{1/2}$ state [3] as well as from the $1S_{1/2}$ to the $2P_{1/2}$ and $2P_{3/2}$ states [4], [2]. Their measurements for the Lamb shift ($2S_{1/2} \rightarrow 2P_{1/2}$) were consistent with the theory at a level of 11 %. However, since the contribution to the Lamb shift of antihydrogen of the antiproton charge radius is very small, more precise measurements are needed for a meaningful value of $r_{\bar{p}}$. This is what the GBAR experiment at CERN is aiming to do. GBAR stands for "Gravitational Behaviour of Antimatter at Rest", which is the ultimate goal of the experiment. For this, a large number of antihydrogen will be produced, of which a significant amount is in the $2S$ state. These antihydrogen atoms in the $2S$ state allow for a precise measurement of the Lamb shift of antihydrogen.

Chapter 2

Setup of the Experiment

The aim of the GBAR experiment is to investigate the effect of gravity on antimatter. This is done by producing very slow, on the order of 1 m/s, positive antihydrogen using laser cooling. One positron then gets removed with a laser and the acceleration of the antihydrogen by the gravitational force from the earth is measured. For this, a large number of antihydrogen is produced of which a significant amount is in the $2S$ state which can be used for precise measurements of the Lamb shift of antihydrogen, which would allow for the determination of the antiproton charge radius. A comparison between the proton and antiproton charge radius would provide a test of CPT.

The GBAR experiment receives antiprotons at around 100 keV delivered from the ELENA ring at CERN. The antiprotons are subsequently cooled to 6 keV thereupon they collide with a dense positronium beam in the reaction chamber. In this process $\overline{\mathrm{H}}$ and $\overline{\mathrm{H}}^+$ are produced. The current state of the experiment is to try to maximize the production of $\overline{\mathrm{H}}$ using this reaction. After the $\overline{\mathrm{H}}$ is produced, its Lamb shift can get measured using microwave systems.

2.1 Positron Line

The positron line largely functions separately from the $\overline{\mathrm{p}}$ line. At the end of the positron line, the positrons enter the reaction chamber and thus the $\overline{\mathrm{p}}$ line.

2.1.1 Positron Production [14]

As a first step towards the positron production, 9 MeV electrons are produced with a linear accelerator. In a linear accelerator, particles get accelerated by passing through electrodes which are changing their polarization periodically. This period is defined in such a way, that the particle always experiences a force in the same direction. So for electrons a positive voltage is applied to the electrode, effectively pulling the electron towards its centre, until the electron reaches the middle of the electrode. At this point, a negative instead of a positive voltage is applied to the electrode, pushing the particle away from the centre of the electrode. All the electrodes change polarization with the same frequency, meaning that electrodes further towards the end of the linear accelerator

get longer as the speed of the electron increases. The linear accelerator for the GBAR experiment has 18 separate electrodes with radius 4.5 mm and a total length of 900 mm. The electrons get accelerated to 9 MeV.

After the acceleration of the electrons to 9 MeV they impinge on a 1 mm thick tungsten target. When the electrons reach the target, positrons are mainly produced by bremsstrahlung where highly energetic photons are ejected from the electrons, which produce positrons via pair production. The positrons' energy spectrum goes up to around 7 MeV, which is too fast for their trapping. To slow them down, a moderator is placed 2 mm after the target. A moderator is a solid, in our case tungsten, in which the positrons lose energy until they are close to thermal equilibrium with the crystal lattice. This is a surface process which has an increasing efficiency with the emitting area of the moderator. The moderator used for the GBAR experiment has twelve layers, each of which is a woven wire mesh of 20.3 µm thickness with a wire distance of 140 µm.

2.1.2 Trapping of the Positrons [13]

The positrons are accumulated and trapped, such that as many as possible are available for each $\bar{p}$ shot from ELENA. This trapping consists of a three stage Buffer Gas Trap (BGT) followed by a high field Penning Trap (HFT). The BGT consists of three sections, each of which is a Penning-Malmberg trap, as described in Section 2.3.1.3 where the trapped particles have a positive instead of a negative charge. The first section is made up of 15 electrodes with a radius of 8 mm and a length of 24 mm. Nitrogen gas is injected into the trap, with which the positrons collide and thus lose enough energy so that they cannot escape from the potential well in the trap. A high concentration of nitrogen gas is required in the trap to maximize the trapping efficiency. The lifetime of the trapped positrons is mainly constrained by radial movements caused by elastic collisions with the nitrogen gas, which ultimately leads to the annihilation of positrons on the trap wall. To counteract this process, CO_2 gas is injected in the second and third section of the BGT instead of N_2 gas. The CO_2 gas has better cooling rate at low positron energies and with the help of a rotating wall electrode, the radial expansion can be stopped and the positron lifetime is only limited by annihilation with the CO_2 gas. The second section of the BGT is made up of 5 electrodes with a diameter of 41 mm and a length of 49 mm and is directly connected to the first section. The third section consists of 14 electrodes with a diameter of 41 mm and each electrode has a length of around 17.4 mm. This allows for the formation of harmonic wells at almost every position in the third section. The second and third section are connected by an aluminium pumping restriction.

Once there are enough positrons in the third section of the BGT, they are transferred to the HFT. A homogeneous magnetic field is generated inside the HFT by a superconducting magnet. There are 27 electrodes with a diameter of 38 mm in the HFT. The last electrode on either side of the HFT has a length of 270 mm, the next two on either side of the trap

have a length of 160 mm while the 21 central electrodes have a length of 22 mm. Voltages between ± 4000 V can be applied to the electrodes, where the voltage difference between two consecutive electrodes cannot be bigger than 2000 V. Two of the inner electrodes are split into four parts, which allows them to produce a rotating wall magnetic field. The positrons in the HFT are cooled with synchrotron radiation of electrons that can be injected into the trap. When new positrons come from the BGT, the voltage at the entrance electrode of the HFT is lowered so they can pass through and enter the HFT. The positrons which are already in the HFT were cooled and thus cannot escape as long as the voltage is not too low.

2.2 Antiproton Production and Cooling before the GBAR Experiment

Protons are first produced in the Proton Synchrotron at CERN and are then fired at an iridium rod where many energetic particles are produced from collisions, including antiprotons. These are then led into the AD ring and later transferred to the ELENA ring for cooling, after which they are guided to the experiments.

2.2.1 Cooling of Antiprotons in the AD ring

Just after the production of the $\overline{p}$, they enter the AD ring. There they are cooled to around 5.3 MeV using Radio frequency (RF) systems, Stochastic cooling and Electron cooling. After the AD ring, the beam enters the ELENA ring.

2.2.1.1 Radiofrequency Cooling

The RF system uses alternating positive and negative electric fields with a frequency of around 0.5 MHz - 2 MHz to decelerate the protons. Magnets in the cavities are also used for the bunching of the beam.

2.2.1.2 Stochastic Cooling

Stochastic cooling uses the velocity of single particles in a bunch and applies a kick depending on their velocity. This kick consists of an electric field with which the transverse momentum of the particles gets reduced.

2.2.1.3 Electron Cooling

With electron cooling, an electron beam parallel to the antiproton beam is injected. The injected electrons are a bit slower than the antiprotons, and the electron beam has a very low emittance. Through Coulomb interactions between the electrons and the antiproton, the transverse emittance of the antiproton beam gets reduced. To separate the electrons from the antiprotons again, a weak magnetic field is applied to the beam cavity. Since

the electrons are much lighter than the antiprotons, the electron beam gets guided away while the antiproton beam is nearly unaffected.

2.2.2 Cooling in the ELENA Ring

The ELENA ring is a 30 m long synchrotron and is hexagonal. First, another RF cavity with voltage less than 500 V is used to bring down the energy of the antiprotons from 5.3 MeV to around 0.65 MeV. To decrease the antiproton energy further to 100 keV, electron cooling is applied to reduce the beam emittance and minimize losses of particles [34]. Once the beam has been cooled to 100 keV, it is diverted to the experiments.

2.3 Antiproton Beam Line at the GBAR Experiment

When the $\overline{\mathrm{p}}$ beam arrives at the GBAR experiment from the ELENA ring, it first needs to undergo further cooling. After that, the beam collides with positronium to produce $\overline{\mathrm{H}}$ and $\overline{\mathrm{H}}^{+}$, which can be used for measurements of the Lamb shift and tests of the gravitational effects on $\overline{\mathrm{H}}$.

2.3.1 Cooling of Antiprotons at the GBAR Experiment

The setup of the antiproton beam line up to the reaction chamber is illustrated in Figure 2.1. Once the beam arrives at the GBAR experiment, it enters a drift tube, which decreases the axial momentum of the beam. After the drift tube, the beam passes through an Einzel lens before entering a Penning-Malmberg trap. The trap is used to decrease the transversal momentum, and thus the emittance, of the beam and to compress the beam radially. Following the extraction of the Penning-Malmberg trap, the beam passes through two more Einzel lenses, thereupon reaching the reaction chamber. These different processes are further explained in the sections below.

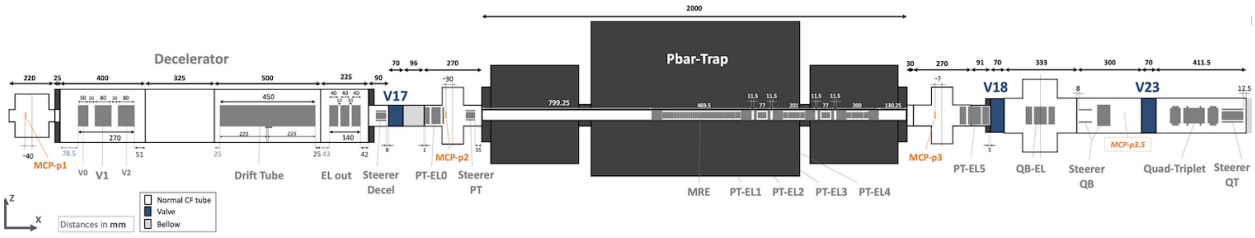

Figure 2.1: Antiproton line schematics of the GBAR experiment before the reaction chamber, taken from the GBAR collaboration.

2.3.1.1 Einzel Lens

An Einzel lens focuses a beam of charged particles without changing their energy. This is achieved by putting at least three cylindrical or rectangular apertures along the beam line.

To the outer two, an identical positive voltage is applied, while a negative one is applied to the one in the middle. With this setup, the particles further away from the beam centre get deflected more than the ones closer to its centre and the beam gets focused. The beam also does not lose any energy, since the electrostatic potential of the lens is symmetric.

2.3.1.2 Cooling the Beam in a Drift Tube

The voltage V_{Drift} is applied to the drift tube, which decelerates the beam to 100 keV $-$ V_{Drift}. The particles in the beam would just accelerate back up to 100 keV upon leaving the drift tube because of the subsequent voltage gradient. To prevent this, the voltage applied to the drift tube has to be turned off while the beam is inside of it [26]. Since with this technique only the axial momentum decreases and the transverse momentum stays the same, the beam emittance blows up after the drift tube and the beam needs to be refocused. This is accomplished using an Einzel lens.

2.3.1.3 Reducing Beam Emittance with a Penning-Malmberg Trap

In order to reduce the beam emittance and focus the beam, a Penning-Malmberg trap is installed after the drift tube. Penning traps are used for the trapping of charged particles. A detailed explanation of how they function can be found at [12], for which a short summary follows. A homogeneous magnetic field $\mathbf{B} = B\vec{e_z}$ confines the particles radially and a quadrupole electric field $\mathbf{E}$ confines them axially. The magnetic field is produced by a superconducting solenoid magnet. The electric field is generated by three electrodes, one ring electrode with radius r_0 around the trapping region and two end cap electrodes with distance z_0 from the trap centre. For $\bar{p}$, the end caps need to be charged negatively, which produces a saddle point in the middle of the trap around which the particles oscillate harmonically with angular frequency

$$\omega_z = \sqrt{\frac{qV_0}{mz_0^2}} \tag{2.1}$$

where q is the charge of a trapped particle and V_0 the voltage between the ring and end cap electrodes. The combination of the magnetic and electric fields cause the particles to move in an eptrochoidal motion in the radial plane defined by the two angular frequencies

$$\omega_\pm = \frac{1}{2}\left(\omega_c \pm \sqrt{\omega_c^2 - 2\omega_z^2}\right) \; ; \quad \omega_c = \frac{q}{m}B \tag{2.2}$$

where m is the mass of a trapped particle. ω_c, ω_z, ω_+ and ω_- are called the free cyclotron frequency, axial frequency, modified cyclotron frequency and magnetron frequency. For this system to be stable, all frequencies must be real and thus

$$\omega_c^2 > 2\omega_z^2 \quad \text{or equivalently} \quad B > \sqrt{2\frac{mV_0}{qz_0^2}} \tag{2.3}$$

is required. In reality, the motion of the particles cannot be precisely defined by these three frequencies, because of imperfections in the setup or particle interactions.

Penning-Malmberg traps function the same way, with the one difference that the ring electrode is longer, which allows for the confinement of more particles. The detailed setup for the trap used for the GBAR experiment is outlined in [46]. There are some additional features compared to a classical Penning-Malmberg trap, since the beam gets compressed radially and the beam emittance gets decreased. The ring electrode is split into eleven electrodes, of which one is called the "rotating wall electrode" and another one is a ground electrode. These eleven electrodes form a harmonic potential well which traps the antiprotons. The rotating wall electrode is split into 4 parts and generates a rotating electric field while applying RF voltages with different phases to each of the 4 parts. This setup results in radial compression of the beam, as presented in [6]. To reduce the beam emittance, electrons are injected into the trap before the $\bar{p}$ beam enters. These electrons quickly lose energy through synchrotron radiation. Once the beam enters the trap, the antiprotons lose energy through collisions with the electrons. They should lose around 95% of their energy after 110 s in the trap. The electrons can be removed by changing the magnetic field, which influences the electrons a lot more than the antiprotons due to their much lower mass. When the antiprotons are extracted from the trap, the voltage of the downstream end cap electrode is changed such that the beam gets accelerated axially to the desired energy. A double-gap buncher system [30] is also used for the bunching of the beam. Once the beam leaves the trap, it diverges due to the space-charge effect [46]. To counteract this, two Einzel lenses are placed after the trap, after which the reaction chamber follows.

2.3.2 Reaction Chamber

The setup for the antiproton beam line starting from the reaction chamber is illustrated in Figure 2.2. As the positrons enter the reaction chamber, they collide with a dense electron cloud and positronium is produced. The positronium and antiproton beam then collide at the target position in the reaction chamber, triggering the reaction

$$\overline{\mathrm{p}} + \mathrm{Ps}(n_p, l_p) \rightarrow \overline{\mathrm{H}}(n_h, l_h) + \mathrm{e}^- \tag{2.4}$$

where n_p and l_p are the principal and angular momentum quantum numbers of the positron and n_h and l_h are the principle and angular momentum quantum numbers of the antihydrogen. Following this, we have a further reaction

$$\overline{\mathrm{H}}(n_h, l_h) + \mathrm{Ps}(n_p, l_p) \rightarrow \overline{\mathrm{H}}^+ + \mathrm{e}^-. \tag{2.5}$$

The cross-sections of the reactions (2.4) and (2.5) have been calculated in [15]. The dependence of the cross-sections on the positronium and antiproton states and energy have been further investigated in [16]. It was found that the positronium should be in

the $3d$ state and the antiprotons at 6 keV. It was predicted that for a pulse with $3 \cdot 10^6$ $\overline{\mathrm{p}}$ at 6 keV and 1 keV, at least one $\overline{\mathrm{H}}^+$ should be produced. Since the beam FWHM needs to be quite short for 1 keV, which would be difficult to achieve with the beam as it is delivered by ELENA, 6 keV was chosen for the $\overline{\mathrm{p}}$ energy.

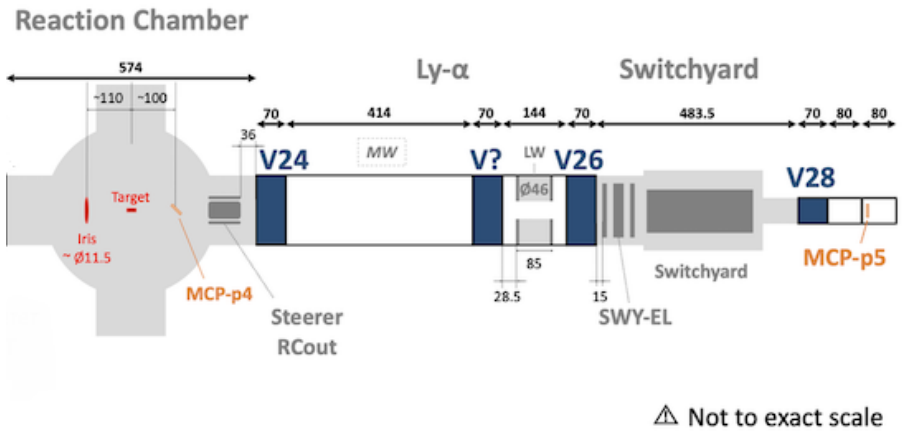

Figure 2.2: Antiproton line schematics of the GBAR experiment starting from the reaction chamber, taken from the GBAR collaboration.

2.3.3 Lamb Shift Setup

After the $\overline{\mathrm{H}}$ production, an electric field is applied to the beam which separates the positive, neutral and negative particles from each other. We are interested in the neutral particles to determine the Lamb shift of antihydrogen. A detailed description of the whole microwave setup can be seen at [40], of which a short summary follows.

We are interested in the three transitions α ($2S_{1/2}^{F=1,m_f=\pm1} \rightarrow 2P_{1/2}^{F=1,m_f=\pm1}$) around 1087 MHz, β ($2S_{1/2}^{F=1,m_f=0} \rightarrow 2P_{1/2}^{F=0,m_f=0}$) around 1147 MHz and γ ($2S_{1/2}^{F=0,m_f=0} \rightarrow 2P_{1/2}^{F=1,m_f=0}$) around 910 MHz. We know from [2], [4] and [3] that these transitions are similar for $\overline{\mathrm{H}}$ as for H, so we take measurements assuming the same energies and inspect the final result for any discrepancies. If we assume that each state in $2S_{1/2}$ has the same likelihood of occurring, we will observe twice as many α as β and γ transitions. Once a transition from the $2S_{1/2}$ state to the $2P_{1/2}$ state is induced, the particle in the $2P_{1/2}$ state with lifetime 1.6 ns quickly decays to the ground state while emitting a Lyman alpha photon. The full width half maxima of the distribution of the Lyman alpha photons can be calculated following the steps in [17] by using the energy-time uncertainty relation and the finite lifetime $\tau = 1.6\,\mathrm{ns}$ of the $2P_{1/2}$ states taken from [11]

$$\tau \Delta E = \hbar \quad \Rightarrow \quad \Delta E = \frac{\hbar}{\tau}. \tag{2.6}$$

We can now use the equation for the energy of a photon

$$\Delta E = h\Delta f = \frac{\hbar}{\tau} \quad \Rightarrow \quad \Delta f = \frac{\hbar}{h\tau} \tag{2.7}$$

we get a full width half maximum of $\Delta f = 100\,\text{MHz}$. We can now get the lineshape for different energies for each transition $p(\omega)$ using a Breit-Wigner distribution

$$p(\omega) = \frac{1}{(\omega^2 - \omega_0^2) + \Delta f^2 \omega_0^2} \tag{2.8}$$

with ω_0 the centre of the distribution, so around 1087 MHz, 1147 MHz and 910 MHz for the α, β and γ transitions. These lineshapes, together with their sum, are displayed in Figure 2.3. We can clearly see, that the α and β transitions blend together in the total lineshape, but the γ transition is somewhat separated from them. This means, that ideally, the α and β transitions should be induced and the γ transition observed. For this, the Hyperfine Selector (HFS) is installed after the reaction chamber. The HFS consists of two parallel plate electrodes in a box, through which the beam passes. Between the electrodes an electric field is induced, which is homogeneous throughout the whole beam area and oscillating with a frequency of 1.1 GHz. Once a transition from the $2S_{1/2}$ state to the $2P_{1/2}$ state is induced, the particle in the $2P_{1/2}$ state with lifetime 1.6 ns quickly decays to the ground state while emitting a Lyman alpha photon.

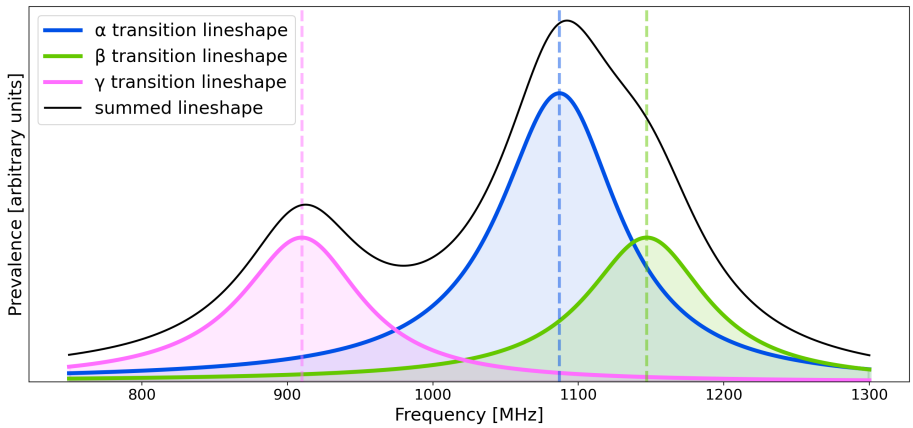

Figure 2.3: Observable lineshapes of the α, β and γ transitions using a Breit-Wigner distribution. The α lineshape is in blue, the β lineshape is in green and the γ lineshape is in pink. The sum of the lineshapes of the three transitions is in black.

After the HFS, the Microwave Scanner (MWS) is placed. The MWS functions similarly to the HFS, except that its frequency can be set to different values so that the probability of inducing the $2S_{1/2}$ state to the $2P_{1/2}$ state transition varies. After the MWS, the detector follows. Inside the detector, a static electric field, generated by two ring anodes in the detector, is present. This field is called the quenching field and quenches any remaining $2S_{1/2}$ states to the $2P_{1/2}$ states. Any particles in the $2P_{1/2}$ state quickly decay to the ground state while emitting a Lyman alpha photon. These photons are measured with

4 microchannel plate detectors (Section 2.3.3.3), which are placed on the sides of the detector. The quenching region is surrounded by a grounded tungsten grid to avoid the quenching field and the MCPs to influence each other [28]. With the number of photons from the $2P_{1/2}$ state decay, a lineshape similar to the one in Figure 2.3 should be recovered and the transition energy determined. There is also a lot of background noise from other particles impacting on the microchannel plate detectors, so these signals need to be carefully analysed.

There are also four LEDs mounted at the end of the MWS. These LEDs emit photons with a wavelength of 265 nm to 280 nm. This allows us to see a signal created primarily by photons of a single wavelength which produce a similar signal as the Lyman alpha photons except that the Lyman alpha photons have a shorter wavelength. This means that they have higher energy, and thus the signal from the Lyman alpha photons in the MCPs should to be at higher voltages compared to the one from the LED photons.

2.3.3.1 Microwave Apparatus Setup and Circuit

A schematic of the microwave apparatus as presented in [40] can be seen in Figure 2.4. There is an input power on the order of 1 mV which goes to the signal generator. The signal then goes through a 40 dB amplifier and gets amplified to around 10 W. Next the signal reaches a 180° phase inverting high power divider which is connected to the two plate electrodes generating the field in the microwave apparatus. After the plate electrodes, the signal gets combined again and measured by a power meter.

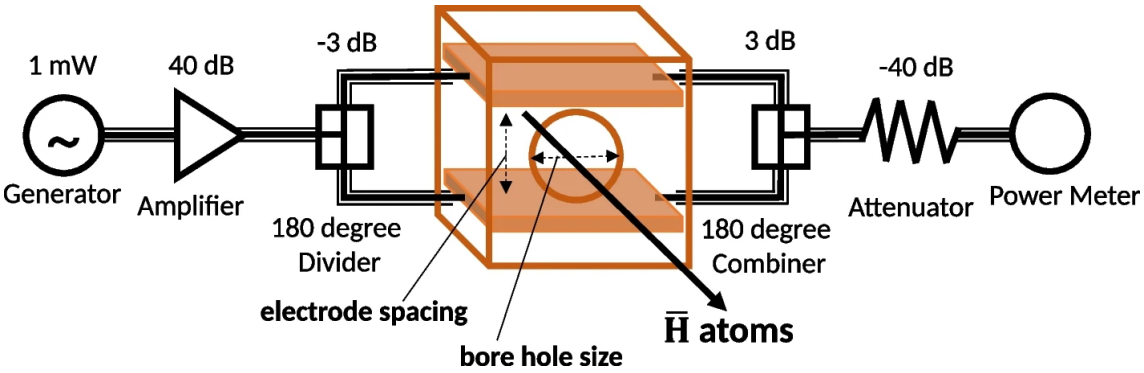

Figure 2.4: Setup of the MWS and HFS and the associated circuits taken from [40].

2.3.3.2 Efficiency of the MWS at different Frequencies

A simulation of the microwave system was created by Tanaka Takumi as seen in [40] to determine the efficiency of the MWS at different powers to induce the $2S_{1/2} \rightarrow 2P_{1/2}$ transition at different frequencies. For the MWS power at -3 dBm and when taking the spacial and energy distribution of the hydrogen as well as the spacial distribution of the microwave field into account, the results from this simulation are displayed in Figure

f_{MWS} [MHz]	800	900	1000	1060	1100	1200	1300
MWS efficiency	0.36	0.57	0.78	0.86	0.85	0.64	0.31

Table 2.1: Efficiency of the MWS at -3 dBm input power to induce the $2S_{1/2} \rightarrow 2P_{1/2}$ transition at different MWS frequencies f_{MWS}. The values are obtained from the simulation of the microwave system seen in [40] where the power dependence of the MWS on the frequency was also included.

2.5a. As expected, this looks similar to the summed lineshape in Figure 2.3. Through the electric circuit seen in Figure 2.4 a frequency dependence of the actual input power of the MWS is created. The results of the simulation while also including this frequency dependence of the MWS power are displayed in Figure 2.5b. These are the results that we will use for the analysis. For Dataset 1 we are interested in the MWS efficiency at the frequency 1060 MHz and for Dataset 3 at the frequencies 800 MHz, 900 MHz, 1000 MHz, 1100 MHz, 1200 MHz and 1300 MHz. These values can be seen in Table 2.1.

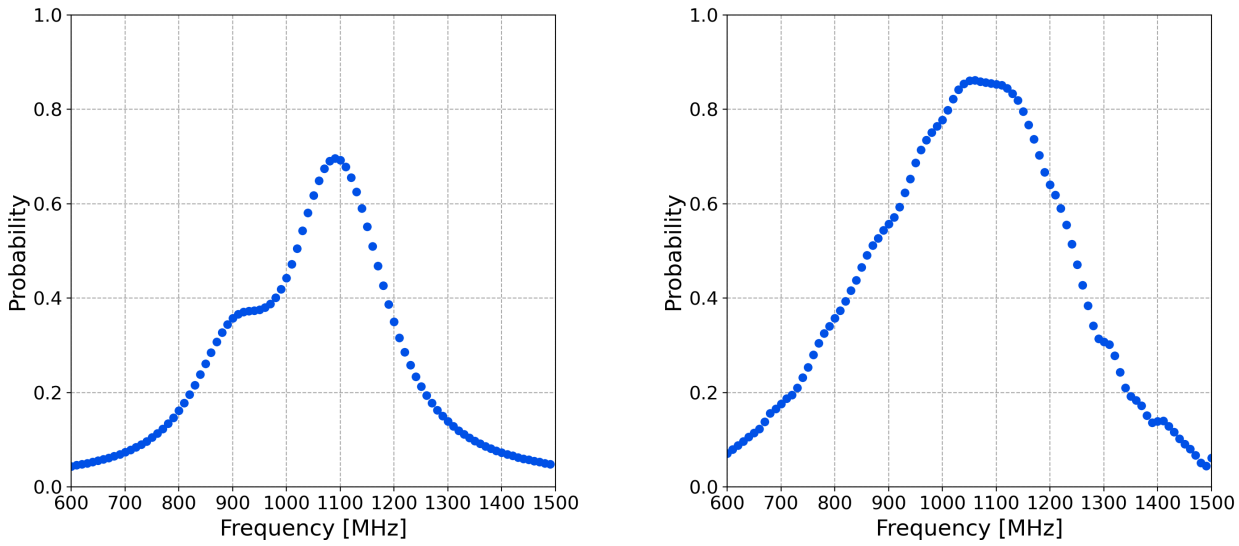

Figure 2.5: Probabilities for the MWS to induce the $2S_{1/2} \rightarrow 2P_{1/2}$ transition at different frequencies. The simulation from Takumi Tanaka seen in [40] was used to obtain the probabilities. For the figure on the left, the spacial and energy distribution of the hydrogen atoms as well as the spacial distribution of the microwave field were taken into account. The electrical circuit of the MWS also introduces a frequency dependence of the MWS power. In the right figure are the probabilities obtained from the simulation if this frequency dependence is also considered.

2.3.3.3 Microchannel Plate Detector (MCP)

MCPs are used to detect single particles and photons. They are made of a thin plate with thickness around 1.5 mm of a resistive material, such as glass. This material has a multitude of tiny holes, which are around 15 µm in diameter. These holes are parallel to each other and go through the plate at a slight angle, around 10 degrees, from the surface.

Around 50 % of the surface area of the MCP is covered by these holes. A strong electric field called the MCP bias is applied to the whole MCP such that each hole becomes an electron multiplier. This means that if a particle impacts the MCP and enters one of the holes, a cascade of electrons is triggered. On the other side of the MCP, the electrons exit and reach an anode. Whenever an electron shower reaches this anode, a peak in its voltage is visible, so we get the particles impacting on the MCP through time. It is also possible to get a spatial image of the MCP. This is done with a phosphor screen placed behind the MCP, which also acts as an anode. When the electrons from the MCP reach the phosphor screen, photons are emitted, which get captured by a CCD camera placed behind the phosphor screen. However, time resolution is not possible in the images from the CCD camera. In the GBAR experiment, these pictures have 1392×1040 pixels. Each of these pixels has a number as a value and this value correlates to the charge of the particles impacting on the phosphor screen at the position of the pixel.

The MCPs used in the GBAR experiment are so-called chevron MCPs. They consist of two consecutive MCPs, the latter being rotated by 180 degrees. This means, that an electron shower from the first MCP triggers one on the second MCP. Chevron MCPs allow for less noise and more gain compared to single MCPs. The MCPs in the Lyman alpha detector also have a cesium iodide (CsI) coating, which improves the quantum efficiency of the MCPs, which is the probability that an electron shower is started by a photon [18, 19, 39]. This is because the CsI converts incoming photons into electrons via the photoelectric effect.

There is a maximum and minimum voltage cap that are measured for the MCPs. If the voltage would go above or below these caps, the measured voltage stays constant at the value of this cap. The values of the caps depend on the oscilloscope settings. Similarly, the measured voltage can only be at discrete values, which also depend on the oscilloscope settings. These voltage values are at a distance of 0.667 mV from each other for the measurements of the Lyman alpha MCPs.

2.3.4 Beam Line after the Lamb Shift Setup

Just after the microwave setup, an Einzel lens is placed. After this, the switchyard follows. In the switchyard, an electric field can be applied to the beam to deflect any charged particles that are still present. These charged particles can be produced by annihilation. Some charged particles also do not get deflected in the reaction chamber, since only a small electric field can be applied to the beam before the Lamb shift setup, otherwise some $\overline{\mathrm{H}}$ in the $2S_{1/2}$ state might already be quenched. With the current installation the beam line ends shortly after the switchyard and an MCP, called MCP5, is placed at its end.

2.4 Beam Line Modifications for a H^- Beam

With the current state of the GBAR experiment, not enough $\overline{H}$ are produced for a Lamb shift measurement of antihydrogen. However, the Lamb shift setup can still be tested with hydrogen. A H^- beam can get delivered by the ELENA ring to the experiment. This beam passes through the drift tube and get slowed down to around 6 keV. The Penning-Malmberg trap is turned off for the H^- beam. The positron beam line is also not needed for the H^- beam. Instead, a thin carbon foil is placed at the target position. When the beam reaches the carbon foil, the additional electron gets stripped and neutral hydrogen passes down the beam line. The thickness of the carbon foil as well as the scattering of the beam on the carbon foil need to be determined. The Lamb shift setup can now be used to measure the Lamb shift of hydrogen. The Lamb shift recovered from these measurements can be compared to the established one to confirm that the setup can be used for Lamb shift measurements of $\overline{H}$.

Chapter 3

General Analysis Methods

3.1 Error Estimations and Propagation

If two values n_1 and n_2 with uncertainties e_1 and e_2 are added or subtracted from each other, the resulting uncertainty is given by

$$e = \sqrt{e_1^2 + e_2^2}. \tag{3.1}$$

For the multiplication of n_1 and n_1 with errors e_1 and e_2 and $n_1 \times n_2 = n$ the uncertainty of n is given by

$$e = n\sqrt{\left(\frac{e_1}{n_1}\right)^2 + \left(\frac{e_2}{n_2}\right)^2}. \tag{3.2}$$

For both the number of voltage pulses and number of clusters on the MCP images, an error of $\sqrt{n}$ with n the number of pulses or clusters is used for the uncertainty.

3.2 Finding Clusters on MCP5

We are interested in the number of clusters on MCP5, since we can get the number of particles on MCP5 and some other information from these clusters. A cluster is defined as the pixels in an image which are adjacent to each other and have a value above a certain threshold. The images are generated by a CCD camera which records the image from the phosphor screen over 1 µs. These images have a resolution of 1392×1040 pixels. When searching for clusters on the MCP only pixels which correspond to the MCP are considered and since the phosphor screen is bigger than the MCP some pixels have to be discarded. For this, we set the centre of MCP5 at the pixel position (731,533) and its radius to $r_{MCP5} = 460$ pixels. Pixels outside this are ignored. The threshold for pixels to be considered part of a cluster changes depending on the beam properties, but generally it is determined using the average value of the pixels that are part of MCP5 of the pedestal file μ_{ped} and the standard deviation of these pixels σ_{ped}. The size of a cluster is the number of pixels which are part of it, and the charge of a cluster is the sum of the values of all pixels in it.

The main problem with the cluster finder is that there is no good method to determine if the clusters from two particles overlap and are only counted as one cluster. As mentioned before, this is only a problem if there are a lot of particles present. This means that, for example, in Section 6.3.2 this is no problem since there are very few clusters visible on MCP5. However, for the images of the MCP taken for the events of Dataset 3 there can be upwards of 1000 clusters per image, so there will nearly always be too few clusters counted. One idea to check for this would be to search for local maxima in each cluster. A pixel closer to the exact position of a particle impact will have a higher value than pixels further away from this position, and this falls off relatively quickly. It would be challenging to find the correct parameters, since the clusters from similar particles can still look quite different. The shape of the clusters can also vary quite a bit.

Another method would be to train a simple supervised machine learning model which looks at the clusters found by the cluster finder and returns the actual number of clusters. This was attempted for this analysis, though not implemented for the final results. The model was generated using the scikit-learn library on python [37]. Clusters found by the cluster finder from images of MCP5 from 2023 were taken. Some of these clusters consist of multiple overlapping clusters. This means that only one particle would be counted when there were multiple particle impacts on the MCP. The actual number of particles forming each cluster has to be determined manually. The model can now be trained using these clusters and the number of particles that formed the cluster. The model created this way was trained on 1355 clusters, of which 163 contained multiple particles. Since there was not a lot of data for clusters formed by more than two particles, the model was trained to return 1 for each cluster formed by a single particle and 2 if the cluster was formed by two or more particles. This model was then tested for 905 clusters, of which 260 contained multiple particles. All but 15 clusters were predicted correctly, meaning that the model had an accuracy of 98.3 %. Of these 15 false predictions by the model, 2 was predicted five times and 1 ten times. This means that single particle clusters were predicted correctly 640 out of 645 times, so 99.2 % of single particle clusters were predicted correctly. The multiple particle clusters were predicted correctly 250 out of 260 times, meaning that 96.2 % of them were predicted right.

The model described above already works pretty well even though it does not have very much training data and would likely increase its accuracy if more training data is added. So we showed that the problem with the overlapping clusters can be countered using a machine learning algorithm. The only problem would be to detect clusters formed from more than two particles, as there are not that many such clusters in the images used for the training. However, there are few such clusters in the MCP5 pictures of Dataset 3 so the number of particles on MCP5 would only differ very slightly from the number of clusters found. If there were images with a lot of clusters formed from more than two particles, a new model would have to be trained with this data.

Chapter 4

Carbon Foil

The carbon foil can be inserted at the target position in the reaction chamber. It is used for the H^- beam if neutral hydrogen is required, i.e. for a Lamb shift measurement of hydrogen. For this, it is useful to measure the thickness of the carbon foil as well as the distribution of the hydrogen scattered on the carbon foil.

4.1 Data used for the Carbon Foil Properties

4.1.1 Carbon Foil Thickness

To get the thickness of the carbon foil, the voltage on MCP5 was measured for 19 events, each with a H^- beam. Ten of these events had the carbon foil inserted, and the switchyard was on, meaning that only the neutral hydrogen could reach MCP5. The bias on MCP5 was set to 2.2 kV. For the other nine events the carbon foil was not inserted, and the switchyard was off, so that the charged beam could reach MCP5. The bias on MCP5 was set to 1.8 kV for the charged beam due to a much higher particle number reaching MCP5 than with the neutral beam. Otherwise, all beam steering parameters remained the same.

4.1.2 Scattering on the Carbon Foil

To try and get the distribution of particles scattered by the carbon foil on MCP5 the images taken during Dataset 3 (5.1.3) are used. During Dataset 3 there were 2397 images of MCP5 saved, each for a H^- beam with the carbon foil inserted and the same beam steering parameters. The bias on MCP5 was set to 2.2 kV for all these images.

4.2 Analysis Methods for the Carbon Foil

4.2.1 Carbon Foil Thickness

The thickness of the carbon foil can be determined by measuring the energy loss that particles passing through it experience. This energy loss can be determined by comparing the arrival times of the charged and neutral hydrogen beam at MCP5. For this the measurements from Section 4.1.1 are used. Since we are at low energies, relativistic

corrections for the velocities which are around 1 m/µs can be ignored. The kinetic energy of a single particle is thus given by

$$E_{kin} = \frac{1}{2}mv^2 \tag{4.1}$$

where m is the mass of the particle and

$$v = \frac{l}{t} \tag{4.2}$$

its velocity with $l = 1.69\,\text{m}$ the distance from the carbon foil at the target position to MCP5 and t the time it takes a particle to travel from the target position to MCP5. The difference in energy ΔE is

$$\Delta E = E_c - E_n \tag{4.3}$$

where E_c is the kinetic energy of the particles in the charged beam and E_n is the kinetic energy of the particles in the neutral beam. The relation between the thickness of a carbon foil and the energy loss has been determined in [5] to be

$$\Delta E = k\frac{d_f}{a_0 + a_1 E_c^{-0.4} + a_2 E_c^{0.25}} \tag{4.4}$$

where $k = 19.9$ is a unit conversion factor, d_f is the areal thickness of the foil and $a_0 = -37.19$, $a_1 = 178.1$ and $a_2 = 9.236$ are fit parameters from [5]. Thus, the areal thickness is given by

$$d_f = (a_0 + a_1 E_c^{-0.4} + a_2 E_c^{0.25})\frac{\Delta E}{k} \tag{4.5}$$

The only thing we have to determine from the voltage data of MCP5 is the arrival time of the beam. The beam arrival on MCP5 is visible as a large pulse in the voltage. Since the particles in the beam get scattered and the beam gets slowed down at the carbon foil, the pulse from the neutral beam should be both lower in voltage and wider than the pulse from the charged beam. If we take the timing of the maximum of the voltage pulse as the arrival time, we can ignore the different widths of the beam. Since we expect the pulse from the beam to be symmetric, we determine this maximum by fitting a Gaussian function to the voltage pulse. The position of the centre of this Gaussian is the time we are aiming to estimate. We do this for each of the 19 files and finally average the arrival time over the carbon foil in and out events separately.

4.2.2 Scattering on the Carbon Foil

4.2.2.1 Scattering of low Energetic Particles on a thin foil using Meyer's Theory [33]

There was a purely theoretical analysis done by L. Meyer in 1971 about the scattering of low energy heavy particles in thin solid layers. For thick layers, the calculations by Meyer

agree well with those of Molière [10], but for thin layers, as is the case for us, there are significant deviations. Meyer's theory is valid if

$$\alpha > 1\,; \quad \alpha = \frac{Z_1 Z_2}{137\beta} \tag{4.6}$$

where α is the Born parameter, Z_1 and Z_2 are the atomic numbers of the incident and scattering particles and $\beta = \frac{v}{c}$ is the ratio of the incoming particle velocity v to the velocity of light $c = 3.00 \times 10^8\,\mathrm{m/s}$. This is equivalent to

$$E_i < A_1 Z_1^2 Z_2^2 \times 25\,\mathrm{keV} \tag{4.7}$$

where E_i is the energy of the incident particles and A_1 the mass number of the incident particles.

For the calculations of the scattering distribution, we first define the screening parameter

$$a = \frac{0.885\,a_0}{\left(Z_1^{2/3} + Z_2^{2/3}\right)^{1/2}} \tag{4.8}$$

where $a_0 = 0.529 \times 10^{-8}\,\mathrm{cm} = 0.529\,\text{Å}$ is the Bohr radius. We also define the reduced energy

$$\varepsilon = \frac{a}{b}\,; \quad b = \frac{Z_1 Z_2 e^2}{2\pi\varepsilon_0}\frac{m_1 + m_2}{m_1 m_2 v^2} \tag{4.9}$$

where m_1 and m_2 are the masses of the incident and scattering particles, $e = 1\,\mathrm{e}$ is the elementary charge and $\varepsilon_0 = 55.3\,\mathrm{e^2 eV^{-1} \mu m^{-1}}$ is the vacuum permittivity. Equation (4.9) can also be written as

$$\varepsilon = E_i \frac{4\pi\varepsilon_0 a}{Z_1 Z_2 e^2}\frac{m_2}{m_1 + m_2}. \tag{4.10}$$

Next, we define r_0 as half the distance of neighbouring carbon atoms in the foil

$$r_0 \approx \frac{1}{2} N^{-1/3} \tag{4.11}$$

where N is the number of atoms per volume in the foil. Then we define $n = \pi r_0^2 N t$ where t is the thickness of the foil. Using the areal thickness of the foil d_f, n can be written as $n = \pi r_0^2 N_w d_f$ with the number of atoms per unit mass in the foil $N_w = \frac{1}{m_2}$. The reduced thickness of the foil τ is defined as

$$\tau = \frac{a^2}{r_0^2} n = \pi a^2 N t = \pi a^2 N_w d_f. \tag{4.12}$$

Using τ the half width angle of the scattered particles can already be determined with

$$\tilde{\vartheta}_{1/2} = g_1(\tau) + \frac{a^2}{r_0^2} g_2(\tau) \tag{4.13}$$

where the functions g_1 and g_2 were calculated by Meyer and are given in Table 1 and $\tilde{\vartheta}_{1/2}$ is the reduced half width angle. To get the actual angle from the reduced angle, we use

$$\vartheta = \frac{2}{\varepsilon}\frac{\tilde{\vartheta} m_2}{m_1 + m_2}. \tag{4.14}$$

The distribution of the scattered particles is now given by

$$F(\tilde{\vartheta}) = \frac{\varepsilon^2}{8\pi}\left(\frac{m_1 + m_2}{m_2}\right)^2 \left[f_1(\tau, \tilde{\vartheta}) - \frac{a^2}{r_0^2} f_2(\tau, \tilde{\vartheta})\right] \tag{4.15}$$

where f_1 and f_2 are the functions

$$f_1(\tau, \tilde{\vartheta}) = \int_0^\infty exp\left[-\tau\Delta(z)\right] J_0(\tilde{\vartheta} z) z dz \tag{4.16}$$

and

$$f_2(\tau, \tilde{\vartheta}) = \frac{\tau}{2}\int_0^\infty exp\left[-\tau\Delta(z)\right] J_0(\tilde{\vartheta} z)\Delta^2(z) z dz \tag{4.17}$$

with

$$\Delta(z) = \int_0^\infty \frac{f(\eta)}{\eta^2}\left[1 - J_0(z\eta)\right] d\eta. \tag{4.18}$$

The function $f(\eta)$ was calculated by Meyer and is given in Table 2. For values of η between two values in the table, a linear evolution between the next highest and lowest values in the table is assumed. Additionally, J_0 is the zero order Bessel function of the first kind.

4.2.2.2 Scattering obtained using the Scattering Constant from Allegrini [5]

In [5] the scattering half width angle was measured for nine carbon foils with different nominal thicknesses, ranging from 0.5 µg/cm^2 to 2 µg/cm^2. If the thickness is calculated as described in Section 4.2.1, their areal thicknesses range from 1.6 µg/cm^2 to 2.9 µg/cm^2. Hydrogen ions with energies from 1 keV to 50 keV were used for the incoming particles. From Meyer's theory follows that the half width angle $\vartheta_{1/2}$ at constant incident particle energy E_i is proportional to the areal thickness of the foil d_f. This means that

$$k_F = \vartheta_{1/2} E_i \tag{4.19}$$

is proportional to the foil thickness and is called the scattering constant. With the foils in [5] it was shown that

$$d_f = 0.153\, k_f\,; \quad k_f = 6.52\, d_f \tag{4.20}$$

This means that if we know d_f and E_i, we can use (4.19) and (4.20) to get $\vartheta_{1/2}$ with the equation

$$\vartheta_{1/2} = \frac{k_f}{E_i} = \frac{6.52\, d_f}{E_i}. \tag{4.21}$$

Using $\vartheta_{1/2}$ and Equation(4.13) the distribution from Equation(4.15) can be determined for the half width angle found here.

4.2.2.3 Distribution of the Particles on MCP5

To look for the distribution of particles scattered on the carbon foil on MCP5, the measurements from Section 4.1.2 are used. A particle is visible on the MCP5 images as a spot where the pixels have a higher value than normal, which can be seen as a cluster on MCP5. A cluster is defined as described in Section 3.2. The threshold for a pixel to be considered part of a cluster is chosen to be the average of the pedestal file plus three times the standard deviation of the pixels in the pedestal file. Usually clusters correspond to single particles, but if two particles impact on MCP5 too close to each other their clusters merge together, and they are only counted as a single particle.

To get the particle distribution, each pixel is averaged for the 2397 events. We then subtract the average value from a pedestal file μ_{ped} from each pixel and set all pixel values below zero to zero, giving us the matrix V_{dist}. Since we are only interested in the pixels which are part of the MCP, all pixel values outside the MCP region are set to zero. The dimensions of MCP5 are the same as in Section 3.2. Also, for each image, all pixels which are not part of a cluster are set to zero.

When looking at V_{dist}, we may see some unexpected features in the MCP. For example, if there is a crack in the MCP, this can be seen as an area with higher voltage than the average. We may also see some areas with much lower voltage than the average. This can happen if the channels in the MCP somehow get blocked, so no electron showers can be started, or the phosphor screen has some problem in that area. These features need to be considered in the analysis.

At this point, a two-dimensional Gaussian of the form

$$f_{2D}(x,y) = Ae^{-\frac{1}{2}\left(\frac{(x-\mu_1)^2}{b^2}+\frac{(y-\mu_2)^2}{c^2}\right)} \tag{4.22}$$

is fit to V_{dist}. The position of the maximum of f_{2d} will be at the pixel with position (μ_1, μ_2).

It is also a possibility to try and create a gain map of MCP5 with the images. The purpose of this gain map is not to correct for damages in the MCP, such as cracks, but to determine if clusters in different areas of the MCP trigger different voltages. The gain map can be obtained by going through each picture, setting all pixels which are not part of a cluster to 0, subtracting the average of the pedestal file from the remaining pixels and taking the sum over all of these matrices. For each pixel the number of pictures in which

it is part of a cluster is also counted and the summed matrix from before is divided by these values. Effectively, we now have for each pixel the average value that it has if it is part of a cluster. We now take the average value of all pixels which are part of MCP5 and divide each pixel with this value. With this matrix, we see how much gain there is for each pixel in comparison to the average gain of the pixels on MCP5. To smooth out this matrix it is averaged over blocks of 10×10 pixels and the resulting matrix is used as the final gain map V_{gain}. To get the charge distribution while accounting for the gain map, each element of V_{dist} is multiplied by the corresponding element in V_{gain}.

4.3 Carbon foil Results

4.3.1 Results for the Thickness of the Carbon Foil

The voltage of MCP5 averaged over the ten events with the carbon foil in and out, as well as the Gaussian fits to these voltages, can be seen in Figure 4.1. Averaging the maxima of the Gaussian fits over the events with a charged beam gives the time $t_{mc} = (5.30 \pm 0.01)\,\mu s$ and for the events with a neutral beam $t_{mn} = (5.42 \pm 0.01)\,\mu s$ where t_{mc} and t_{mn} are the times that the beam centre hits the MCP5 from the start of the voltage measurement. The uncertainties are chosen to be one standard deviation of the times over which we average. To get the charged and neutral beam travel time from the target to MCP5 t_c and t_n we use the energy of the particles in the charged beam $E_c = 6\,keV$. With Equation(4.1) we get the speed of the particles in the charged beam $v_c = 1.07\,m/\mu s$. This means that $t_c = \frac{l}{v_c} = 1.58\,\mu s$ and the beam arrives at $t_{target} = t_{mc} - t_c = (3.72 \pm 0.01)\,\mu s$ at the target in the timescale of the MCP5 voltage measurement. With this we get $t_n = t_{mn} - t_{target} = (1.70 \pm 0.01)\,\mu s$ and thus, with Equation(4.2) we get the speed of the particles in the neutral beam $v_n = \frac{l}{t_n} = (1.00 \pm 0.01)\,m/\mu s$.

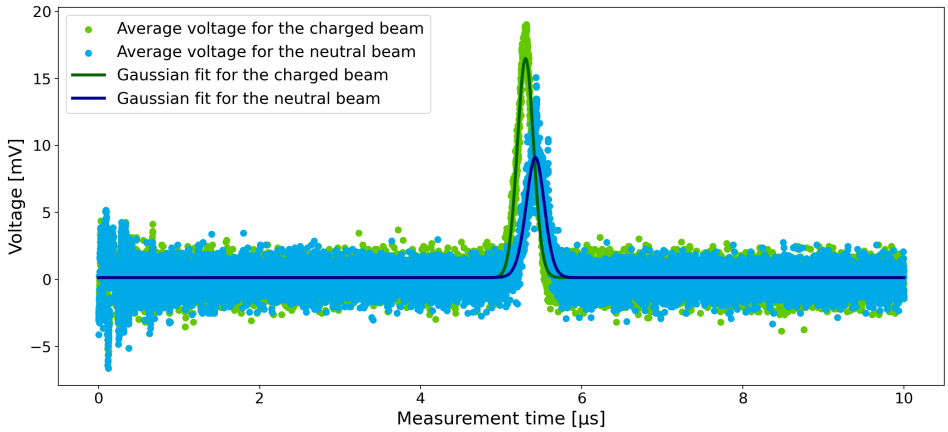

Figure 4.1: Averaged voltage of the MCP5 over time over nine events for the H^- beam with the carbon foil out (light green) and ten events for the H^- beam with the carbon foil in (light blue). Gaussian fits to the voltage pulses caused by the beam can be seen in dark green for the charged beam and in dark blue for the neutral beam.

With Equation(4.1) we get $E_n = (5.18 \pm 0.09)\,\text{keV}$ which gives us the energy loss in the carbon foil $\Delta E = (0.82 \pm 0.09)\,\text{keV}$. Using Equation(4.5) we get the areal thickness of the carbon foil $d_f = (2.64 \pm 0.28)\,\mu\text{g/cm}^2$. With the density of a typical carbon foil $\rho_{cf} = (2.01 \pm 0.02)\,\text{g/cm}^3$ taken from [8] we get the thickness of the foil $d_t = \frac{d_f}{\rho_{cf}} = (1.31 \pm 0.14) \times 10^{-6}\,\text{cm} = (131 \pm 14)\,\text{Å}$. From [29] we get that the thickness of each layer of carbon atoms is about 3.7 Å, which would mean that there are $\frac{d_t}{3.7\,\text{Å}} = 35 \pm 4$ layers of carbon atoms.

4.3.2 Results for the Scattering on the Carbon Foil

4.3.2.1 Scattering obtained using Meyer's Theory [33]

We first have to test if we are in the correct regime to use Meyer theory by checking that Equation (4.6) and (4.7) are valid. In our case with incoming H^- particles scattered on carbon particles we have $E_i = 6\,\text{keV}$, $Z_1 = 1$, $Z_2 = 6$ and $A_1 = 1$. With these values, Equation(4.7) becomes

$$6\,\text{keV} < 1 \times 1^2 \times 6^2 \times 25\,\text{keV} = 900\,\text{keV} \tag{4.23}$$

so we are in the Regime for the Meyer theory. Additionally, using Equation(4.1) we have a velocity of the incoming hydrogen ions of $v = 1.07 \times 10^6\,\text{m/s} = 1.07\,\text{m/µs}$. Using Equation(4.6) this gives us a Born parameter of

$$\alpha = \frac{1 \times 6}{137 \times \frac{1.07 \times 10^6\,\text{m/s}}{3.00 \times 10^8\,\text{m/s}}} = 12.25 \tag{4.24}$$

which is also in agreement with the criteria $\alpha > 1$.

Now we can start the actual calculations. In Equation(4.8) we get a value for the screening parameter of $a = 0.226\,\text{Å}$. From this we calculate in Equation(4.9) $b = 1.56 \times 10^{-10}\,\text{cm}$ which gives us the reduced energy $\varepsilon = 14.4$. In the calculation of r_0 in Equation(4.11) we need to determine the number of atoms per volume in the foil N. This can be done by using the density of a typical carbon foil of $\rho_{cf} = (2.01 \pm 0.02)\,\text{g/cm}^3$ taken from [8] and the mass of a single carbon atom m_2. This gives $N = \frac{\rho_{cf}}{m_2} = (1.01 \pm 0.01) \times 10^{23}\,\text{atoms/cm}^3$. With this we get $r_0 = 1.07 \times 10^{-8}\,\text{cm}$. Next, we get the reduced foil thickness from Equation(4.12) $\tau = 2.12 \pm 0.22$. We can now plug τ into the functions g_1 and g_2 to get $g_1(\tau) = 0.602 \pm 0.052$ and $g_2 = 0.583 \pm 0.016$. We can now use Equation(4.13) to get the reduced scattering half width angle $\tilde{\vartheta}_{1/2} = 0.628 \pm 0.052$. Finally, we can use Equation(4.14) to get the scattering half width angle $\vartheta_{1/2} = (4.59 \pm 0.38)^\circ$.

To get the full distribution $F(\vartheta)$ given in Equation(4.15) we need to evaluate the functions f_1, f_2 and $\Delta(z)$ which are given in the Equation (4.16), (4.17) and (4.18). Each of these functions contains an integral, all of which are approximated using Simpson's rule. The

half width angle of this distribution is at $\vartheta_{1/2}^{M} = (4.58 \pm 0.48)^\circ$. Once we have $F(\vartheta)$, we calculate the particle distribution at the plane of MCP5 with

$$F(h) = F\left(\tan^{-1}\left[\frac{h}{l}\right]\frac{360}{2\pi}\right) \tag{4.25}$$

where h is the distance from the scattering centre in the plane of MCP5 and $l = 1.69\,\mathrm{m}$ is the distance from the target position to MCP5. We can see this distribution in the blue curve in Figure 4.2. Since the distribution is spherically symmetric and MCP5 is circular with a radius of 2 cm we get the percentage of particles on MCP5 by evaluating the integral of $F(h)$ from $h = -2\,\mathrm{cm}$ to $h = 2\,\mathrm{cm}$ which gives us the value $\int_{-2}^{2} F(h)dh = (12.4 \pm 1.4)\,\%$ if we assume that the beam centre is at the middle of MCP5. $F(h)$ has a full width at half maximum (FWHM) of $(27.0 \pm 2.8)\,\mathrm{cm}$. Furthermore, $F(\vartheta)$ has a standard deviation of $\sigma^{M} = (4.64 \pm 0.35)^\circ$.

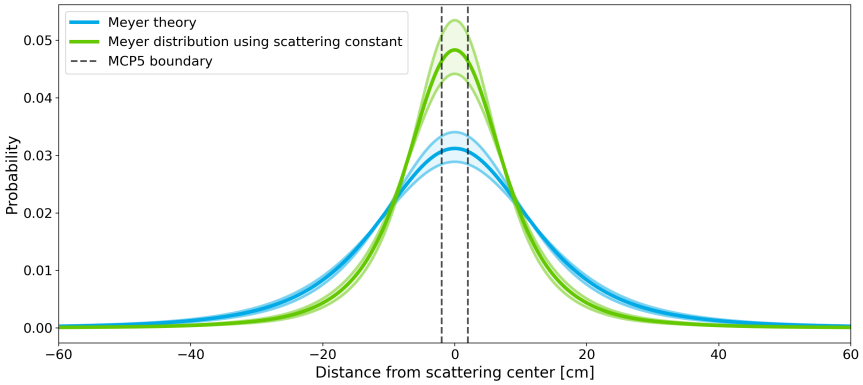

Figure 4.2: Distributions of the H^- beam after passing through the carbon foil at MCP5. We get the blue curve by using Meyer's theory 4.2.2.1 and the green curve by using the scattering constant k_F 4.2.2.2. The shaded areas show the uncertainties of the two distributions. The black dashed lines at $\pm 2\,\mathrm{cm}$ mark the area that MCP5 covers, with the assumption that the beam centre is at the middle of MCP5. The blue curve has a FWHM of $(27.0 \pm 2.8)\,\mathrm{cm}$ and (12.4 ± 1.4) percent of it is on MCP5, while the green curve has a FWHM of $(17.0 \pm 2.1)\,\mathrm{cm}$ and $(19.0 \pm 2.5)\,\%$ of it is on MCP5.

4.3.2.2 Scattering obtained using the Scattering Constant from Allegrini [5]

With Equation(4.20) we get the scattering constant $k_F = (17.5 \pm 1.8)\,\mathrm{keV}^\circ$. With Equation(4.21), the half width scattering angle $\vartheta_{1/2}^{A} = (2.91 \pm 0.31)^\circ$ is obtained. The areal thickness of the foil d_f^A required in Meyer's theory to get $\vartheta_{1/2}^{A}$ is obtained using Equation(4.13) resulting in $d_f^A = (1.52 \pm 0.18)\,\mu\mathrm{g/cm}^s$. With d_f^A, the particle distribution in the plane of MCP5 $F^A(h)$ can be calculated similarly to Section 4.3.2.1. This distribution can be seen as the green curve in Figure 4.2 and has a FWHM of $(17.0 \pm 2.1)\,\mathrm{cm}$, which corresponds to a half width angle of $\vartheta_{1/2}^{A} = (2.88 \pm 0.36)^\circ$. If we assume that the beam centre is at the middle of MCP5, we have $\varrho^A = (19.0 \pm 2.5)\,\%$ of the total particles on MCP5. Furthermore, with this distribution we have a standard deviation of $\sigma^A = (3.46 \pm 0.34)^\circ$.

4.3.2.3 Faults and Gain Map of MCP5

Before working with the voltage distribution in the pictures of MCP5, we look for features in the MCP which need to be compensated and a gain map of MCP5 is created as described in Section 4.2.2.3.

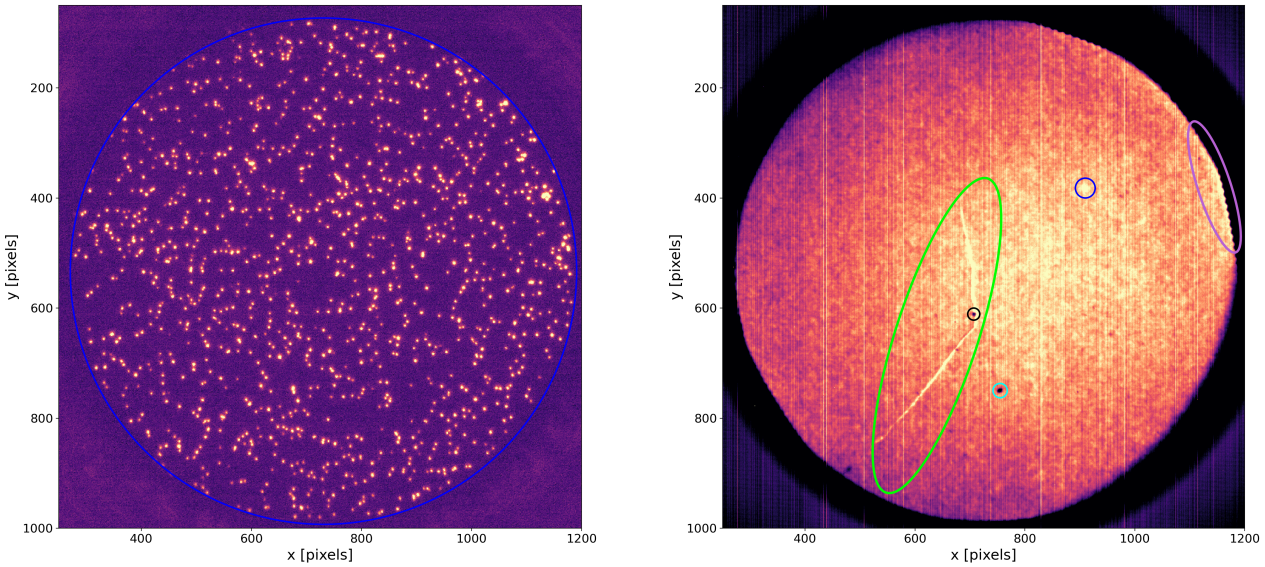

(a) Typical image of MCP5 for an event in Dataset 3. The clusters are the yellow areas and the blue circle is the approximate area that MCP5 covers. For this event the H^- beam had an intensity of 9.47×10^6 Particles and there were 1042 clusters detected.

(b) Average value of all the pixels contained in a cluster for all images of MCP5 from Dataset 3. The colored outlines highlight some visible faults in the MCP. The black and light blue circles show areas where no voltage was detected. The dark blue circle shows an area where there were abnormally high voltages. The green ellipse shows a crack in the MCP around which too high voltages were recorded. On the top right edge of the MCP we can see that there are high voltages, the worst are is highlighted in the purple ellipse. There are also some bright yellow vertical lines visible which are artifacts from the CCD camera used to record the images.

Figure 4.3: Pictures of MCP5 from Dataset 3.

A picture of V_{dist} from Section 4.2.2.3 is shown in Figure 4.3b. Some Features in the MCP are clearly visible. The bright line marked by the light green ellipse is a crack in MCP5. Similarly, a bright area can be seen in the dark blue circle, most likely also caused by damage in the MCP. Both these features result in an increased voltage measured by the phosphor screen. In the light blue and black circle there are dark spots, meaning that the phosphor screen measured voltages that are too low. These could be caused either by the channels in MCP5 being blocked over those spots or some problem with the phosphor screen. We can also see that there are a lot of bright spots corresponding to high voltages on the top right side of the MCP. They could be caused by damage along the edge of the MCP, or there could also be an increase in the gain of the MCP going further right. The

dark spots are not too problematic, since they are quite small and any pixels with value zero are ignored in the analysis. The bright spot in the blue circle is also no problem since it is small, and we can see in the gain map in Figure 4.5 that this gets compensated. Similarly, the bright areas on the right of the MCP can be seen in the gain map and thus will also get corrected. The pixels in the crack need to be determined separately as they do not have a high gain when a particle impacts on the MCP close to them, but the measured background voltage is higher on average for them.

In Figure 4.3b we can also see some vertical lines which are artefacts from the CCD camera. To determine which ones are the most problematic, the average value of each column of pixels contained by the MCP is taken. The columns with an average value of at least 41.5, which are a total of 17 rows, are all set to 0 to get rid of the most problematic ones.
To get the pixels affected by the crack, we use the image seen on the left side of Figure 4.4. In this image, we search for clusters above a threshold of 880 and with 50 as the minimum number of pixels in the cluster. We get three clusters containing a total of 3342 pixels. We call the pixels affected by the crack P_{crack}. An image of P_{crack} can be seen on the right side of Figure 4.4. For the determination of the voltage distribution on MCP5, all these pixels are set to zero.

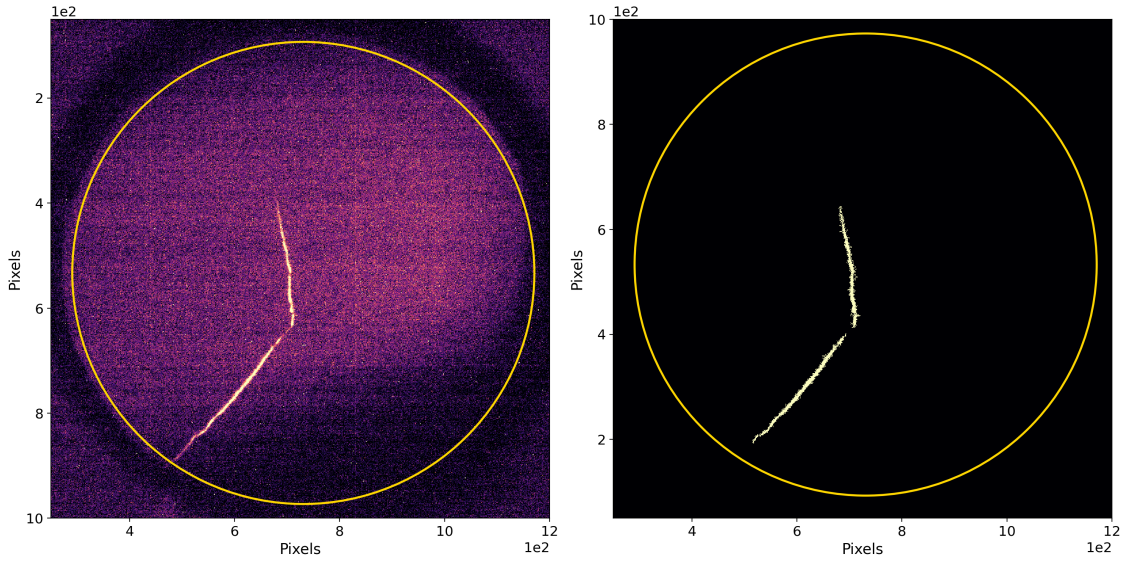

Figure 4.4: On the left is the picture of MCP5 from which the pixels affected by the crack P_{crack} can be extracted. On the right is an image of the pixels in P_{crack}. The yellow circle in both pictures is the approximate area of MCP5.

A picture of the gain map V_{gain} can be seen in Figure 4.5. V_{gain} was obtained as described in 4.2.2.3 with the addition that the pixels in P_{crack} were set to zero before averaging over every 10×10 block of pixels. To compensate for this, the average of each 10×10 block was calculated by summing over all 100 pixels part of the block, but only dividing this

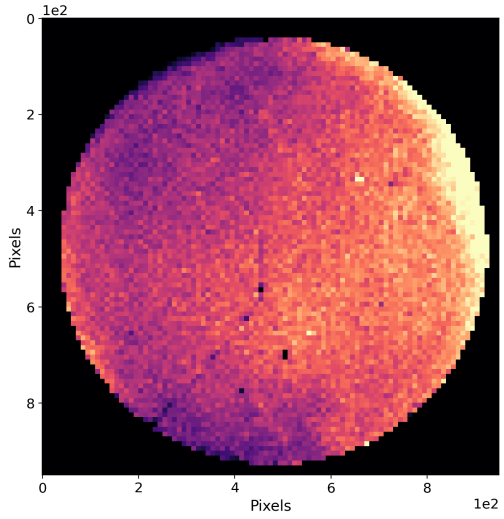

Figure 4.5: On the left is the picture of MCP5 from which the pixels contained in the crack were extracted. On the right is an image of the specific pixels that we define to be part of the crack. The yellow circle in both pictures is the approximate area of MCP5.

number by the number of pixels unequal to zero in the block. This means that before dividing V_{dist} by V_{gain} all pixels in P_{crack} must be set to zero in V_{dist}.

4.3.2.4 Distribution of the Particles on MCP5

To get the V_{dist} we follow the steps in Section 4.2.2.3. An example of the image of MCP5 of one event of Dataset 3 can be seen in Figure 4.3a. For this specific event, a total of 1042 clusters were detected and there was a beam intensity from ELENA of 9.47×10^6 Particles. When averaging over all MCP5 pictures of Dataset 3 we get the image in Figure 4.3b. Next, the pixels in P_{crack} and the pixels in the columns with an average value above 41.5 are all set to zero as described in Section 4.3.2.3. All pixels outside MCP5 also get set to zero. The resulting matrix is the charge distribution over MCP5 V_{dist}. For now, the gain map of MCP5 is ignored. Now, a two-dimensional Gaussian $f_{2D}(x, y)$ of the form seen in Equation(4.22) is fit to V_{dist}. The fit parameters for f_{2D} that were found are $A = 45.35 \pm 0.01$, $b = 693.6 \pm 0.5$, $c = 528.5 \pm 0.2$, $\mu_1 = 861.0 \pm 0.2$ and $\mu_2 = 531.4 \pm 0.1$. Given these values, the beam centre would be placed at the position (861.2,531.4).

Since we want to get the probability distribution of the voltage p_{2D}, the integral of $f_{2D}(x, y)$ needs to be determined. To do this, the integral of $f_{2D}(x, y)$ is calculated using Simpson's rule where y is constant and x is in the array x_{arr}. This step is repeated for different values of y, which are in the array y_{arr}. Both x_{arr} and y_{arr} are constructed such that the difference between two neighbouring values x_d and y_d is always the same. We call their minimum and maximum x_0, x_1, y_0 and y_1 and their lengths x_l and y_l. The integral can now be calculated with

$$\int_{-\infty}^{\infty}\int_{-\infty}^{\infty} f_{2D}(x,y)\,dx\,dy \approx \int_{y_0}^{y_1}\int_{x_0}^{x_1} f_{2D}(x,y)\,dx\,dy \approx y_d \sum_{i=0}^{y_l} simpson(f_{2D}(x_{arr},y_i)) \quad (4.26)$$

The specific values were found through some testing and they are: $x_0 = y_0 = -4000$, $x_1 = y_1 = 6000$ and $x_d = y_d = 100$. This means that we have $x_l = y_l = 101$. With this, we get the values for the integral $I_{2D} = 9.000 \times 10^7$. The probability distribution is now given by $p_{2D}(x,y) = f_{2D}(x,y)I_{2D}^{-1}$. To get the percentage of particles hitting MCP5, p_{2D} has to be integrated over the area of MCP5

$$\iint_{MCP5} p_{2D}(x,y)\,dx\,dy = 22.7 \pm 1.6_{\text{sys}}\,\%. \quad (4.27)$$

We repeat all of this now while accounting for the MCP5 gain map V_{gain} that was constructed in Section 4.3.2.3 and can be seen in Figure 4.5. The only change we have to make is to multiply each pixel in V_{dist} by the corresponding one in V_{gain} before calculating the fit of the two-dimensional Gaussian distribution f_{2D}. From the fit we obtain the parameters $A = 44.72$, $b = 661.4 \pm 0.4$, $c = 558.4 \pm 0.2$, $\mu_1 = 811.9 \pm 0.2$ and $\mu_2 = 531.4 \pm 0.1$. Given these values, the beam centre would be placed at the position (818.7,532.3). To get the percentage of particles that we see on MCP5 we follow the same steps as before and get

$$\iint_{MCP5} p_{2D}(x,y)\,dx\,dy = 22.9 \pm 0.9_{\text{sys}}\,\%. \quad (4.28)$$

4.4 Discussion of the Carbon Foil Properties

4.4.1 Carbon Foil Thickness

The carbon foil thickness of $(2.64 \pm 0.28)\,\mu g/cm^2$ is relatively thin and should provide a good amount of hydrogen. Counting the clusters on MCP5, there are around 600 particles detected per event in Dataset 1. In comparison, the carbon foil used in 2022 resulted in an energy loss of around 3.8 keV and had a thickness of around $12\,\mu g/cm^2$. As a result of this, the particles were distributed over a wider area. Around 30 particles were detected on MCP5 for a typical event. These numbers are heavily influenced by the beam intensity and the beam steering, so they cannot be compared directly to each other, but the huge increase in the number of particles is promising.

4.4.2 Scattering on the Carbon Foil

The results for the scattering on the carbon foil vary significantly depending on the method is used. One important remark is that the exact composition of our carbon foil is not known. For example, the Arizona Carbon Foil company states in [8] that their carbon foils have an approximate composition of 1 atomic percent oxygen, 3-5 atomic percent hydrogen and a few atomic percent sodium with the rest being carbon. The foils tested

in [5] have a composition of 12 atomic percent oxygen and 88 atomic percent carbon. In Section 4.3.2.1 it was assumed that our foil is 100 percent carbon, which is quite unlikely. If the composition from [5] is used and all other parameters stay the same and (4.15) is calculated again, a half width angle of $(4.58 \pm 0.38)^\circ$ is obtained and $(12.4 \pm 1.0)\,\%$ of the particles are hitting MCP5 if the beam centre is in the middle of MCP5. These are the same values as for 100 atomic percent carbon. The only difference is that the standard deviation of the new distribution is a bit higher than $\sigma^M = (4.64 \pm 0.35)^\circ$ at $(4.66 \pm 0.36)^\circ$. Thus, we can conclude that the composition is most likely not the cause of the different distributions.

Meyer provided in his paper [33] the values for $f_1(\tau, \tilde{\vartheta})$ and $f_2(\tau, \tilde{\vartheta})$ at distinct τ and $\tilde{\vartheta}$. We can now compare the values of $f_1(\tau, \tilde{\vartheta})$ and $f_2(\tau, \tilde{\vartheta})$ provided by Meyer to the ones calculated for this analysis. At three σ^M distance from the centre, we have an angle of $\vartheta_{3\sigma^M} = 13.9^\circ = 0.243\,\text{rad}$. Going $3\vartheta_{3\sigma^M}$ to either side from the centre includes 98 % of the distribution we get from Meyer's theory. The reduced angle at $\vartheta_{3\sigma^M}$ is given by $\tilde{\vartheta}_{3\sigma^M} = 1.90$. Similarly, for the distribution we get with the scattering constant we arrive at $\tilde{\vartheta}_{3\sigma^A} = 1.18$. So we are only interested in the values of f_1 and f_2 at a reduced angle, not much bigger than $\tilde{\vartheta}_{3\sigma^M}$ if τ is around $\tau^M = 2.12 \pm 0.22$ or $\tilde{\vartheta}_{3\sigma^A}$ if τ is around $\tau^A = 1.22 \pm 0.14$. For $\tau = 2.0$ the values of f_1 and f_2 at different reduced angles provided by Meyer and calculated in this analysis can be seen in Table 3. For $\tau = 1.2$ the same can be seen in Table 4. We can see that the values differ slightly and are generally slightly lower for the calculated ones. This does mean that we would get a bit more particles in the region of MCP5, however the differences are too small to influence the result significantly.

The percentage of particles on MCP5 when fitting the two-dimensional Gaussian agrees more or less with the one using the scattering constant. However, there are multiple factors that could be improved for this fit. Firstly, the method to determine the gain map here would greatly benefit from more statistics. It could also be interesting to compare the gain map with different beam steering parameters, as this should theoretically not affect it. Comparing the results with and without the gain map gives a very similar final result. The only part where we can see a major difference is the x-position of the centre of the distribution for which we get 861.0 without the gain map and 811.9 with the gain map. One solution to determine which values are better would be to take a couple of pictures of MCP5 of the H^- beam without the carbon foil. Since the centre of the beam with and without the carbon foil should be the same, if the centre of the charged beam could be determined, these values could be used in the fitting of the distribution. This could also be repeated before and after the pictures of the beam with the carbon foil in to see if there is any change in the beam trajectory. Also, it may not be ideal to use Gaussians for the fit, since the distributions given in Meyer's theory have a different shape. A comparison between the probability distribution we got in Section

4.3.2.1 and a Gaussian with the same standard deviation $\sigma = 13.7\,\text{cm}$ is illustrated in Figure 1. Furthermore, the choice of the pedestal file also influences our result. There are two pedestal files available for MCP5, both taken with identical parameters. The first one has an average value of the pixels on MCP5 of 806 and their standard deviation is 22.2. For the second one, we get an average of 809 and a standard deviation of 23.1. For the analysis, the first pedestal file was used. If we use the second pedestal file, we get that 24.3 % of the distribution is on MCP5 without the gain calibration and 23.8 % with the gain calibration. These discrepancies are considered in the systematical uncertainties.

Taking all of this into account, the calculations in this analysis are performed using the values found in Section 4.3.2.2 but the uncertainty of ϱ^A is increased to 4 % so as to incorporate the other results for the distribution. This means that $\varrho = (19 \pm 4)\,\%$ is used, which would correspond to the reduced foil thickness $\tau = 1.22 \pm 0.50$.

Chapter 5

Lamb Shift Setup Tests

For the tests of the Lamb shift setup presented here, the HFS was always off and only the MWS was used. As mentioned in Section 2.3.3 there are four MCPs used to detect Lyman alpha photons. They will occasionally be referred to as channel 1, 2, 3 and 4 from now on. We get the voltage over time from each of the four MCPs. For each shot from ELENA, the MCP voltages are measured for 10 µs. A particle impacting on an MCP is seen as a negative pulse in the voltage of the anode of the MCP. The value of the minimum of these pulses if often referred to as the pulse height. When comparing different pulse heights, lower and higher is always meant with respect to the absolute value of the pulse height. Higher energetic particles are associated with larger pulses, but the same particle at the same energy can result in two different pulse heights. This happens because a particle can penetrate the MCP to different depths until an electron shower is started. However, these pulse heights are still what we are mainly interested in and what should allow us to determine the transition energy.

In order to determine the transition energy, there are on the order of a couple of hundred events recorded for different microwave frequencies. Next, the heights and timings of the voltage pulses are determined for each event. Comparing the prevalence of the pulses depending on their height for different microwave frequencies should give us a lineshape which should look similar to the one in Figure 2.3 with which we can determine the transition energy.

5.1 Datasets from the Lamb Shift Setup

There were three different datasets taken which are relevant for the analysis. One where the MWS was either off or on set to a fixed frequency and two where the MWS was scanning over different frequencies. For each of these datasets, the bias for the four Lyman alpha MCPs was set to $-2.2\,\mathrm{kV}$.

5.1.1 Microwave on/off Dataset (Dataset 1)

For the first dataset, the MWS was either turned off or set to a frequency of 1060 MHz, which is the frequency for which we expect the most induced $2S_{1/2} \rightarrow 2P_{1/2}$ transitions.

MWS off and MWS on events were taken alternating in runs of 90 events each with a total of 13 repetitions. Comparing the data between the MWS being off and on allows us to make sure that the setup works and to determine the voltage range in the MCPs in which the pulses caused by Lyman alpha photons are. This voltage range should not change while the MCP bias stays the same, so it can also be used for the analysis of the scanning runs. Some more information about Dataset 1 can be seen in Table 5.1.

MWS frequency [MHz]	0	1060
Events	1169	1170
Pulses	10172	9804
Pulses per event	8.70	8.38
Total particles [millions]	10340	10269
Pulses per 1 million particles	0.984	0.955
Events with $n_I > 6$	1041	1029
Pulses in events with $n_I > 6$	9979	9557
Pulses per event with $n_I > 6$	9.59	9.29
Total particles from events with $n_I > 6$ [millions]	10154	10055
Pulses per 1 million particles from events with $n_I > 6$	0.983	0.950

Table 5.1: Information about the measurements in Dataset 1 where n_I is the particle beam intensity in million particles.

5.1.2 First Microwave Scanning Dataset (Dataset 2)

For this dataset, the MWS was set to the frequencies from 800 MHz to 1300 MHz with steps of 100 MHz for a total of six different frequencies. This was done in runs of 100 events for each frequency, starting at 800 MHz and going to 1300 MHz for 4 repetitions. Because of some mechanical problems the experiment had to be entered shortly after starting this sequence and thus most events in the first 800 MHz run and a few in the first 900 MHz run had no particles reaching the reaction chamber. Since mainly the 800 MHz run was affected, another 385 events were taken with the MWS set to 800 MHz. Some more information about Dataset 2 can be seen in Table 5.2.

5.1.3 Second Microwave Scanning Dataset (Dataset 3)

Similarly to Dataset 2 MWS was scanning between the frequencies 800 MHz to 1300 MHz with steps of 100 MHz. However, after each run with the MWS on, there was one run taken with the MWS off. Each of these runs consist of 100 events and in total two repetitions were made, so a total of 200 events for each frequency and 1200 events with the MWS off were measured. There is a steerer placed right after the reaction chamber which applies an electric field to the beam and deflects the charged particles. This steerer was on and set to a low voltage for Dataset 2 to reduce the noise from charged particles in the Lyman alpha MCPs. This might have already quenched the beam partially so that less Lyman alpha photons would be detected, so this steerer was off for the measurements in

MWS frequency [MHz]	800	900	1000	1100	1200	1300
Events	716	393	400	384	400	397
Pulses	9880	4644	4976	5027	4703	5173
Pulses per event	13.80	11.82	12.44	13.09	11.76	13.03
Total particles [millions]	5362	3018	2998	3088	3012	2958
Pulses per 1 million particles	1.84	1.54	1.66	1.63	1.56	1.75
Events with $n_I > 6$	623	350	348	338	346	343
Pulses in events with $n_I > 6$	9436	4444	4743	4762	4447	4894
Pulses per event with $n_I > 6$	15.15	12.70	13.63	14.09	12.85	14.27
Total particles from events with $n_I > 6$ [millions]	5201	2946	2909	3000	2910	2874
Pulses per 1 million particles from events with $n_I > 6$	1.81	1.51	1.63	1.59	1.53	1.70

Table 5.2: Information about the measurements in Dataset 2 where n_I is the particle beam intensity in million particles.

Dataset 3. All other parameters of the experiment were identical for the Datasets 2 and 3 so we should be able to combine them in the analysis. Some more information about Dataset 3 can be seen in Table 5.3.

MWS frequency [MHz]	0	800	900	1000	1100	1200	1300
Events	1198	199	198	200	199	200	200
Pulses	17342	2621	2778	2769	2773	2920	2865
Pulses per event	14.48	13.17	14.03	13.85	13.93	14.60	14.32
Total particles [millions]	10368	1713	1700	1682	1701	1712	1702
Pulses per 1 million particles	1.67	1.53	1.63	1.65	1.63	1.71	1.68
Events with $n_I > 6$	1167	189	188	192	195	192	192
Pulses in events with $n_I > 6$	17047	2526	2680	2677	2737	2838	2838
Pulses per event with $n_I > 6$	14.61	13.37	14.26	13.94	14.04	14.78	14.78
Total particles from events with $n_I > 6$ [millions]	10194	1657	1647	1639	1682	1670	1632
Pulses per 1 million particles from events with $n_I > 6$	1.67	1.52	1.63	1.63	1.63	1.70	1.74

Table 5.3: Information about the measurements in Dataset 3 where n_I is the particle beam intensity in million particles.

5.1.4 Data for the LEDs in front of the Lyman Alpha Detector

The four MCPs could have a different gain compared to each other. To study this, the four LEDs which are installed at the end of the microwave setup and in front of the Lyman alpha MCPs can be used. The LEDs emit photons with a wavelength of 265 nm to 280 nm and thus allow us to observe the pulses in the MCP voltages from a specific wavelength. Setting the MCP bias to different voltages also allows us to compare the spread of the pulses. For each of the three MCP biases $-2.0\,\mathrm{kV}$, $-2.1\,\mathrm{kV}$ and $-2.2\,\mathrm{kV}$ there were ten background measurements taken with the LEDs off and twenty with the

LED voltages set to 4.75 V. Each measurement lasts 1 ms and measures the voltage with 1 GHz frequency, so there are 10^6 frequencies saved for each measurement.

5.2 Lamb Shift Data Analysis Methods

5.2.1 Determining the Voltage Pulses in the Lyman Alpha MCPs

To analyze the measurements from Section 5.1 the pulses in the MCP voltages have to be determined. Unfortunately, this is not trivial. There are two main difficulties when trying to determine the pulses: Ringing in the MCP voltage after a particle impact and a lot of background, making individual pulses difficult to be distinguished from each other.

For the first problem, some pulses as seen in the voltage measurements of the Lyman alpha MCPs caused by single particles are depicted in Figure 5.1 as the black points for each of the four channels. There we can also see that a ringing in the voltages of the MCPs is produced after each pulse. This is especially bothersome because we expect the pulses created by Lyman alpha photons to be quite a bit lower than the highest pulses, which are most likely caused by background stray particles from the beam hitting the MCPs. So eliminating this ringing is quite important if we want to have precise measurements for the Lamb shift.

The second problem can be seen when searching for pulses which are very close together so that they cannot be clearly separated any more. This gets more relevant as we have more background. For a hydrogen beam this background is not too relevant, but for an antihydrogen beam there would be a lot more background, made up mainly of pions produced by annihilation of the antihydrogen.

Both of these problems have to be considered when analysing the voltages from the Lyman alpha MCPs. Some methods to counter them are presented in the Sections 5.2.1.1 and 5.2.1.2.

5.2.1.1 Ringing in the MCP Voltages from Particle Impacts

The ringing caused by a particle impact on an MCP is unique for each channel, but within a channel it stays very similar and only depends on the pulse height. Thus, for each channel, four events, which only had a single pulse with height above 80 mV, were combined to get the shape of the ringing. To do this, we take the ten measurement points before until 1000 measurement points after the voltage minima, which corresponds to around 0.01 µs before until 1 µs after the pulse. For each of these pulses we have to consider that we only measure the voltage at discrete times, around every 1 ns, and not continuously and thus the actual pulse height h_a and timing t_a could be different from the

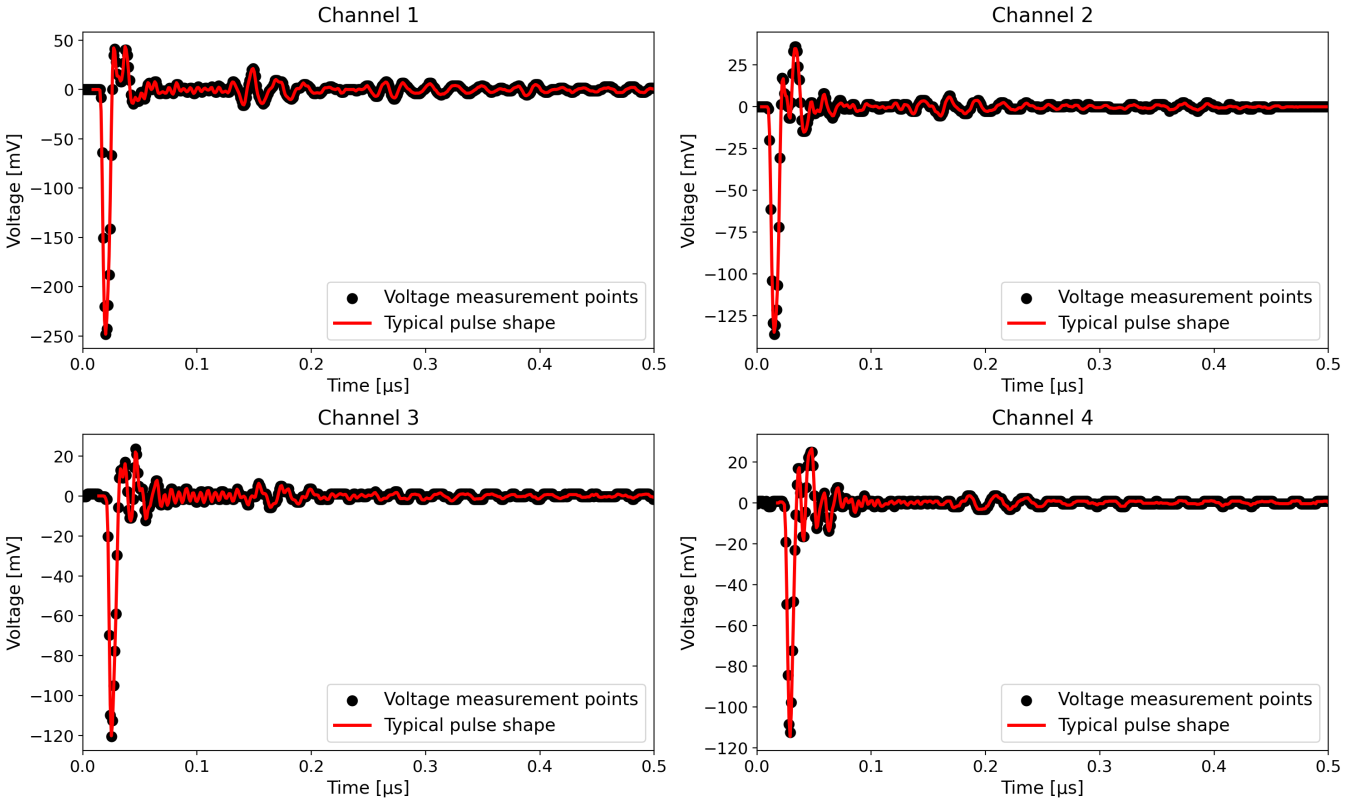

Figure 5.1: Pulse from single particles as seen on the four channels (black points) and the typical shape of a pulse and the following ringing in the voltage ς_{Ch} from a single particle impact (red).

minimum measured voltage. To find them, the shape of the pulse is determined, and a separate three-dimensional polynomial is fit to this shape for each interval of 1 ns. These go from 6 ns before to 6 ns after the minimum of the pulse. With all these polynomials, a function $\varsigma_{pulse-Ch}$ is created that takes the time and height of the maximum of the pulse as input. $\varsigma_{pulse-Ch}$ is different for each channel Ch. Now $\varsigma_{pulse-Ch}$ is fit to the measurement points using the $scipy.optimize.curve\_fit$ command in python [42] which returns the optimal parameters for the pulse height h_a and time t_a. Next the voltages of the pulses get scaled to the same height using h_a and they get combined to one array for each channel such that each of their pulse timings t_a is at the position 0. Similarly to before, each of these arrays is split into 1009 consecutive parts, each part for a time interval of 1 ns. Then a three-dimensional polynomial is fit to each of these intervals, which are then combined into one function for convenience. With this method we get a unique function ς_{Ch} for each channel which contains the typical shape of a pulse and the following ringing in the voltage for the channel Ch. ς_{Ch} takes h_a and t_a as input to scale it properly to any pulse we are looking at.

5.2.1.2 Distinguishing Pulses with a lot of Background

It is possible that two pulses on the same MCP are very close to each other in time, and thus the shape of a single pulse $\varsigma_{pulse-Ch}$ cannot be fit properly to the measured

voltages. If this is the case, then two pulses get fit to the measured voltages. This is done similarly as in Section 5.2.1.1 using the *scipy.optimize.curve_fit* command in python [42]. The function ς_{fit-Ch} which we want to fit to the measured voltages is the sum of two pulse shape functions of channel two $\varsigma^1_{pulse-Ch}$ and $\varsigma^2_{pulse-Ch}$. Thus, we search for the peak heights and timings of two pulses of which the sum is similar to the measured voltages. An example of this process in channel 2 can be seen in Figure 5.2. The blue and green curves are the shapes of the pulses from single particles $\varsigma^1_{pulse-2}$ and $\varsigma^2_{pulse-2}$, the pink curve their sum ς_{fit-2} and the black points the measured voltages which were used for the fit.

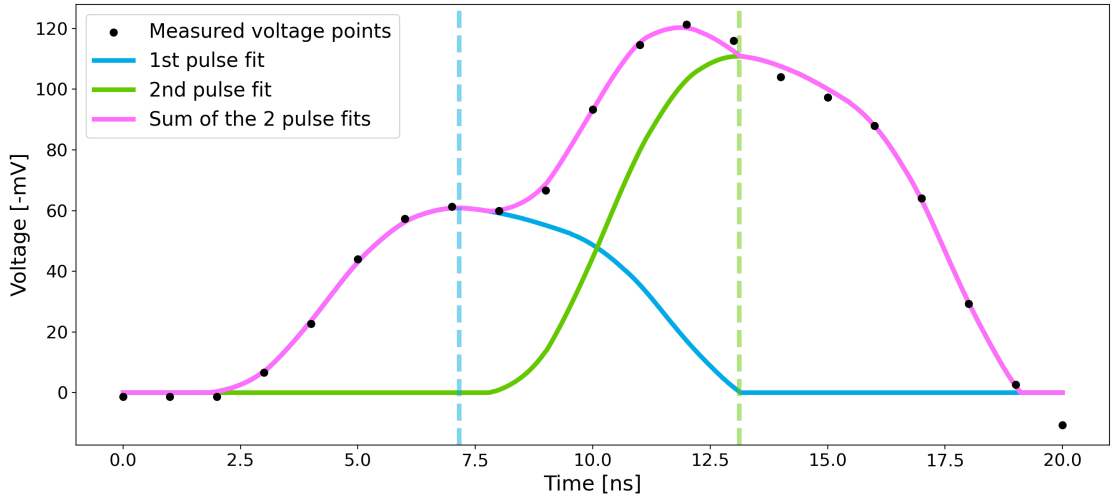

Figure 5.2: Measured voltages in channel 2 (black points) caused by multiple particle impacts on the MCP. The blue and green curves are the two pulses which have been found by fitting two pulse shapes $\varsigma^1_{pulse-2}$ and $\varsigma^2_{pulse-2}$ to the measured voltages. The two dashed lines indicate where the peaks of the pulses are. The pink curve is the sum of the two fit pulses ς_{fit-2}. The y-axis is given in negative voltage.

5.2.1.3 Final Determination of the Voltage Pulses

The actual determination of the pulses is done using the *scipy.signal.find_peaks* command in python [42]. This command takes an array of data and a minimum height as input. In our case, this array is just the negative of the voltage we get from the MCPs. The output contains two arrays, the first one containing the indices of all pulses that were found in the voltage array and the second one containing the voltage value at the indices from the first array so the height of the pulses.

In a first step, only pulses with height bigger than 30 mV are considered. This is done to remove the ringing caused by larger pulses as described in Section 5.2.1.1 before looking at smaller pulses which are heavily influenced by this ringing. For each channel, we start with the earliest pulse that was found. First, a pulse shape function $\varsigma^1_{pulse-2}$ similar to Section 5.2.1.1 is fit to the pulse in the voltage measurement. With this we find the

actual height and time of the pulse, and we can also calculate the squared difference of the voltage measurement and the fit curve divided by the height of the pulse. If this difference is big enough, we go through the procedure described in Section 5.2.1.2 and get a second difference using the fit curve similar to the first difference. Depending on these two differences either the fit for one pulse or for two pulses is used or if they are both too big the pulse gets discarded. As long as the pulse does not get discarded we get a value for the pulse height h_a and time t_a from the fit which we save in an array. We can now subtract $\varsigma_{Ch}(h_a, t_a)$ from the measured voltage. After this, the $scipy.signal.find\_peaks$ command is used again and this procedure gets repeated until there are no more pulses above 30 mV found.

At this point, we use the $scipy.signal.find\_peaks$ command to search for pulses below 30 mV. Similarly to larger pulses, $\varsigma^1_{pulse-Ch}$ gets fit to the pulse and depending on how well it fits the measurement the pulse will either be discarded or saved. It was found that the method described in Section 5.2.1.2 was unreliable for small pulses, and thus this the two-pulse fit is not done for pulses below 30 mV. There are also two more criteria which we have to consider. The first being that because of some crosstalk in the experiment there are periodic oscillations in the first 3 µs of the measured voltages, and thus we discard any pulses smaller than 30 mV before this time. This not a problem since the beam should never arrive this early at the Lyman alpha detector, it usually arrives around 1.8 µs later. For the second, we only look at pulses that are either below 15 mV or closer than 10 ns to a pulse above 30 mV. We calculate the least square difference divided by the pulse height between the fit and the measured voltage again but this time from 8 ns before until 18 ns after the pulse and discard the pulse if this difference is not very small. This is done because very small pulses are often very similar to the fit, even if they are clearly caused by noise.

We have to go through this for each shot we get from ELENA and measure Lyman alpha data. The pulse heights and timings for each shot get put into a pandas Dataframe [36] for further analysis.

5.2.2 Analysis of the Signals on the Lyman Alpha MCPs from the LEDs

The data from the LEDs is taken as described in Section 5.1.4. The measurements for the voltage of the Lyman alpha MCPs gets evaluated similarly as described in Section 5.2.1. The key differences are that each measurement is now 1 ms long, and we expect the pulses to be evenly distributed across the whole measurement, so we do not perform any time cuts. The noise in the MCP voltages due to cross talk is also not present in these measurements. Furthermore, we are now very interested in pulses with a low height (below 20 mV) to observe the signals in this region. We have little to no background from massive particles, so there should be very few very high pulses (above 150 mV) which would cause a lot of noise. To attempt and accurately determine as many pulses

as possible, we first only search for pulses with height greater than h_1, save them and subtract their noise given by ς_{Ch} from the data. Once there are no pulses above h_1 left, this is repeated for pulses with height greater than h_2. Now that there are only low pulses left and the noise from the higher pulses is eliminated, we search for any remaining pulse above h_3 without taking their noise ς_{Ch} into account. We only keep pulses in this last step that are more than 10 ns distant from any pulses higher than h_2.

Another feature in the pulse height distribution is that we should see the pulses detected from noise. The correction with ς_{Ch} is not perfect and still leaves a bit of noise and if we set h_3 low enough both the remaining noise from ς_{Ch} and the background fluctuations in the voltage are also be counted as pulses. These noise pulses should fall off exponentially so we can see them nice in the pulse height distribution and can define for each channel and bias the voltage value above which the noise pulses should be negligible.

5.2.3 Estimating the Number of Clusters on MCP5 depending on the Beam Intensity

For Dataset 1 there were one 24 images of MCP5 saved out of 2339 events. It would be interesting to try and estimate the number of clusters on MCP5 depending on the beam intensity for the events which do not have an image saved for them. For this, the MCP5 images from Section 4.1.2 are used. The number of clusters found on MCP5 for the events in Dataset 3 and the beam intensity of the corresponding event can be seen in Figure 5.3b. The number of clusters depending on the beam intensity I_e behaves similarly to a function of the form

$$C(I_e, A, \mu) = A\frac{I_e}{I_e + \mu}. \tag{5.1}$$

Using the $scipy.optimize.curve_fit$ command in python [42] the fit parameters for Dataset 3 $A_3 = (1.93 \pm 0.12) \times 10^3$ and $\mu_3 = 7.62 \pm 1.02$ can be obtained. This fit is illustrated in Figure 5.3b. Using the 24 pictures from Dataset 1 and applying the same fit gives the parameters $A_1 = (1.07 \pm 0.14) \times 10^3$ and $\mu_1 = 8.27 \pm 2.27$. Both the data points of the 24 pictures from Dataset 1 and the fit are illustrated in Figure 5.3a.

5.2.4 Analysis of the Lyman Alpha Pulse Data

5.2.4.1 Time of Flight (TOF) Cuts

For each event we have the voltage over time of MCP5. Because the neutral beam impacts on MCP5 at the end of the beam line, there is a voltage pulse visible. Since there are a lot of particles colliding with the MCP in a short time frame, we have only one continuous voltage pulse. The width of this pulse gives us the length of the beam. We can now use the distance from the Lamb shift setup to MCP5 together with the speed of the neutral beam, which was found in Section 4.3.1, to get the time during which the beam passes

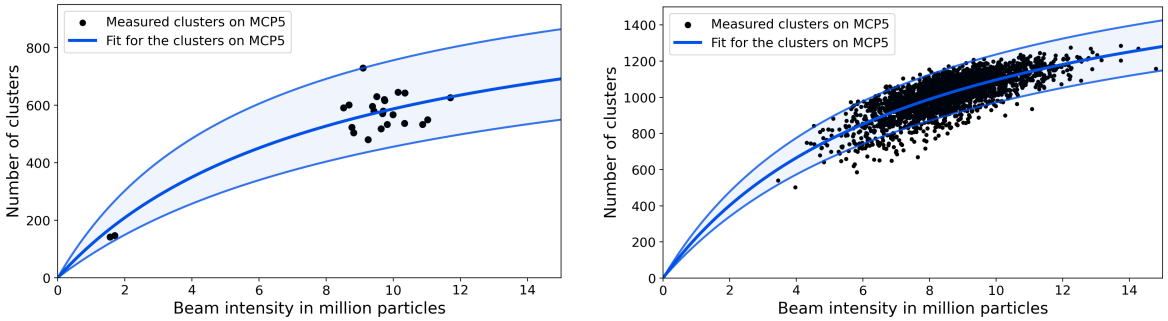

Figure 5.3: Cluster number and beam intensity for Dataset 1 (left) and Dataset 3 (right). The black points are the number of clusters found on the images on MCP5 taken during the Datasets. The blue curve is obtained by fitting Equation(5.1) to the data points. The functions that are found are $C_1(I_e) = A_1 \frac{I_e}{I_e+\mu_1}$ with $A_1 = (1.07 \pm 0.14) \times 10^3$ and $\mu_1 = 8.27 \pm 2.27$ for Dataset 1 and $C_3(I_e) = A_3 \frac{I_e}{I_e+\mu_3}$ with $A_3 = (1.93 \pm 0.12) \times 10^3$ and $\mu_3 = 7.62 \pm 1.02$ for Dataset 3. The shaded blue areas show the uncertainty of the functions obtained from the fit.

through the microwave system. Only pulses within this time window should contribute to the determination of the transition energy.

5.2.4.2 Scaling of Pulse Height Distributions at different MWS Frequencies

Even if the same number of event were measured for different MWS frequencies, their pulse height distributions have to be scaled with respect to each other. One source of a different number of pulses is the number of particles that the GBAR experiment gets from ELENA. A higher intensity of the beam should obviously also mean that more pulses are detected. Dataset 1 is scaled using the ratio of the total particle intensities for different frequencies. Specifically, the scaling factor is given by

$$\kappa^1 = \frac{I_{1060}}{I_0} \tag{5.2}$$

where I_0 and I_{1060} are the sums of the beam intensity from ELENA over all events with the MWS off and set to 1060 MHz respectively. Alternatively, instead of the beam intensities, the total number of clusters found on MCP5 can also be used for the scaling. Looking at the Datasets 2 and 3 we can see in Figure 5.4 that the average number of pulses in the four channels increases with time while the particles from ELENA (black line) stays roughly the same. It is not known what causes this, but we have to consider it in the analysis nonetheless.

For Dataset 2 the only viable solution that was found was to use the probability distributions of the pulse heights for their analysis. We should still be able to see the different numbers of Lyman alpha photons in the probability distribution since we only expect a difference for a specific frequency range, just not as clearly any more.

For Dataset 3 the runs with MWS off were taken for this exact purpose. The number of pulses in these runs should only depend on the particle intensity, so scaling the MWS off runs to each other using the same method as for Dataset 1 should allow us to scale the runs with the MWS on properly. We can also see when comparing Figure 5.4b to 5.4a that for Dataset 3 the increase in the pulse numbers over time is much lower than for Dataset 2. But we have to keep in mind that this only works if Dataset 3 is analysed alone, if the Datasets 2 and 3 get analysed together the scaling has to be done using the probability distribution again.

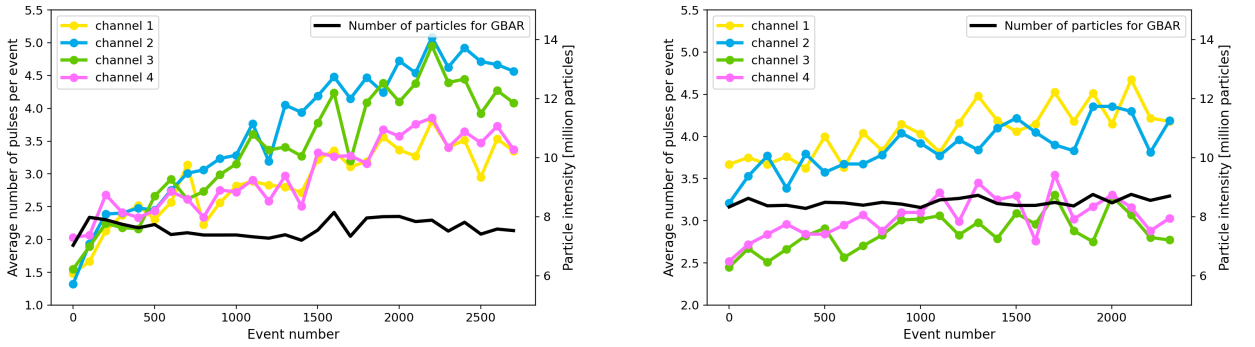

(a) Average number of pulses in the Lyman alpha MCPs for Dataset 2.

(b) Average number of pulses in the Lyman alpha MCPs for Dataset 3.

Figure 5.4: The average number of pulses in the Lyman alpha MCPs per event averaged over every 100 events for channel 1 (yellow), 2 (blue), 3 (green) and 4 (pink) for Dataset 2 (left) and Dataset 3 (right). The left y-axis corresponds to these four plots. The number of particles that GBAR received from ELENA averaged over every 100 events is displayed black, corresponding to the right y-axis.

For the analysis of Dataset 3 we consider the run with the MWS on combined with the subsequent run for which the MWS is off. For each distinct frequency f of the MWS we have n runs and the total beam intensity from ELENA of the ith run is $I_{f,i}$. The total beam intensity for all runs with frequency f is given by

$$I_f = \sum_{i=0}^{n} I_{f,i}. \tag{5.3}$$

The i-th run of frequency f has $P_{f,i,Ch}$ pulses in channel Ch. After each of the n runs at frequency f, a run with the MWS off follows, for which the number of pulses in each channel $A_{f,i,Ch}$ is determined. The subscript f stands for the MWS frequency of the previous run. We also determine the total beam intensity in million particles from ELENA over these runs with the MWS off $E_{f,i}$. We can now calculate the peak excess for the frequency f and channel Ch

$$\kappa_{f,Ch} = \sum_{i=0}^{n} \left(A_{f,i,Ch} \frac{I_{f,i}}{E_{f,i}} - P_{f,i,Ch} \right). \tag{5.4}$$

This is the difference in the number of pulses with the MWS off to the number of pulses with the MWS on and set to the frequency f. Alternatively, instead of the beam intensities, $I_{f,i}$ and $E_{f,i}$ can also be set to the total number of clusters found on MCP5 for the ith run of frequency f.

5.2.4.3 Determination of the Lamb Shift from the Voltage Pulses

For each dataset and each frequency, the number of pulses in some, yet to be determined, voltage range are counted. This voltage range is different for each channel, and they correspond to the pulse height distribution of Lyman alpha photons. This can be determined using the results of Dataset 1 and the pulse height distribution of the LEDs. Summing the number of pulses over the four channels and plotting this for each frequency should give a lineshape similar to the one in Figure 2.3, or Figure 2.5b if the different MWS influences are also considered, mirrored on the x-axis. If runs with the MWS off are also taken, the pulse numbers in the voltage ranges with different MWS frequencies can be subtracted from the pulse numbers in the voltage ranges for the MWS off to get the difference in the number of Lyman alpha photons. In this case, the resulting lineshape should look like the one in Figure 2.3, respectively Figure 2.5b. From the experimentally determined lineshapes the Lamb shift can be recovered.

5.2.5 Estimating the Number of available H in the $2S$ state in the Lyman Alpha Detector

We want to know how many events are approximately needed to get a clear signal from the Lyman alpha photons. For this, the total number of H in the $2S$ state passing through the Lyman alpha detector and the number of detected Lyman alpha photons when the MWS if off are needed.

First, the number of H on MCP5 is determined. This is done by counting the clusters as described in Section 3.2. The MCPs have an open area of around 50 percent, so the number of H on the area of MCP5 should be twice the number of clusters found. We then use the results from Section 4.4.2 to estimate the total number of hydrogen after the carbon foil. Using the values found in [28] we have that $\varepsilon_{2S} = 5.4\,\%$ of the hydrogen is in the $2S$ state after passing through the carbon foil. The opening of the Lyman alpha detector with the four MCPs inside is circular with a diameter of 4.6 cm and it is located at a distance of 84 cm from the target position. To get the total number of H in the $2S$ state passing through the Lyman alpha detector, the distribution found in Section 4.4.2 is used to calculate the percentage of all H that passes through the opening of the Lyman alpha detector and multiply this with ε_{2S}.

5.3 Lamb Shift Setup Results

The pulses in the Lyman alpha MCP voltages are found as described in Section 5.2.1 and the number of total pulses found can be seen in the Tables 5.1, 5.2 and 5.3 for Datasets 1, 2 and 3 respectively.

5.3.1 TOF Cuts of the Voltage Pulses

To get the TOF cuts we use the distance from the beginning and the end of the Lyman alpha detector to MCP5, which are $d_0 = 0.848\,\text{m}$ and $d_1 = 0.704\,\text{m}$ and the velocity of the beam $v = (1.00 \pm 0.01)\,\text{m}/\mu\text{s}$ which was calculated in Section 4.3.1. This means that the beam has a travel time of $t_0 = \frac{d_0}{v} = (0.852 \pm 0.007)\,\mu\text{s}$ from the start of the Lyman alpha detector to MCP5 and $t_1 = \frac{d_1}{v} = (0.707 \pm 0.006)\,\mu\text{s}$. To get the time window that the beam spends in the Lyman alpha detector, we need to subtract t_0 from the time that the beam starts arriving at MCP5 and subtract t_1 that the beam stops arriving at MCP5. It is important to remember that not all measurements start at the exact same time. For example, the measurement for the voltage of the Lyman alpha MCPs start 0.81 µs after the MCP5 voltage measurement for every event in Dataset 3. In Figure 5.5 we can see the pulse distribution over time for the three Datasets, once with all pulses and once only with pulses that are within the TOF window of their event. For Dataset 1 we have 93 % of all pulses within the TOF window, for Dataset 2 94 % and for Dataset 3 95 %.

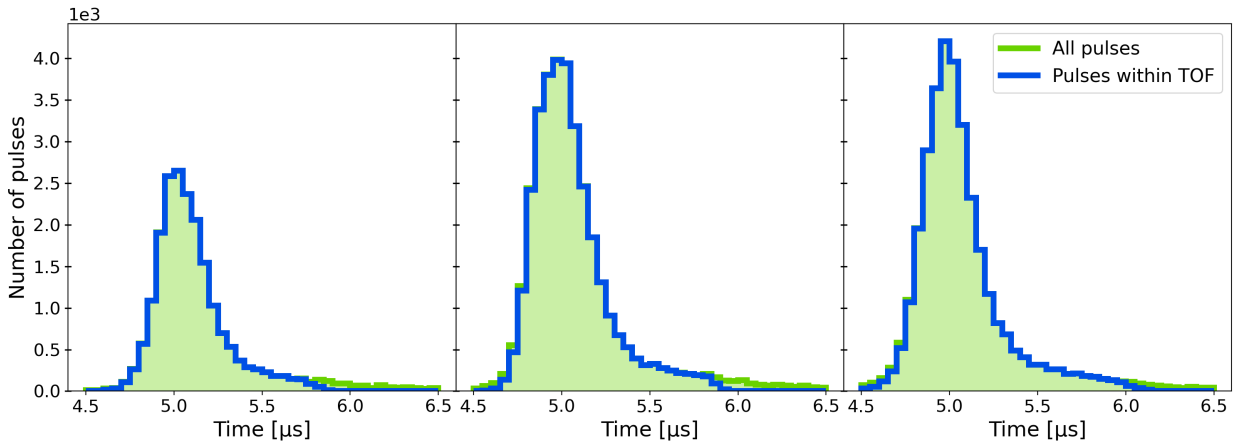

Figure 5.5: Histograms of the pulses over time. The left figure is for Dataset 1, the middle one for Dataset 2 and the right one for Dataset 3. The green histogram contains all pulses, regardless of the TOF window, and the blue histogram only contains pulses which are within the TOF window. Both histograms include the pulses between 4.5 µs and 6.5 µs which were sorted into 40 bins, each with a width of 0.05 µs.

5.3.2 Signals on the Lyman Alpha MCPs from the LEDs

The determination of the pulses is done as described in Section 5.2.2. The parameters for the different MCP biases are $h_1 = 30\,\text{mV}$ and $h_2 = 15\,\text{mV}$ for $-2.0\,\text{kV}$, $h_1 = 40\,\text{mV}$ and $h_2 = 15\,\text{mV}$ for $-2.1\,\text{kV}$ and $h_1 = 60\,\text{mV}$ and $h_2 = 20\,\text{mV}$ for $-2.2\,\text{kV}$. The parameter h_3

was set to 0.5 mV for all three biases.

The thresholds above which pulses from the noise are negligible are chosen according to Figure 2 and can be seen in Table 5.4. The number of pulses above these thresholds in the background measurements for each channel and the three MCP biases −2.0 kV, −2.1 kV and −2.2 kV can be seen in Table 5.5a. The same but for the measurements with the LEDs at a voltage of 4.75 V is in Table 5.5b. Since the number of background pulses is very small, the background can be ignored. The histograms with the pulse height distribution from the photons from the LEDs for each channel and bias mentioned before can be seen in Figure 5.6. Only pulses above the corresponding thresholds are included.

Lyman alpha MCPs bias [kV]	Channel number			
	1	2	3	4
−2.0	3 mV	2.5 mV	2 mV	3 mV
−2.1	3 mV	2.5 mV	4 mV	3 mV
−2.2	3 mV	2.5 mV	4.5 mV	3 mV

Table 5.4: Thresholds above which the pulses from the noise become negligible for the measurements of the Lyman alpha MCP voltages with the LEDs turned on.

Lyman alpha MCPs bias [kV]	Channel number			
	1	2	3	4
−2.0	1	1	1	3
−2.1	4	3	0	5
−2.2	0	7	2	12

(a) Number of pulses found in the Lyman alpha MCP voltages with the LEDs set to 0 V.

Lyman alpha MCPs bias [kV]	Channel number			
	1	2	3	4
−2.0	8129	7754	5974	14013
−2.1	8982	8678	6234	15496
−2.2	10749	9570	7342	17525

(b) Number of pulses found in the Lyman alpha MCP voltages with the LEDs set to 4.75 V.

Table 5.5: Number of pulses found in the Lyman alpha MCP voltages of each channel, with the LEDs set to 0 V on the left and 4.75 V on the right. The bias of the MCPs was set to −2.0 kV, −2.1 kV and −2.2 kV. The peaks found for the LEDs set to 0 V act as a background measurement, and ten such measurements were performed. With the LEDs on and set to 4.75 V there were twenty measurements taken. Each measurement lasts 1 ms.

5.3.3 Microwave on/off (Dataset 1) Results

For each channel, a histogram with the pulse height distribution of the pulses within the TOF window found in Dataset 1 is illustrated in Figure 5.7. The histogram for the MWS off is in green and the one for the MWS set to 1060 MHz is in blue. The histogram when combining all four channels can be seen in Figure 5.8. To get the scaling factor as mentioned in Section 5.2.4.2 we use the total beam intensity from ELENA for the MWS off events $I_0^1 = 1.0340 \times 10^{10}$ particles and the MWS on events $I_{1060}^1 = 1.0269 \times 10^{10}$ particles. The scaling factor in Equation(5.2) is now $\kappa^1 = 0.99317$. To implement the scaling, the bins of the histograms for the MWS off get multiplied with κ^1. We cannot see a clear

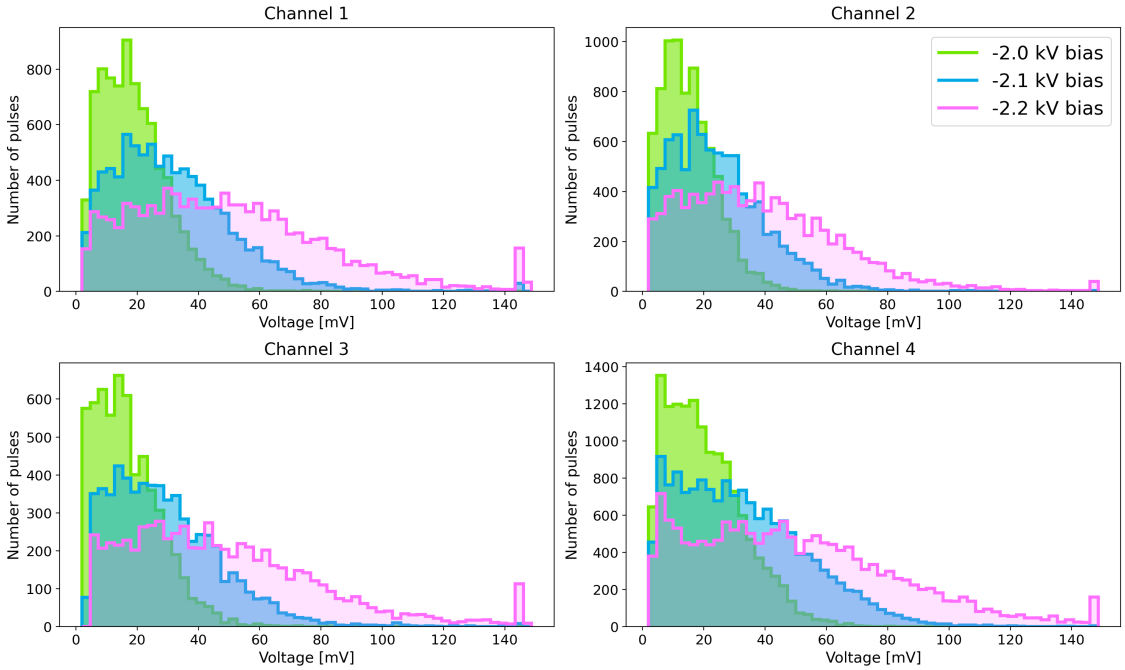

Figure 5.6: Histograms of the pulse height distribution of the voltage of the four Lyman alpha MCPs from photons at wavelength 265 nm to 280 nm emitted by the LEDs. Going from left to right and top to bottom the images are for the channel 1, 2, 3 and 4 MCPs respectively. The green, blue and pink histograms are for the MCP gains $-2.0\,\mathrm{kV}$, $-2.1\,\mathrm{kV}$ and $-2.2\,\mathrm{kV}$. Each histogram includes pulses which are higher than their corresponding thresholds seen in Table 5.4 sorted into 54 bins each with a width of $2.67\,\mathrm{mV}$.

contribution from noise pulses, like for the LEDs. This is because there is a more strict selection process being used for small pulses.

We can clearly see an excess of pulses for the MWS off histogram compared to the MWS on one. The difference in the number of pulses up to different voltages has been plotted in steps of 1 mV for each channel and can be seen in Figure 5.9. We can clearly see the difference increasing in the start and then staying roughly constant. The voltages at which the pulse difference stops increasing V_{t-Ch} for channels 1, 2, 3 and 4 are $V_{t-1} = 83\,\mathrm{mV}$, $V_{t-2} = 71\,\mathrm{mV}$, $V_{t-3} = 133\,\mathrm{mV}$ and $V_{t-4} = 106\,\mathrm{mV}$. The number of signals from Lyman alpha photons for each channel is given by the difference between the number of pulses below V_{t-Ch} for the MWS off events to the number of pulses below V_{t-Ch} for the MWS on events. This gives us (110 ± 40) signals in channel 1, (156 ± 48) signals in channel 2, (153 ± 54) signals in channel 3 and (92 ± 41) signals in channel 4. The errors of these values are calculated as described in Section 3.1. For example, in channel 1 we have 855 pulses in the MWS off events and 739 pulses in the MWS on events without any scaling. This gives us the uncertainty for the number of Lyman alpha signals in channel 1 $\sqrt{855 + 739} = 40$.

If the number of all pulses below V_{t-Ch} are summed over the four channels, we get $\mu_0 = (4515 \pm 67)$ pulses in the MWS off events and $\mu_1 = (3973 \pm 63)$ pulses in the MWS

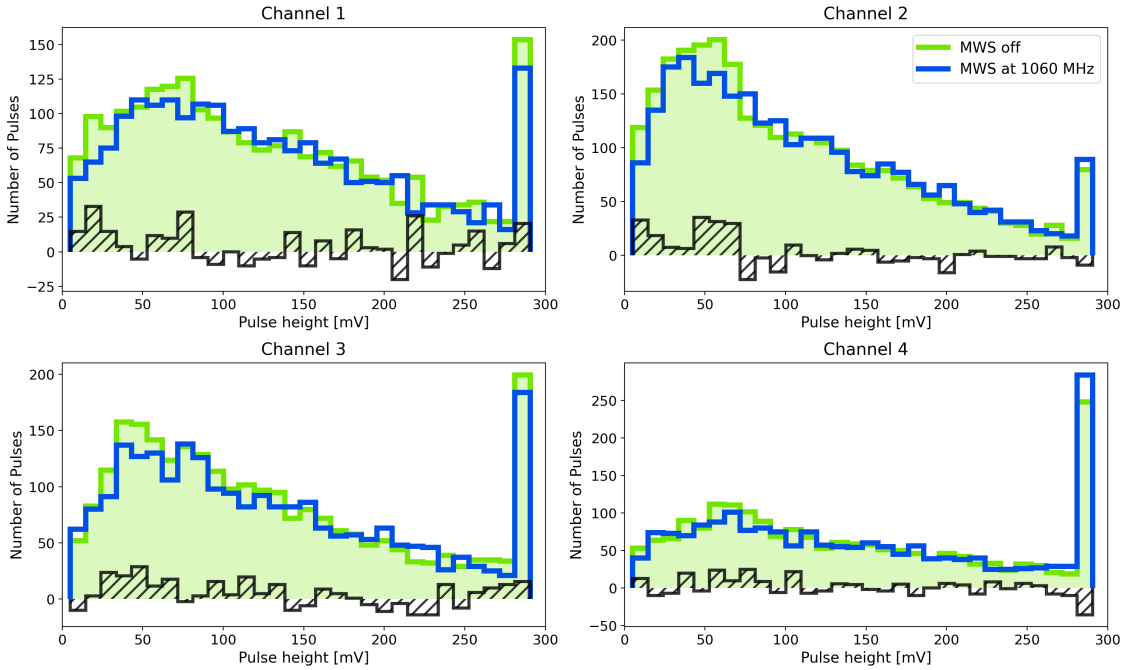

Figure 5.7: Histograms of the pulse heights found in Dataset 1 for each channel. Only pulses within the TOF window were included. The distribution of pulses found in the MWS off events is depicted in green and the one for the MWS set to 1060 MHz in blue. The MWS off histograms were scaled to the MWS on histograms by comparing the total beam intensities between the MWS off and on events. The dashed black areas show the difference between the number of pulses between the two histograms.

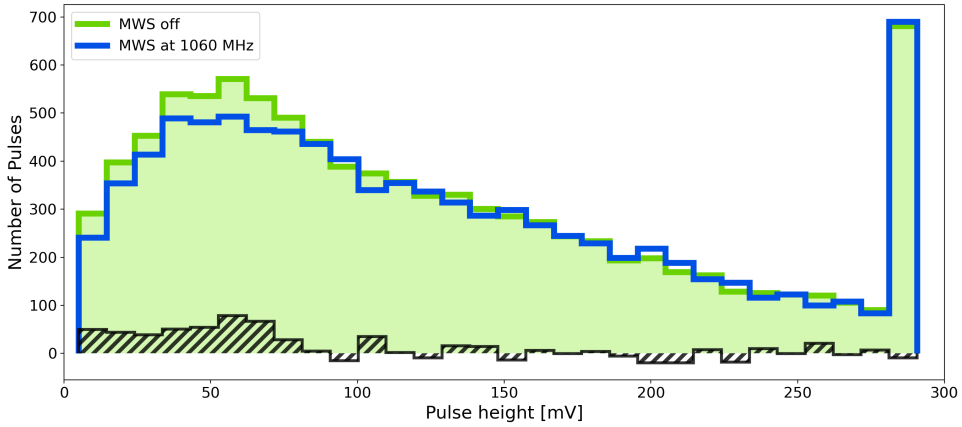

Figure 5.8: Histogram of the pulse heights found in Dataset 1 in all four channels. Only pulses within the TOF window were included. The distribution of pulses found in the MWS off events is depicted in green and the one for the MWS set to 1060 MHz in blue. The MWS off histogram was scaled to the MWS on histogram by comparing the total beam intensities between the MWS off and on runs. The dashed black area shows the difference between the number of pulses between the two histograms.

on events. Thus, the resulting uncertainty is $\sigma_a = \sqrt{4515 + 3973} = 92$. When scaling these numbers with the total beam intensity, we get the total number of detected Lyman alpha signals of 511 ± 92. This means that we have a signal of $\frac{511}{92} = 5.6$ sigma.

The calculations described in Section 5.2.5 can be used to get the number of hydrogen in the $2S$ state passing through the Lyman alpha detector. As described in Section 4.4.2 a distribution similar to the one found in Section 4.3.2.2 is used but with an increased uncertainty such that $\varrho^A = (19.0 \pm 4.0)\,\%$.

The number of clusters on MCP5 for each event is calculated with the function $C(I_e, A_1, \mu_1)$ from (5.1) with I_e the beam intensity in million particles and A_1 and μ_1 are the values found in Section 5.2.3. For all MWS on events of Dataset 1 this gives us a total of $C^1_{MCP} = (6.19 \pm 0.03) \times 10^5$ clusters on MCP5. Since we only see a cluster on MCP5 for 50 % of the hydrogen on the area of MCP5 the total number of hydrogen on the area of MCP5 is $N^1_{MCP5} = (1.20 \pm 0.15) \times 10^6$. This is $(19.0 \pm 4.0)\,\%$ of the total hydrogen, and thus in total we have $N^1_{tot} = (6.52 \pm 1.37) \times 10^6$ hydrogen atoms after the carbon foil for all MWS on events. Of these, hydrogen atoms 5.4 % are in the $2S$ state which gives us $N^1_{tot,2S} = 0.054 \times N^1_{tot} = (3.52 \pm 0.74) \times 10^5$ hydrogen in the $2S$ state in all MWS on events. To calculate the number of H atoms passing through the Lyman alpha detector, we need to determine the percentage of the distribution mentioned before that is within 2.3 cm of its centre at a distance of 84 cm from the carbon foil. We get that $\varepsilon_{dist} = (41.5 \pm 11.0)\,\%$ of all hydrogen atoms pass through the Lyman alpha detector. This means that in total $N^1_{LyA} = N^1_{tot,2S} \times \varepsilon_{dist} = (1.46 \pm 0.49) \times 10^5$ hydrogen atoms in the $2S$ state pass through the Lyman alpha detector for all MWS on events of Dataset 1.

Repeating these calculations for the MWS off events of Dataset 1 we have the total number of clusters on MCP5 $C^0_{MCP5} = (6.23 \pm 0.03) \times 10^5$ and the total number of hydrogen atoms after the carbon foil $N^0_{tot} = (6.56 \pm 1.38) \times 10^6$. The total number of hydrogen in the $2S$ state is $N^0_{tot,2S} = (3.54 \pm 0.75) \times 10^5$ and the total number of hydrogen atoms in the $2S$ state passing through the Lyman alpha detector is $N^0_{LyA} = (1.47 \pm 0.50) \times 10^5$.

As mentioned in Section 5.2.4.2 instead of the beam intensity the number of clusters on MCP5 can be used for the scaling in Equation(5.2). For this the estimated number of clusters from Section 5.2.3 are used as there are only images of MCP5 for 24 out of 2339 events available. The estimated number of clusters on MCP5 for all MWS off events is $C^0 = (6.23 \pm 0.03) \times 10^5$ and for all MWS on events $C^1 = (6.19 \pm 0.03) \times 10^5$. This means that there were $\gamma^{0,1}_{LyA} = \mu_0 \frac{C^1}{C^0} - \mu_1 = 518 \pm 98$ more Lyman alpha photons detected in the MWS off events than the MWS on events. To get the number of Lyman alpha photons for the MWS off and on events separately we use the MWS efficiency for 1060 MHz which is 0.86 taking the value from Table 2.1. This means that there should be $\gamma^0_{LyA} = \gamma^{0,1}_{LyA} \frac{0.14}{0.86} = 84 \pm 16$ Lyman alpha photons detected in all MWS on events. The number of detected Lyman alpha photons for the MWS off scaled to C^1 is thus $\gamma^1_{LyA} = 602 \pm 114$. For the MWS on events, there were a total of $N^1_{LyA} = (1.46 \pm 0.49) \times 10^5$ hydrogen in the $2S$ state going through the Lyman alpha detector. The quenching efficiency has been found with a simulation using SIMION to be around $\varepsilon_{quench} = 0.8$ so there

should be a total of $\gamma^0_{quench} = \varepsilon_{quench} \times N^0_{LyA} = 1.17 \pm 0.40$ Lyman alpha photons emitted in the Lyman alpha detector. The area covered by the MCPs on the sides gives a geometric efficiency of around $\varepsilon_{geo} = 0.5$, meaning that $\gamma_{quench,geo} = (5.85 \pm 1.98) \times 10^4$ Lyman alpha photons should hit an MCP. Of these we detect $\gamma^1_{LyA} = 602 \pm 114$, giving us the efficiency to detect a Lyman alpha photon hitting the MCP $\varepsilon^m_{LyA} = \frac{\gamma^1_{LyA}}{\gamma_{quench,geo}} = (1.03 \pm 0.40) \times 10^{-2}$ and the total efficiency $\varepsilon^m_{tot} = \varepsilon_{quench} \times \varepsilon_{geo} \times \varepsilon^m_{LyA} = (4.12 \pm 1.60) \times 10^{-3}$. We would expect that this efficiency is the combination of the quantum efficiency ε_{QE} and the efficiency of the MCP ε_{MCP}, giving us $\varepsilon^e_{LyA} = \varepsilon_{QE} \times \varepsilon_{MCP}$. The quantum efficiency for CsI coated MCPs was found to be around $\varepsilon_{QE} = 0.5$ in [39]. The efficiency of the MCPs was measured in [28] to be around $\varepsilon_{MCP} = 0.8$ so $\varepsilon^e_{LyA} = 0.4$. This results in a total efficiency of $\varepsilon^e_{tot} = \varepsilon_{quench} \times \varepsilon_{geo} \times \varepsilon^e_{LyA} = 0.16$. This efficiency was also experimentally verified some years ago for the same setup at PSI with Muonium [35, 27].

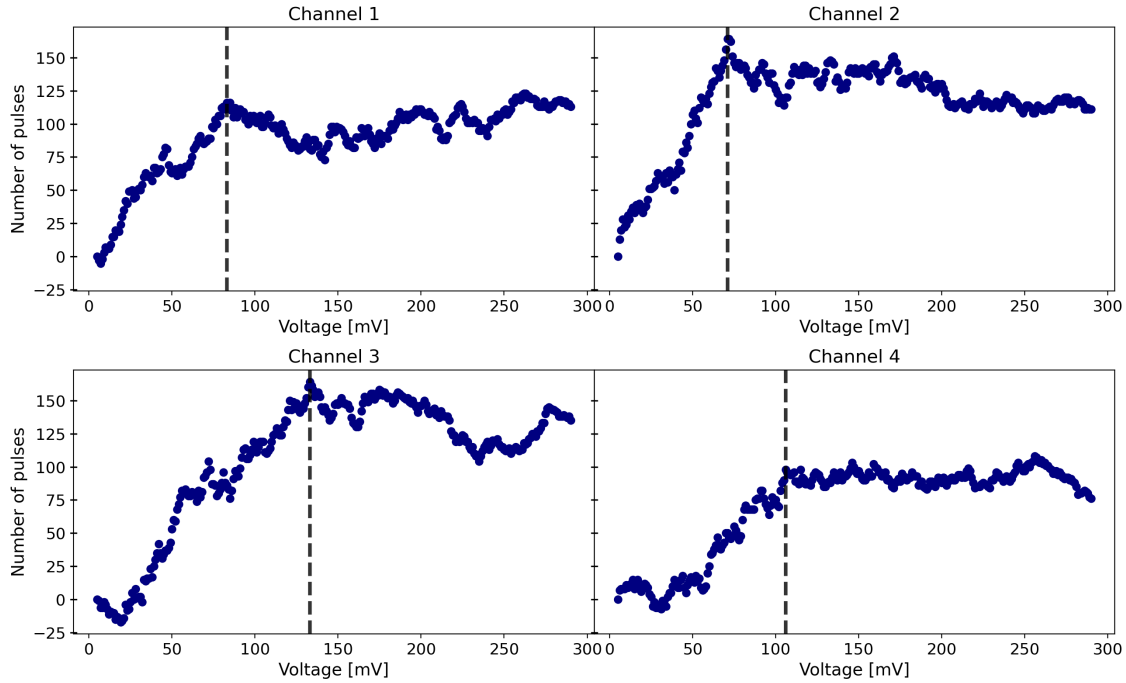

Figure 5.9: Difference in the number of pulses in the MWS off and on events from Dataset 1 from 5 mV up to the voltage given on the x-axis. In each channel there is a clear increase visible up to a certain point marked by a dashed line, after which the difference in pulses stabilises.

5.3.4 Microwave Scan 1 (Dataset 2) Results

For each different frequency, the pulses were determined and the number of pulses below the voltages mentioned in Section 5.3.3 were counted and divided by the total number of pulses for each channel and frequency. This essentially gives us the percentage of pulses within the area where we expect to see the pulses from the Lyman alpha photons. These percentages are plotted in Figure 5.10.

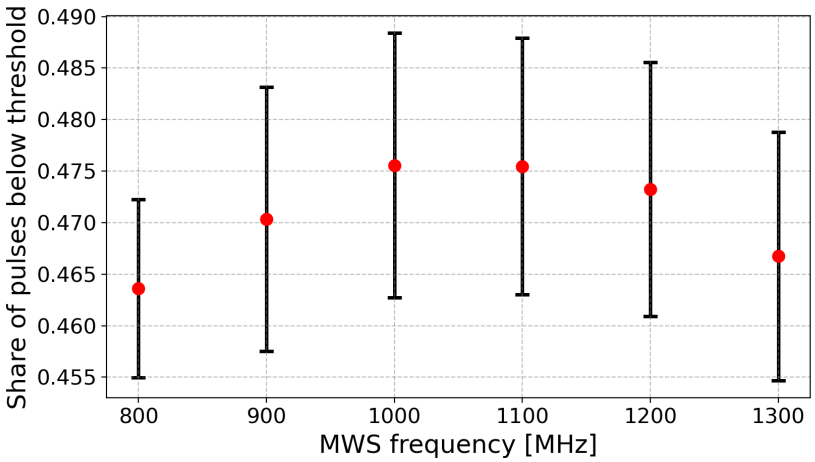

Figure 5.10: Share of pulses from Dataset 2 below the voltage thresholds found in Section 5.3.3 in comparison to the total number of pulses summed over all four channels. The MWS was set to the six different frequencies 800 MHz, 900 MHz, 1000 MHz, 1100 MHz, 1200 MHz and 1300 MHz.

5.3.5 Microwave Scan 2 (Dataset 3) Results

The pulses found for Dataset 3 were evaluated with Equation(5.4). The resulting lineshape can be seen in Figure 5.11a. As mentioned in Section 5.2.4.2, the number of clusters can be used for the scaling instead of the beam intensities. Since images of MCP5 are available for all except three events, the cluster number of these three events is calculated as described in Section 5.1 and for all other events the actual number of clusters that was found was used. In Table 5.7 the number of pulses for different MWS frequencies can be seen. The values for each row with the MWS frequency 0 MHz correspond to the MWS off runs taken right after the MWS on runs with the frequency from the previous row. The results of Equation(5.4) using the cluster numbers can be seen in Table 5.6. These results are also illustrated in Figure 5.11b.

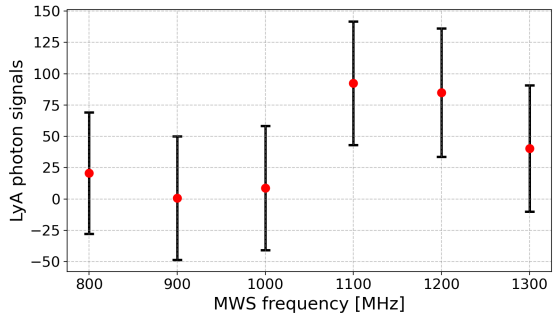

(a) Lineshape for Dataset 3 with the beam intensity used for the scaling in Equation (5.4).

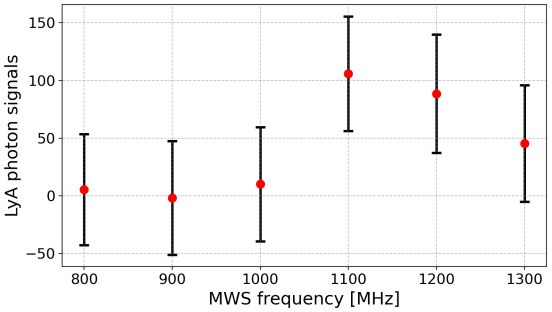

(b) Lineshape for Dataset 3 with the cluster numbers used for the scaling in Equation (5.4).

Figure 5.11: Excess number of pulses from Dataset 3 between MWS off and on runs. For the figure on the left, the beam intensity was used for the scaling and for the figure on the right, the cluster numbers were used. The MWS was set to the frequencies 800 MHz, 900 MHz, 1000 MHz, 1100 MHz, 1200 MHz and 1300 MHz. Only pulses below the voltages V_{t-Ch} are considered for each channel. For the final result, the number of excess pulses is summed over all four channels.

f_{MWS} [MHz]	800	900	1000	1100	1200	1300
N^1_{LyA}	-4 ± 32	-21 ± 34	-57 ± 34	59 ± 34	94 ± 35	15 ± 36
N^2_{LyA}	9 ± 36	20 ± 36	67 ± 36	46 ± 36	-5 ± 37	30 ± 35
N_{LyA}	5 ± 48	-1 ± 49	10 ± 50	105 ± 50	89 ± 51	45 ± 50

Table 5.6: Number of excess pulses under V_{t-Ch} found in the events of Dataset 3 when comparing MWS off to MWS on events. f_{MWS} is the MWS frequency in MHz. As described in Section 5.1.3 for each frequency there were two runs with 100 events each taken. N^1_{LyA} are the excess pulses taking only the first run of each frequency, and N^2_{LyA} are the excess pulses for the second run. N_{LyA} is the total excess over both runs. To compare the MWS on to off runs, the number of pulses in the MWS off runs was scaled using the number of clusters on MCP5 for the runs. A plot for N_{LyA} at different frequencies is illustrated in Figure 5.11b.

f_{MWS} [MHz]	N_{LyA} $[1 \times 10^4]$	P_{thresh}	f [MHz]	N_{LyA} $[1 \times 10^4]$	P_{thresh}
800	4.54 ± 1.53	1171 ± 34	1100	4.84 ± 1.64	1185 ± 34
0	4.68 ± 1.58	1212 ± 35	0	4.91 ± 1.67	1308 ± 36
900	4.68 ± 1.58	1219 ± 35	1200	4.87 ± 1.64	1278 ± 36
0	4.72 ± 1.59	1228 ± 35	0	4.92 ± 1.66	1381 ± 37
1000	4.75 ± 1.60	1235 ± 35	1300	4.84 ± 1.64	1265 ± 36
0	4.83 ± 1.63	1266 ± 36	0	4.94 ± 1.67	1337 ± 37

Table 5.7: Table with results for Dataset 3 from Section 5.3.5. f stands for the frequency of the MWS, N_{LyA} stands for the total number of hydrogen atoms in the $2S$ state passing through the Lyman alpha detector for each frequency and P_{thresh} is the sum of the number of pulses below V_{t-Ch} for each channel. The rows with MWS frequency f bigger than zero contain the information of all the events from runs where the MWS was set to the frequency f_{MWS}. As described in Section 5.1.3 after each run with the MWS on a run with the MWS off was taken. The rows with $f = 0\,\text{MHz}$ contain the information of the runs with the MWS off taken right after the runs with the MWS on and set to the frequency from the previous row.

5.4 Discussion of the Lamb Shift Setup Tests

5.4.1 Problems and Possible Improvements for the Pulse Finding Algorithm

It is very important for the pulse finding to work properly, but this is quite challenging. The main problem is the ringing in the voltage after particle impacts, mentioned in Section 5.2.1.1. This does get compensated with ς_{Ch} but the shape of this ringing is not always exactly the same, though it is always very similar. This is particularly problematic for pulses below 20 mV, which can still be affected by some remaining noise. For this purpose the fit with $\varsigma_{pulse,Ch}$ is performed but the lower a pulse is the more lenient the fit becomes and for pulses below 15 mV it gets quite difficult to determine if something is a pulse from a particle or photon impact on the MCP or noise. In this analysis, pulses above 5 mV are considered, but it may make more sense to set the minimum height of a pulse to a higher value around 15 mV for the reasons mentioned before. However, the results in Sections 5.3.3, 5.3.4 and 5.3.5 barely change when the minimum height of the pulses is increased.

The fitting of the pulses explained in Section 5.2.1.2 is not too important for the data from a H^- beam because there are not that many signals. In general, fitting even more pulse shapes would be better if there are more signals, but this was not done for this analysis because of runtime lengths. One improvement that could be made to these fits of multiple pulses is to consider the noise after the pulse. In Figure 5.2 the blue and green curves are the specific functions of which two are fit to the measurements. These functions are defined as the area of ς_{Ch} around the peak of a pulse until the voltage crosses 0 V on either side. This means that the noise caused by the first pulse is not considered in the fit, which would have an influence on the second pulse. It is also possible that, with the current implementation of this fit method, a single pulse is sometimes saved as two pulses. There are selection processes to try and inhibit this, and this most like happens only rarely.

The ultimate goal of the whole setup is of course to measure the Lamb shift of antihydrogen. There were no background measurements of the Lyman alpha MCPs made until now with a $\overline{p}$ beam because of insufficient beam steering. With a $\overline{p}$ beam, there would be a lot of pions created in the beam line due to annihilation of the $\overline{p}$. Most of these pions would arrive sooner at the Lyman alpha detector than the $\overline{p}$ and any $\overline{H}$ produced due to its much lower mass and thus much faster velocity, but there would still be a large background visible from them. Very precise beam steering is required to bring this pion background to a level where the pulses in the MCP voltages can be properly determined. This increase in the background makes the methods described before even more important. It should be possible to decrease the noise from impacts on the MCPs substantially with changes to the electrical circuits of the MCPs. Reducing this as much as possible would be quite important for the determination of the Lamb shift of $\overline{H}$. The fitting of multiple pulses would also be more important to recover any signals from Lyman alpha photons with a large pion background. As mentioned before, ideally, more than two pulse shapes would be fit to the voltages together.

5.4.2 Signals from the LEDs on the Lyman Alpha MCPs

We can see quite well that the signals from the LEDs are at the lower voltages and go towards higher voltages for higher biases of the MCPs. For each MCP bias the LED power was the same so there are the same number of photons passing through the Lyman alpha detector for each bias, however the total number of pulses that were detected increases for each higher bias. At some point, the whole distribution of the pulses from the photons should be visible, and increasing the gain would not result in an increase of detected pulses. We do not see the whole distribution of the pulses for the highest bias of $-2.2\,\mathrm{kV}$ so it might be ideal to have an even higher bias but increasing the bias even more could damage the MCPs. A higher bias also means that we do not have as clear of a signal region for the photons, as their pulse height distribution stretches more. Because of this, it might make sense to try and decrease the bias for further microwave

scan measurements. This would ultimately result in less detected pulses from Lyman alpha photons, but the signals from them in the pulse height distribution should be much clearer, allowing us to analyse a smaller voltage range. There were also some measurements with the MWS off and on at frequency 1060 MHz made for the MCP biases -2.0 kV and -2.1 kV, but the data from -2.2 kV seemed to be the clearest at the time, which is the reason that the microwave scans were also performed with an MCP bias of -2.2 kV

The photons from the LEDs have a wavelength of 265 nm to 280 nm and thus an energy of 4.4 eV to 4.7 eV while the Lyman alpha photons have a wavelength of around 122 nm and an energy of around 10 eV. The higher energy of the Lyman alpha photons means that their pulse heights should be at higher voltages than for the photons from the LEDs. However, the energy difference is so small that the pulse height distribution from the Lyman alpha photons should be very similar to the one from the LED photons.

5.4.3 MWS Line Shape and Power Spectrum

Looking at Figure 2.5a a similar shape to Figure 2.3 is visible. While the γ transition blends together with the α and β transitions more, it is still visible to be separated from them. If the power spectrum of the MWS is also considered in Figure 2.5b all three transitions blend together and cannot be seen separately any more at all. The probability does visibly fall off slower towards lower frequencies. To get a precise measurement of the Lamb shift, this power spectrum has to be compensated. This can be done by using different input powers depending on the frequency for the signal generator. This has not been done for the measurements in this analysis, so when performing a microwave scan the numbers of detected Lyman alpha photons with the MWS at different frequencies are expected to have a similar shape with respect to each other as the probabilities in Figure 2.5b mirrored on the x-axis.

5.4.4 Dataset 1 Results Discussion

For Dataset 1 we can clearly see the Lyman alpha photons in the pulse height distribution in Figure 5.8. Looking at each channel separately in Figure 5.7 the Lyman alpha photons are not quite as clearly visible. The best indication from the Lyman alpha photons comes from Figure 5.9. The number of pulses in the MWS off events minus the number of pulses in the MWS on events nicely increases until a point, after which it stays roughly constant. These points should be where the pulse height distribution for the MCP bias -2.2 kV in Figure 5.2.2 becomes small. Specifically, these voltages found in Dataset 1 are 83 mV, 71 mV, 133 mV and 106 mV for the channels 1, 2, 3 and 4. Looking at Figure 5.2.2, this seems to add up more or less, though we would expect a higher threshold for channel 1, whereas channel 3 should have a lower threshold. But all in all, they agree

nicely.

For the estimation of the total number of hydrogen in the $2S$ state passing through the Lyman alpha detector, the number of clusters on MCP5 was utilized. Since we do not have images of MCP5 for most of the events of Dataset 1 the fit of the function (5.1) to the available pictures was used to estimate the number of clusters on MCP5. As discussed in Section 3.2 the number that was used was definitely smaller than the actual number of particles that triggered an electron shower on MCP5 due to the overlapping cluster. This could explain the shape of the curve seen in Figure 5.3. If the beam intensity is higher there is more neutral hydrogen produced at the carbon foil and thus there are more particle impacts on MCP5 and a higher number of clusters should be visible on MCP5. But the more clusters there are, the higher the likelihood is that a new cluster will overlap with an existing cluster. Since the images from Dataset 3 were used to find the form of the fit function in (5.1) which have more clusters on MCP5 for the same beam intensity than Dataset 1 this effect could skew the estimations for Dataset 1. Additionally, the function from Equation(5.1) might not be of the ideal form. This means that the number of hydrogen in the $2S$ state is actually higher than the numbers calculated in Sections 5.3.3 and 5.3.5.

The ratio between the predicted and measured efficiency is $\frac{\varepsilon^e_{tot}}{\varepsilon^m_{tot}} = 39 \pm 15$. This means that we would expect to see nearly 40 times more Lyman alpha photons. One reason for this difference is that we cannot find every pulse in the voltage of the MCPs. The efficiency of determining the pulses correctly could be around $\varepsilon_{pulses} = 0.8$, which would still leave us with over 30 times more predicted Lyman alpha signals than detected. Another reason is that as we saw in Section 5.4.2 is that we do not see the whole distribution of the pulse heights for the LED photons. This should be similar for the Lyman alpha photons, so some Lyman alpha signals are lost because they are below the minimum pulse height threshold set to 5 mV. Most of the difference in the expected and measured efficiency is due to ageing and improper handling of the MCPS which is talked about more in Section 5.4.7.

5.4.5 Dataset 2 Results Discussion

Looking at Figure 5.10 we do not see what we would expect. If the MWS frequency is closer to the transition frequency, more $2S_{1/2} \rightarrow 2P_{1/2}$ transitions should take place in the MWS, followed by the near immediate decay of the hydrogen in the $2P_{1/2}$ state to the ground state and emission of a Lyman alpha photon. This means that when the MWS frequency is closer to the transition frequency, there will be less hydrogen in the $2S$ state in the quenching field of the Lyman alpha detector, which means that less Lyman alpha photons get emitted in the detector. Consequently, we would expect the percentage of pulses below V_{t-Ch} to be smaller closer to the resonance frequency, so

similar to the negative of the black curve seen in Figure 2.5b. However, what we see is the exact opposite, with the percentage of pulses below V_{t-Ch} being the lowest for 800 MHz and 1300 MHz. But there are some problems if we just look at the percentages. This is only done because of the large increase in pulses during the measurements of Dataset 2 as seen in Figure 5.4a which means that we cannot use the beam intensity which stayed more or less constant to scale different MWS frequencies to each other. As mentioned in Section 5.4.4 this is very likely due to the beam trajectory or emittance changing. This could be caused by some part of the experiment slowly accumulating a charge. However, the electron cooler in the ELENA ring was broken for these measurements, which could also be the reason for the beam parameters changing. This seems quite likely, as such an extreme increase in the pulse numbers was otherwise never detected. For Dataset 3 we can also observe a slight increase in the pulse numbers as seen in Figure 5.4b but much less than for Dataset 2.

All of this makes it quite difficult to get any conclusions from Dataset 2. There were also no events with the MWS off taken which could be used as a reference. There were also no images of MCP5 saved for the whole Dataset. We can have a look at the scatter plot of the pulse heights and the timings of the pulses in Figure 3. We can see that the beam always arrives at similar times from the large number of points from $-0.5\,\mu s$ to $0.5\,\mu s$. There is also a tail of pulses at later times. These come most likely from particles that lost a lot of energy in the carbon foil and are thus slower. We can also see that there are a lot of pulses with height around 291 mV. This is the maximum voltage that we can measure from the MCP, so all pulses that would be above 291 mV are just at this voltage. Other than that, we cannot see anything out of the ordinary. We can also look at the histogram of the pulse numbers at different heights and event numbers from Dataset 2 in Figure 4. There is a clear increase in the number of pulses at all heights visible for later events. We can also see that the uppermost row contains more pulses than the ones immediately below, which comes again from the pulses higher than the voltage cap around 291 mV. The first row also contains very few pulses. As stated in Section 5.1.2 there were no particles reaching the reaction chamber because of a mechanical problem from around event 30 to event 100.

Looking only at the percentages for the pulses is a flawed way to search for the Lyman alpha signals, but there was no method found to properly process this data. If we calculate the percentages for Dataset 1 the same as was done for Dataset 2 we get that $(47.60 \pm 0.09)\,\%$ of all pulses are below the thresholds V_{t-Ch} for the MWS off events and $(43.90 \pm 0.08)\,\%$ for the MWS on events. This means that we have an excess of $(3.6 \pm 1.2)\,\%$ for the events with the MWS off and a statistical significance of $\frac{3.6}{1.2} = 3\,\text{œ}$. We have a bit less than half the pulses for each frequency used in Dataset 2 than we do in Dataset 1. This means that we have less statistical significance for the results of Dataset 2, so more statistics would be required for a definitive result.

5.4.6 Dataset 3 Results Discussion

For Dataset 3 there were both MWS off runs taken after each MWS on run and the MCP5 images were saved. This means that we can now nicely calculate the excess of Lyman alpha photons for each MWS frequency compared to the MWS off runs, which are shown in Figure 5.11. Again, this does not look as we would expect. For 900 MHz and 1000 MHz, we would expect there to be a bigger excess than both 800 MHz and 1300 MHz. However, similarly to Dataset 2 there were only few events taken, only 200 per frequency which leads to a low statistical significance. As described in Section 5.1.3 for each frequency two runs of 100 events were taken. The excess of pulses below V_{t-Ch} for each of these two runs separately for each frequency, and using the cluster numbers for the scaling, are written in Table 5.6. We can see that there can be a huge difference in the pulse excess for the two runs, so our main conclusion is the same as for Dataset 2 in that we need more statistics.

The results obtained using the beam intensities and the cluster numbers for the scaling can be compared. The two lineshapes using the different scaling methods in Figure 5.11 both look similar. The exact results differ by a bit, but not significantly so the beam intensity might be sufficient to use for the scaling, provided that there are no large fluctuations in the number of pulses over time as for Dataset 2.

5.4.7 Methods to Improve the Detection Efficiency of Lyman Alpha Photons

Some methods that could improve the detection efficiency, such as reducing the ringing from pulses in the MCP voltages, have already been mentioned. A change to the setup that could nearly double the detected Lyman alpha photons would be to change the polarization of the front side MCP bias. For all three Datasets in this analysis, a negative voltage was applied to the front side of the MCPs. This is usually done in order to reduce the background from electrons, but in the setup of the GBAR experiment there should be no substantial background from electrons. The advantage of having a positive voltage applied to the front side of the MCPs is that electrons produced by photons hitting the space between channels in the MCP would get pulled back into a channel and thus triggering an electron shower. As stated before, around 50 % of the MCP surface is covered by channels, so ideally this would lead to two times as many Lyman alpha signals.

It could also be beneficial to test the quenching field. For the three Datasets in this analysis, the downstream electrode was set to 3 kV and the upstream electrode to 0 kV. These values were determined to give an efficiency of around 0.8 to induce the $2S_{1/2} \rightarrow 2P_{1/2}$ transition by a simulation, but this was never tested. If the quenching efficiency could be increased, this would lead to an increase in Lyman alpha signals by the same percentage.

A reason that the detection efficiency of Lyman alpha photons is lower than expected

could be that the CsI coating of the MCPs is damaged. CsI is hygroscopic, and thus any exposure to air will lower the efficiency of the MCPs. This was investigated in [43]. The MCPs have spent some time in a depreciated vacuum due to vacuum pumps malfunctioning, which has decreased their quantum efficiency. The MCPs also just lose some efficiency over time as they age. Prolonged exposure to photons can also damage the coating, but the photon flux at the GBAR experiment is not very high, there is most likely only a minimal effect of this. Heavier particles such as protons can also damage the coating. It is unclear exactly how much the efficiency was affected by this. In the future, the LEDs mounted in front of the Lyman alpha detector can be used as a benchmark to test for any change in the quantum efficiency of the Lyman alpha MCPs. In the end, the only options to improve the damaged CsI coating would be to recoat the MCPs.

Chapter 6

$\overline{\mathrm{H}}$ Production Rate in 2024 at GBAR

6.1 Data for the $\overline{\mathrm{H}}$ Production Analysis

To determine the production rate of $\overline{\mathrm{H}}$ runs with and without positrons, which are effectively background runs, are compared to each other. There were a total of six mixing runs and four background runs taken for a total of 560 mixing and 776 background events. The mixing runs contain events with a $\overline{\mathrm{p}}$ beam where positrons are added to the beam in the reaction chamber so the reactions (2.4) and (2.5) can occur. For the background runs, we also have a $\overline{\mathrm{p}}$ beam, however there are no positrons added to the beam in the reaction chamber. For both the mixing and background runs, the MCP5 bias was set to 2.2 kV. Some information for runs can be seen in Table 6.1.

Run number	0	1	2	3	4	5	6	7	8	9
Run mode	mix	mix	mix	mix	mix	mix	bkg	bkg	bkg	bkg
Number of events	218	53	171	79	4	35	304	20	34	418
Number of events with $n_I < 6$ [millions]	2	0	0	0	0	1	2	0	0	3
Number of event with no positrons	51	10	11	11	2	4	-	-	-	-
Number of valid events	165	43	160	68	2	30	302	20	34	415
Average number of particles from ELENA per valid event	10.69	10.78	10.70	10.75	10.78	10.6	10.75	10.49	10.67	10.72

Table 6.1: Information of the mixing runs (mix) and for the background runs (bkg). In row 4 n_I stand for the number of particles that GBAR receives from ELENA in millions and in rows 6 and 7 the valid events consist of events with $n_I > 6$ and positrons.

There were also eleven events recorded in the runs 610 and 618 with the same beam steering ant $\overline{\mathrm{p}}$ trap setup as the background runs in Table 6.1 but with the switchyard turned off so that the $\overline{\mathrm{p}}$ beam can be seen on MCP5. The MCP5 bias was also only set to 1.45 kV.

6.2 $\overline{\mathrm{H}}$ Production Rate Analysis Methods

Any $\overline{\mathrm{H}}$ that are produced in the reaction chamber have nearly the same speed as the $\overline{\mathrm{p}}$, and thus travel with the $\overline{\mathrm{H}}$ beam. The $\overline{\mathrm{p}}$ are deflected by the switchyard before reaching MCP5 as opposed to the $\overline{\mathrm{H}}$. Thus, the eleven events with the $\overline{\mathrm{p}}$ beam on MCP5 can be used to get the time window in which the $\overline{\mathrm{H}}$ signals can be found. The voltage of MCP5 averaged over all eleven events can be seen in Figure 6.2. The beam window is marked by the dashed red lines and goes from 6.46 µs to 6.86 µs.

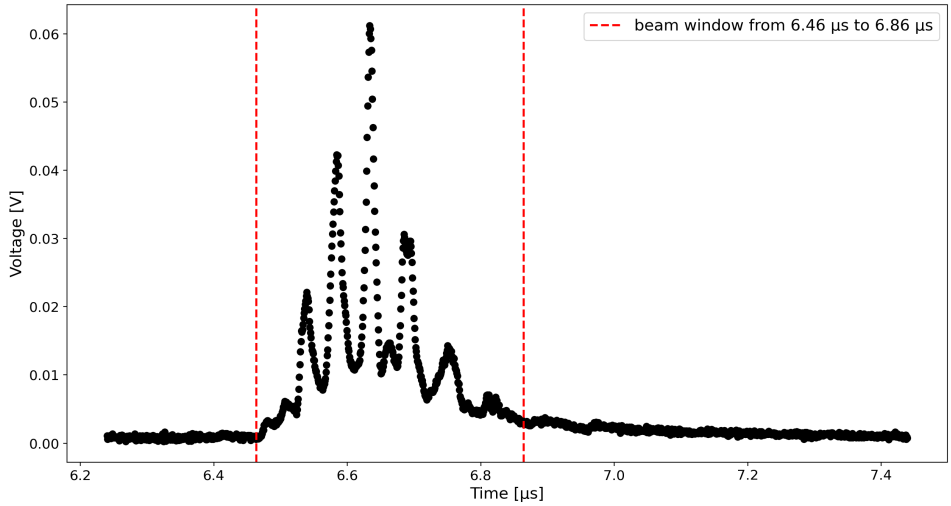

Figure 6.1: Averaged voltage of MCP5 for the eleven events in runs 610 and 618. For these events the setup was the same as for the background runs in Table 6.1 except that the switchyard was turned off. As a result, the $\overline{\mathrm{p}}$ beam can be seen on MCP5. The specific shape of the $\overline{\mathrm{p}}$ beam waveform depends on the Trap setup. Any $\overline{\mathrm{H}}$ produced in the mixing runs arrives with the same timing as the $\overline{\mathrm{p}}$ beam. The window highlighted in the image in which the majority of the $\overline{\mathrm{p}}$ arrive goes from 6.46 µs to 6.86 µs.

6.2.1 Determining $\overline{\mathrm{H}}$ Production Rate from Voltage Pulses in MCP5

The voltage of MCP5 over time for a typical mixing event is shown in Figure 6.2. The arrival time of the $\overline{\mathrm{H}}$ is marked by the dashed lines. All pulses in the voltage during the $\overline{\mathrm{H}}$ arrival window are evaluated using the *scipy.signal.find_peaks* command in python [42]. Comparing the pulse height distribution for mixing and background runs should show more higher pulses for the mixing events than the background events. Each $\overline{\mathrm{H}}$ should produce one pulse in MCP5, so by counting the difference in the number of pulses above a certain threshold between mixing and background runs, we get the number of $\overline{\mathrm{H}}$ produced. This threshold can be determined by looking at the pulse height distributions of mixing and background event and choosing the voltage where the two distributions start to differ significantly.

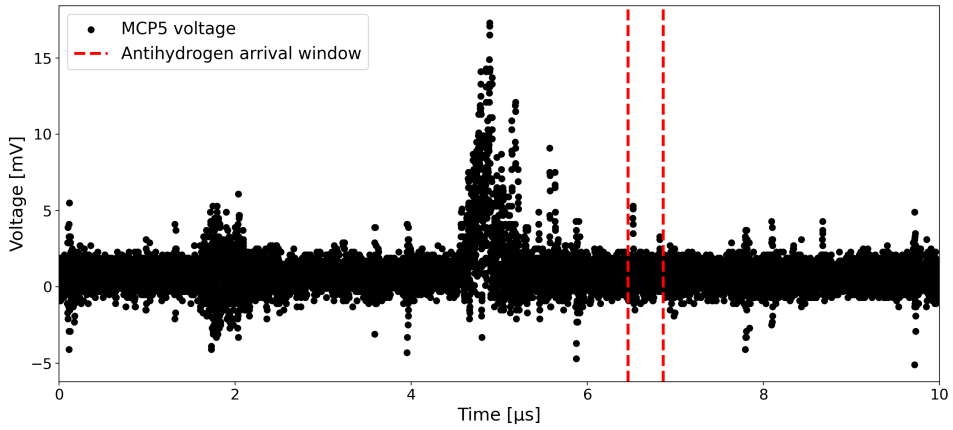

Figure 6.2: Voltage of MCP5 over time for one mixing event. The big pulse in the voltage are the majority of the pions arriving at MCP5, and the dashed lines indicate the arrival window of the antihydrogen from 6.46 µs to 6.86 µs.

6.2.2 Determining $\overline{\mathrm{H}}$ Production Rate from Clusters on MCP5

All clusters for the mixing and background events are evaluated, as described in Section 3.2, where only clusters consisting of at least 15 pixels are kept. As a first step, the average value of the pixels in the pedestal file gets subtracted from the pixels of all MCP5 images and the value of any pixel with a negative value is set to zero. The threshold that is used to search for clusters is three times the standard deviation of the pixels in the pedestal file, which is 68. The cluster charge distributions of the mixing and background runs can be compared, similar to the pulses in Section 6.2.1. The excess of cluster charges above a threshold, determined by looking at the distributions between mixing and background events, can be counted to get the number of $\overline{\mathrm{H}}$ produced.

6.3 $\overline{\mathrm{H}}$ Production Rate Results

6.3.1 $\overline{\mathrm{H}}$ Production Rate from Pulses in the Voltage of MCP5

In Figure 6.3 all pulses found in the voltage of MCP5 around the $\overline{\mathrm{H}}$ time window are shown, on the left for all mixing runs and on the right for all background runs. A clear excess of high voltage pulses within the $\overline{\mathrm{H}}$ time window is visible when comparing the mixing to the background events. The pulse height distributions for pulses within the $\overline{\mathrm{H}}$ time window over all mixing and background runs can be seen in Figure 6.4. From this figure, a threshold of 10 mV was chosen. There are 12.0 ± 3.5 pulses above the threshold in all mixing events and 6.0 ± 2.4 in all background events. As there were 468 mixing events and 776 background events, the normalized pulse number above the threshold for all background events is 3.6 ± 1.5. Consequently, there is an excess of 8.4 ± 4.0 pulses for the mixing runs with a statistical significance of 2.1 standard deviations. This means that per mixing event there were $(1.8 \pm 0.8) \times 10^{-2}$ antihydrogen detected.

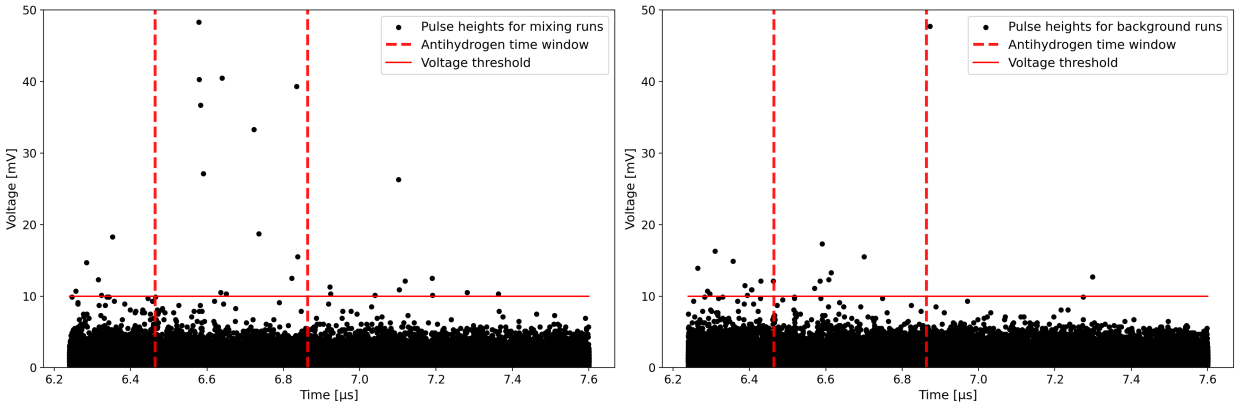

Figure 6.3: Scatter plots for all the pulses found in mixing (left) and background (right) events. The red dashed lines mark the expected window for the $\overline{\mathrm{H}}$ arrival time from 6.46 µs to 6.86 µs.

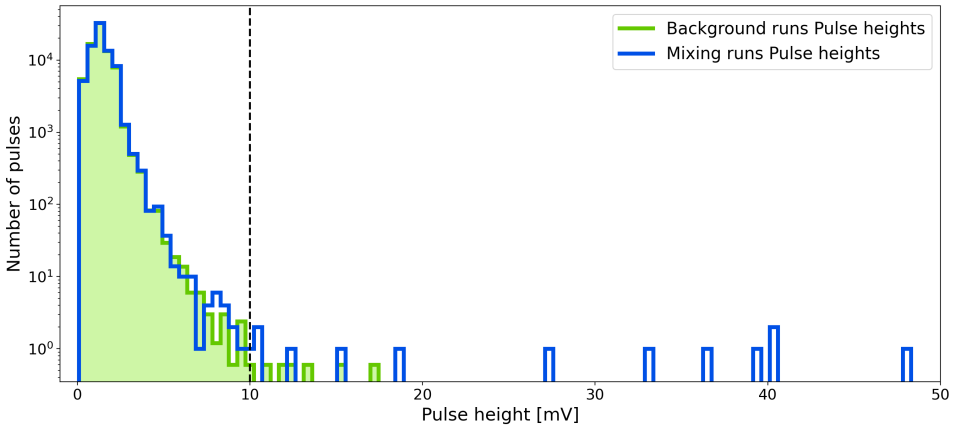

Figure 6.4: Pulse height histograms. The pulses for the background runs are depicted in green and the pulses for the mixing runs in blue. The histogram for the background runs is scaled to the one for the mixing runs by using the total beam intensity for all background and mixing runs. The dashed line at 7.5 mV marks the threshold η_p where the two histograms start to differ visibly.

If the threshold is varied over different voltages, the $\overline{\mathrm{H}}$ production rage and the statistical significance can be seen in Table 6.2.

6.3.2 $\overline{\mathrm{H}}$ Production Rate from Clusters on MCP5

The cluster charge distribution for all mixing and background events is shown in Figure 6.5. Choosing a similar threshold in the cluster charge distribution as in the pulse height distribution gives a threshold around 28 000 for the cluster charge. There are 15.0 ± 3.9 clusters with a charge above this threshold for the mixing runs and 8.0 ± 2.8 for the background runs. Normalizing the number for the background runs gives 4.8 ± 1.7. Thus, there is an excess for the mixing runs of 10.2 ± 4.5 or $(2.2 \pm 1.0) \times 10^{-2}$ per event

Threshold [mV]	N_{mix}	N_{bkg}	$\overline{\mathrm{H}}$ per event	σ_{sig}
5	102.0	88.7	$(2.9 \pm 2.7) \times 10^{-2}$	1.1
5.5	65.0	59.1	$(1.3 \pm 2.1) \times 10^{-2}$	0.6
6	46.0	34.4	$(2.5 \pm 1.7) \times 10^{-2}$	1.4
6.5	41.0	26.5	$(3.1 \pm 1.6) \times 10^{-2}$	1.9
7	31.0	18.7	$(2.6 \pm 1.4) \times 10^{-2}$	1.9
7.5	30.0	14.5	$(3.3 \pm 1.3) \times 10^{-2}$	2.5
8	22.0	10.9	$(2.4 \pm 1.1) \times 10^{-2}$	2.1
8.5	18.0	10.3	$(1.7 \pm 1.1) \times 10^{-2}$	1.6
9	15.0	7.2	$(1.7 \pm 0.9) \times 10^{-2}$	1.8
9.5	13.0	6.6	$(1.4 \pm 0.9) \times 10^{-2}$	1.5
10	12.0	3.6	$(1.8 \pm 0.8) \times 10^{-2}$	2.2
12.5	10.0	1.8	$(1.8 \pm 0.7) \times 10^{-2}$	2.5
15	9.0	1.2	$(1.7 \pm 0.7) \times 10^{-2}$	2.5
17.5	8.0	0.0	$(1.7 \pm 0.6) \times 10^{-2}$	2.8
20	7.0	0.0	$(1.5 \pm 0.6) \times 10^{-2}$	2.6

Table 6.2: $\overline{\mathrm{H}}$ production and statistical significance at different voltage thresholds. N_{mix} and N_{bkg} are the number of signals above the thresholds for the mixing and background runs. σ_{sig} is the statistical significance of the corresponding $\overline{\mathrm{H}}$ production rate.

with a statistical significance of 2.3 standard deviations. It is important to note that the images of MCP5 are generated over 1 µs and start around 6.46 µs so the production rate found this way also includes signals after the $\overline{\mathrm{p}}$ beam arrival window.

6.4 Discussion of the $\overline{\mathrm{H}}$ Production Rate

Looking at Table 6.2 it seems like the voltage threshold of 10 mV might be too high. Both the highest $\overline{\mathrm{H}}$ production rate and statistical significance are at 7.5 mV. In the cluster charge distribution in Figure 6.5 there is also an excess of clusters with lower charges than the chosen threshold of 28 000 visible for the mixing runs. However, these also include clusters after the $\overline{\mathrm{H}}$ arrival window and as can be seen in Figure 6.3 there are quite a few voltage pulses after the $\overline{\mathrm{H}}$ arrival window which correspond to some clusters found in the images. At this point, the $\overline{\mathrm{H}}$ production rate is still calculated using 10 mV as a threshold until there are more statistics available, so as to not overestimate the $\overline{\mathrm{H}}$ production.

In 2022 there were $(2.9 \pm 0.9) \times 10^{-3}$ $\overline{\mathrm{H}}$ detected per event [1], which was also replicated using the same scripts as for this analysis. Comparing this to the value for 2024 derived

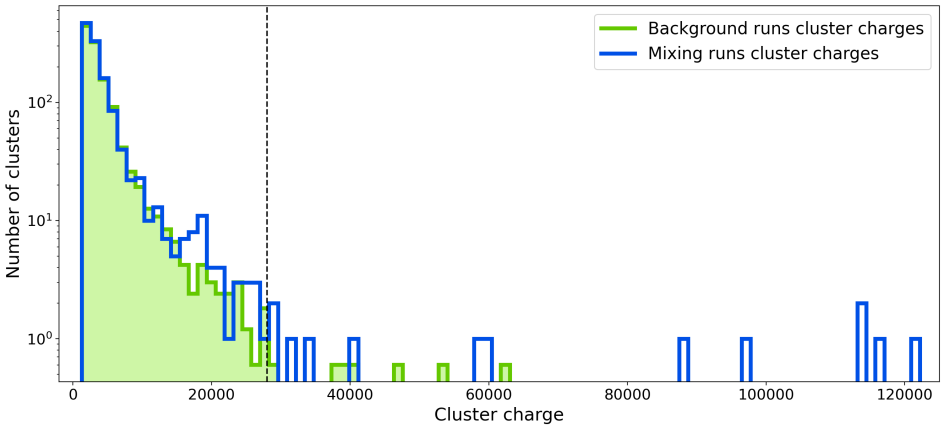

Figure 6.5: Cluster charge histograms. The pulses for the background runs are depicted in green and the pulses for the mixing runs in blue. The histogram for the background runs is scaled to the one for the mixing runs by using the number of background and mixing events. The dashed line at 28 000 marks the threshold that approximately corresponds to the threshold of 10 mV in the pulse height distributions in Figure 6.4.

in this analysis with a threshold of 10 mV gives around a six-fold increase in the number of detected $\overline{\mathrm{H}}$. If the $\overline{\mathrm{H}}$ production rate with a threshold of 7.5 mV is used around a twelve-fold increase in the $\overline{\mathrm{H}}$ detected per event is derived. Comparing the position of the threshold in the pulse height distribution for 2022 and 2024 also suggests that in 2022 a proportionally lower threshold was chosen. Thus far only 468 valid mixing events are available for 2024, compared to 6897 in 2022, so once more statistics are available for 2024 the threshold and thus the $\overline{\mathrm{H}}$ production rate will be able to be determined more accurately.

To calculate the number of $\overline{\mathrm{H}}$ produced per event using the numbers of detected $\overline{\mathrm{H}}$ per event the values for the efficiency from [1] can be used. The efficiency of the MCP to detect an $\overline{\mathrm{H}}$ is $\varepsilon_{MCP} = 0.5$. The nominal acceptance of $\overline{\mathrm{H}}$ in the detection area was estimated with simulations to be $\varepsilon_{nom} = 0.68$. The number of $\overline{\mathrm{H}}$ produced at the target position each event should thus be $(5.3 \pm 2.4) \times 10^{-2}$. This is not guaranteed to be entirely accurate though, as the efficiencies from [1] may be incorrect. At ALPHA, the efficiency of an MCP to detect an antiproton was found to be (93 ± 4) % and 58 % for a proton [20]. While this value may differ for the specific MCP used at GBAR, a detection efficiency of only 50 % seems unlikely for antiprotons. To find the distribution of the $\overline{\mathrm{H}}$ simulation with SIMION was used. This was done for the setup of 2022 and with the addition of the $\overline{\mathrm{p}}$ trap the distribution would likely be more narrow leading to a higher fraction of the $\overline{\mathrm{H}}$ hitting MCP5. To get a reliable value the simulation would have to be redone.

With $(5.3 \pm 2.4) \times 10^{-2}$ $\overline{\mathrm{H}}$ produced each event, 14 % of them are in the $2S$ state [38], so $(7.4 \pm 3.4) \times 10^{-3}$ per event. Using the Lyman alpha photon detection efficiency from Section 5.3.3 and the production rate of $\overline{\mathrm{H}}$ in the $2S$ state would lead to the expected

number of events per detected Lyman alpha photon to be over 30000. Consequentially, any measurements for the Lamb shift of antihydrogen is impossible at this point. If the Lyman alpha detector were replaced and thus a detection efficiency of the Lyman alpha photons of 16 % would be recovered, we would expect to detect a Lyman alpha photon around every 800 events. This is much better but still too high for any antihydrogen Lamb shift measurement. The $\overline{H}$ thus needs to be further improved. As already mentioned before, the number of $\overline{H}$ detected may already be higher in reality than the value in this analysis, if more statistics support lowering the voltage threshold for the pulse heights. The $\overline{H}$ production can also be further improved in 2024. The beam steering has a huge influence on how many $\overline{p}$ reach the target position in the reaction chamber, which directly correlates to the number of $\overline{H}$ produced. For the measurements analysed here, the beam steering should not have been optimal yet. The $\overline{p}$ trap setup can similarly be adjusted and further improved to reduce the beam emittance more. Another way to maximize the $\overline{H}$ production would be to change the $\overline{p}$ energy from 6 keV to 8 keV. For 6 keV, the cross-section of the $\overline{H}^+$ is maximized, but the $\overline{H}$ cross-section is around 14 % larger at 8 keV than at 6 keV [15].

Chapter 7

Conclusion

The thickness of the carbon foil was determined to be $(2.64 \pm 0.28)\,\mu g/cm^2$. With this, the scattering distribution of a H^- beam on the carbon foil was determined. This scattering distribution is not relevant for any $\overline{H}$ measurements, but it is needed to determine the detection efficiency of Lyman alpha photons from measurements with a H^- beam. Depending on what method is used to determine the scattering distribution the results differ by quite a bit. The most realistic value is obtained from [5] where the scattering of hydrogen ions with energies from 1 keV to 50 keV at carbon foils very similar to the one used at GBAR was measured. From this, a scattering half width angle of $(2.91 \pm 0.31)^\circ$ is found for the distribution. The scattering distribution was also estimated by looking at images of MCP5 with incoming neutral hydrogen scattered on the carbon foil. The distribution found this way is a bit more narrow than the one found with [5] but it would be necessary to try and replicate the results with different measurements to determine the accuracy of this distribution. For this, it would be beneficial to save the MCP5 images for further microwave scan measurements. It would also make sense to take some images of MCP5 of the charged beam, so without the carbon foil, to try and determine the centre of the beam. The centre should not change when the carbon foil is inserted, and this would make the distribution determined from the MCP5 images more reliable.

For the test of the Lamb shift system, three measurement sets were taken. One where the MWS was either off or set to a frequency of 1060 MHz and two where the MWS was scanning over different frequencies. These frequencies were from 800 MHz to 1300 MHz in steps of 100 MHz. For the MWS on and off measurements, a clear signal from Lyman alpha photons with a statistical significance of 5.6 standard deviations was detected. Using the distribution from the scattering on the carbon foil from before and the Lyman alpha signals, the probability to detect a Lyman alpha signal from one hydrogen atom in the $2S$ state passing through the Lyman alpha detector can be determined to be roughly $(4.12 \pm 1.60) \times 10^{-3}$. This is nearly 40 times lower than the predicted efficiency, which is 0.16, which was confirmed some years ago at PSI [35, 27]. Some reasons for this difference are that the algorithm searching for pulses in the MCP5 voltages is not perfect and some voltage pulses of the MCPs from Lyman alpha photons are too low and below the minimum height where the pulses can be detected. These factors could be improved by optimizing the pulses finding algorithm by decreasing the signal reflections in the

electrical circuits of the MCPs and increasing the MCP bias. The MCP bias is already set to $-2.2\,\mathrm{kV}$, and increasing this further could damage the MCPs. These factors should not be enough on their own to explain the difference in the measured and predicted efficiency. One other possibility is that the quenching efficiency in the detector is lower than predicted. A possible improvement to the detection efficiency would be to change the polarity of the voltage on the front of the MCPs in the Lyman alpha detector. Currently, this voltage is negative, meaning that electrons produced by impacts on the MCPs between channels are pushed away. Changing this to a positive voltage would mean that these electrons are pulled toward the MCPs and if they enter a channel an electron shower is started. It is also possible that the MCPs are somewhat damaged. Especially the CsI coating responsible for increasing the quantum efficiency of the MCPs might be compromised. Replacing the current Lyman alpha MCPs with new ones should result in recovering a detection efficiency around 0.16.

For the first scanning measurement, there is a large increase in the number of pulses on the MCPs over time observed. This is most likely caused by the beam trajectory and emittance changing during the measurement. The electron cooler in the ELENA ring was broken at the time of this measurement, which could be the reason for this. There were also no MCP5 images saved for these measurements. This makes it difficult to compare different MWS frequencies to each other and no significant result could be obtained. For further scanning measurements, to mitigate similar problems, the images of MCP5 could be saved. Counting the clusters in these images combined with the Lyman alpha detection efficiency and the scattering distribution should give a good estimation of how many Lyman alpha signals are expected to be observed at the different MWS frequencies, though this should be investigated further.

For the second scanning measurement, the MCP5 images were saved and the clusters on them counted. There were also events with the MWS off taken between the different frequencies. The number of detected Lyman alpha photons was determined by comparing the pulses and the number of clusters between the MWS off events and the events for each frequency that the MWS was set to. The results only look partially as expected, where mainly the number of Lyman alpha signals for the frequencies 800 MHz and 900 MHz are higher than expected. However, only few events were taken for each MWS frequency, leading to large statistical fluctuations.

The most important takeaway for further scanning measurements is that more statistics are needed for each frequency and to improve the efficiency of the Lyman alpha detector as much as possible. To improve the efficiency, the most effective short term solution would be to change the voltage on the front side of the Lyman alpha MCPs from negative to positive. It would also be beneficial to save the image of MCP5, which can be used both for the determination of the number of Lyman alpha signals and to predict

the distribution of the hydrogen scattered on the carbon foil. Once a nice lineshape is obtained from the scanning measurements, the next steps would be to take scanning measurements with the HFS on and to account for the MWS power spectrum.

There were also first measurements made for the production of antihydrogen in 2024. From these measurements, there were $(1.8 \pm 0.8) \times 10^{-2}$ antihydrogen detected per event consisting of one $\overline{p}$ spill. In 2022 the number of $\overline{H}$ detected per event was $(2.9 \pm 0.9) \times 10^{-3}$ [1], leading roughly to a six-fold increase in the $\overline{H}$ production when comparing 2024 to 2022. With the current antihydrogen production, no measurements for the antihydrogen Lamb shift can be made. Both the detection efficiency of Lyman alpha photons and the $\overline{H}$ production have to be improved. The methods to increase the Lyman alpha photon detection efficiency have already been described above. Increasing the $\overline{H}$ production is the main goal of the GBAR experiment for the remaining beam time in 2024. This can be achieved by improving the beam steering, which would increase the number of $\overline{p}$ reaching the target position. The beam steering was most likely not optimal for the measurements used in this analysis. Similarly, the parameters of the $\overline{p}$ trap can also be improved, which would result in a more focused $\overline{p}$ beam and thus more $\overline{p}$ at the target position. The $\overline{H}$ production would also improve if the number of positronium at the target position could be increased.

For further mixing runs, it would be ideal if the number of positronium in the reaction chamber could be tracked for each event. One idea for this is to have an ejection of positrons from the HFT into the reaction chamber between the $\overline{p}$ spills and measure the number of positronium for these events. The accumulation of positrons in the HFT is fast enough to allow for this. One major issue currently is that a lot of antiprotons are lost from the ejection of the $\overline{p}$ trap. This can be improved by adjusting the setup of the trap, but another possibility would be to try to eject the antiprotons from one spill in multiple bunches, and the same for the positrons, which might lead to more $\overline{p}$ reaching the reaction chamber in total.

Bibliography

[1] P. Adrich, P. Blumer, G. Caratsch, M. Chung, P. Cladé, P. Comini, P. Crivelli, O. Dalkarov, P. Debu, A. Douillet, D. Drapier, P. Froelich, N. Garroum, S. Guellati-Khelifa, J. Guyomard, P.-A. Hervieux, L. Hilico, P. Indelicato, S. Jonsell, J.-P. Karr, B. Kim, S. Kim, E.-S. Kim, Y. J. Ko, T. Kosinski, N. Kuroda, B. M. Latacz, B. Lee, H. Lee, J. Lee, E. Lim, L. Liszkay, D. Lunney, G. Manfredi, B. Mansoulié, M. Matusiak, V. Nesvizhevsky, F. Nez, S. Niang, B. Ohayon, K. Park, N. Paul, P. Pérez, C. Regenfus, S. Reynaud, C. Roumegou, J.-Y. Roussé, Y. Sacquin, G. Sadowski, J. Sarkisyan, M. Sato, F. Schmidt-Kaler, M. Staszczak, K. Szymczyk, T. A. Tanaka, B. Tuchming, B. Vallage, A. Voronin, D. P. van der Werf, A. Welker, D. Won, S. Wronka, Y. Yamazaki, K.-H. Yoo, and P. Yzombard. Production of antihydrogen atoms by 6 kev antiprotons through a positronium cloud. *The European Physical Journal C*, 83(11), November 2023.

[2] Martez Ahmadi, B. Alves, C. Baker, William Bertsche, A. Capra, Celeste Carruth, C. Cesar, M. Charlton, S. Cohen, R. Collister, S. Eriksson, Andrew Evans, Nathan Evetts, J. Fajans, T. Friesen, M. Fujiwara, David Gill, P. Granum, J. Hangst, and J. Wurtele. Investigation of the fine structure of antihydrogen. *Nature*, 578:375–380, 02 2020.

[3] Martez Ahmadi, B. Alves, C. Baker, William Bertsche, A. Capra, Celeste Carruth, C. Cesar, M. Charlton, S. Cohen, R. Collister, S. Eriksson, Andrew Evans, Nathan Evetts, J. Fajans, T. Friesen, M. Fujiwara, David Gill, J. Hangst, W. Hardy, and J. Wurtele. Characterization of the 1s–2s transition in antihydrogen. *Nature*, 557, 05 2018.

[4] Martez Ahmadi, B. Alves, C. Baker, William Bertsche, A. Capra, Celeste Carruth, C. Cesar, M. Charlton, S. Cohen, R. Collister, S. Eriksson, Andrew Evans, Nathan Evetts, J. Fajans, T. Friesen, M. Fujiwara, David Gill, J. Hangst, W. Hardy, and J. Wurtele. Observation of the 1s–2p lyman-α transition in antihydrogen. *Nature*, 561:1, 09 2018.

[5] Frédéric Allegrini, Robert W. Ebert, Georgios Nicolaou, and Guy Grubbs. Semi-empirical relationships for the energy loss and straggling of 1–50kev hydrogen ions

passing through thin carbon foils. *Nuclear Instruments and Methods in Physics Research Section B: Beam Interactions with Materials and Atoms*, 359:115–119, 2015.

[6] François Anderegg. *Rotatingwall Technique and Centrifugal Separation*, pages 221–238. WORLD SCIENTIFIC (EUROPE), 2016.

[7] Aldo Antognini, François Nez, Karsten Schuhmann, Fernando D. Amaro, François Biraben, João M. R. Cardoso, Daniel S. Covita, Andreas Dax, Satish Dhawan, Marc Diepold, Luis M. P. Fernandes, Adolf Giesen, Andrea L. Gouvea, Thomas Graf, Theodor W. Hänsch, Paul Indelicato, Lucile Julien, Cheng-Yang Kao, Paul Knowles, Franz Kottmann, Eric-Olivier Le Bigot, Yi-Wei Liu, José A. M. Lopes, Livia Ludhova, Cristina M. B. Monteiro, Françoise Mulhauser, Tobias Nebel, Paul Rabinowitz, Joaquim M. F. dos Santos, Lukas A. Schaller, Catherine Schwob, David Taqqu, João F. C. A. Veloso, Jan Vogelsang, and Randolf Pohl. Proton structure from the measurement of 2s-2p transition frequencies of muonic hydrogen. *Science*, 339(6118):417–420, 2013.

[8] The Arizona Carbon Foil Co., Inc. *Product Information*, 1 2024.

[9] H. A. Bethe. The electromagnetic shift of energy levels. *Phys. Rev.*, 72:339–341, Aug 1947.

[10] H. A. Bethe. Molière's theory of multiple scattering. *Phys. Rev.*, 89:1256–1266, Mar 1953.

[11] N. Bezginov, T. Valdez, M. Horbatsch, A. Marsman, A. C. Vutha, and E. A. Hessels. A measurement of the atomic hydrogen lamb shift and the proton charge radius. *Science*, 365(6457):1007–1012, 2019.

[12] Klaus Blaum. Cyclotron frequency in a penning trap. `https://www.physi.uni-heidelberg.de/Einrichtungen/FP/anleitungen/F47.pdf`, 10 2022.

[13] P. Blumer, M. Charlton, M. Chung, P. Cladé, P. Comini, P. Crivelli, O. Dalkarov, P. Debu, L. Dodd, A. Douillet, S. Guellati, P.-A. Hervieux, L. Hilico, A. Husson, P. Indelicato, G. Janka, S. Jonsell, J.-P. Karr, B.H. Kim, E.S. Kim, S.K. Kim, Y. Ko, T. Kosinski, N. Kuroda, B.M. Latacz, B. Lee, H. Lee, J. Lee, A.M.M. Leite, K. Lévêque, E. Lim, L. Liszkay, P. Lotrus, D. Lunney, G. Manfredi, B. Mansoulié, M. Matusiak, G. Mornacchi, V. Nesvizhevsky, F. Nez, S. Niang, R. Nishi, B. Ohayon, K. Park, N. Paul, P. Pérez, S. Procureur, B. Radics, C. Regenfus, J.-M. Reymond, S. Reynaud, J.-Y. Roussé, O. Rousselle, A. Rubbia, J. Rzadkiewicz, Y. Sacquin, F. Schmidt-Kaler, M. Staszczak, K. Szymczyk, T. Tanaka, B. Tuchming, B. Vallage, A. Voronin, D.P. van der Werf, S. Wolf, D. Won, S. Wronka, Y. Yamazaki, K.H. Yoo, P. Yzombard, and C.J. Baker. Positron accumulation in the gbar experiment. *Nuclear Instruments and Methods in Physics Research Section A: Accelerators, Spectrometers, Detectors and Associated Equipment*, 1040:167263, 2022.

[14] M. Charlton, J.J. Choi, M. Chung, P. Cladé, P. Comini, P.-P. Crépin, P. Crivelli, O. Dalkarov, P. Debu, L. Dodd, A. Douillet, S. Guellati-Khélifa, P.-A. Hervieux, L. Hilico, A. Husson, P. Indelicato, G. Janka, S. Jonsell, J.-P. Karr, B.H. Kim, E.-S. Kim, S.K. Kim, Y. Ko, T. Kosinski, N. Kuroda, B. Latacz, H. Lee, J. Lee, A.M.M. Leite, K. Lévêque, E. Lim, L. Liszkay, P. Lotrus, T. Louvradoux, D. Lunney, G. Manfredi, B. Mansoulié, M. Matusiak, G. Mornacchi, V.V. Nesvizhevsky, F. Nez, S. Niang, R. Nishi, S. Nourbaksh, K.H. Park, N. Paul, P. Pérez, S. Procureur, B. Radics, C. Regenfus, J.-M. Rey, J.-M. Reymond, S. Reynaud, J.-Y. Roussé, O. Rousselle, A. Rubbia, J. Rzadkiewicz, Y. Sacquin, F. Schmidt-Kaler, M. Staszczak, B. Tuchming, B. Vallage, A. Voronin, A. Welker, D.P. van der Werf, S. Wolf, D. Won, S. Wronka, Y. Yamazaki, and K.-H. Yoo. Positron production using a 9 mev electron linac for the gbar experiment. *Nuclear Instruments and Methods in Physics Research Section A: Accelerators, Spectrometers, Detectors and Associated Equipment*, 985:164657, 2021.

[15] P Comini and P-A Hervieux. $\bar{\mathrm{h}}^{+}$ ion production from collisions between antiprotons and excited positronium: cross sections calculations in the framework of the gbar experiment. *New Journal of Physics*, 15(9):095022, sep 2013.

[16] Pauline Comini, Paul-Antoine Hervieux, and François Biraben. H^+ production from collisions between positronium and kev antiprotons for gbar. *Hyperfine Interactions*, 228:159–165, 10 2014.

[17] Richard Fitzpatrick. Introductory Quantum Mechanics, aug 10 2020. [Online; accessed 2024-09-03].

[18] G. W. Fraser, M. A. Barstow, M. J. Whiteley, and A. Wells. Enhanced soft x-ray detection efficiencies for imaging microchannel plate detectors. *Nature*, 300(5892):509–511, Dec 1982.

[19] G.W. Fraser and J.F. Pearson. Soft x-ray energy resolution with microchannel plate detectors of high quantum detection efficiency. *Nuclear Instruments and Methods in Physics Research*, 219(1):199–212, 1984.

[20] Stine Svanum Frederiksen. Counting anti-protons with an MCP-SiPM setup to determine the absolute number of anti-protons in the ALPHA experiment. 2022.

[21] H. Gao and M. Vanderhaeghen. The proton charge radius. *Reviews of Modern Physics*, 94(1), January 2022.

[22] David J. Griffiths and Darrell F. Schroeter. *Introduction to Quantum Mechanics*. Cambridge University Press, 3 edition, 2018.

[23] I.V. Hertel and C.P. Schulz. *Atoms, Molecules and Optical Physics 1: Atoms and Spectroscopy*. Graduate Texts in Physics. Springer Berlin Heidelberg, 2014.

[24] Robert Hofstadter and Robert W. McAllister. Electron scattering from the proton. *Phys. Rev.*, 98:217–218, Apr 1955.

[25] M. Horbatsch and E. A. Hessels. Tabulation of the bound-state energies of atomic hydrogen. *Phys. Rev. A*, 93:022513, Feb 2016.

[26] A. Husson, B.H. Kim, A. Welker, M. Charlton, J.J. Choi, M. Chung, P. Cladé, P. Comini, P.-P. Crépin, P. Crivelli, O. Dalkarov, P. Debu, L. Dodd, A. Douillet, S. Guellati-Khélifa, N. Garroum, P.-A. Hervieux, L. Hilico, P. Indelicato, G. Janka, S. Jonsell, J.-P. Karr, E.-S. Kim, S.K. Kim, Y. Ko, T. Kosinski, N. Kuroda, B. Latacz, H. Lee, J. Lee, A.M.M. Leite, K. Lévêque, E. Lim, L. Liszkay, P. Lotrus, D. Lunney, G. Manfredi, B. Mansoulié, M. Matusiak, G. Mornacchi, V.V. Nesvizhevsky, F. Nez, S. Niang, R. Nishi, S. Nourbaksh, K.H. Park, N. Paul, P. Pérez, S. Procureur, B. Radics, C. Regenfus, J.-M. Reymond, S. Reynaud, J.-Y. Roussé, O. Rousselle, A. Rubbia, J. Rzadkiewicz, Y. Sacquin, F. Schmidt-Kaler, M. Staszczak, B. Tuchming, B. Vallage, A. Voronin, D.P. van der Werf, S. Wolf, D. Won, S. Wronka, Y. Yamazaki, and K.-H. Yoo. A pulsed high-voltage decelerator system to deliver low-energy antiprotons. *Nuclear Instruments and Methods in Physics Research Section A: Accelerators, Spectrometers, Detectors and Associated Equipment*, 1002:165245, 2021.

[27] G Janka, B Ohayon, Z Burkley, L Gerchow, N Kuroda, X Ni, R Nishi, Z Salman, A Suter, M Tuzi, C Vigo, T Prokscha, and P Crivelli. Intense beam of metastable muonium. *Eur. Phys. J. C Part. Fields*, 80(9):804, September 2020.

[28] Gianluca Janka. *Lamb Shift of Exotic Atoms: Precision Measurement in Muonium and Progress Towards the First Direct Determination in Antihydrogen*. Doctoral thesis, ETH Zurich, Zurich, 2022.

[29] Henri Jussila, He Yang, Niko Granqvist, and Zhipei Sun. Surface plasmon resonance for characterization of large-area atomic-layer graphene film. *Optica*, 3(2):151–158, Feb 2016.

[30] G. Kim, Wan Hong, H. Woo, Jae-Kwang Kim, Chul Eum, J. Chang, and Kyu-Sik Park. Nanosecond beam bunching system. *Journal of Radioanalytical and Nuclear Chemistry - J RADIOANAL NUCL CHEM*, 271:547–552, 03 2007.

[31] Willis E. Lamb and Robert C. Retherford. Fine Structure of the Hydrogen Atom by a Microwave Method. *Phys. Rev.*, 72:241–243, 1947.

[32] G. Jordan Maclay. History and some aspects of the lamb shift. *Physics*, 2(2):105–149, 2020.

[33] L. Meyer. Plural and multiple scattering of low-energy heavy particles in solids. *physica status solidi (b)*, 44(1):253–268, 1971.

[34] W. Oelert. The elena project at cern. *Acta Physica Polonica B*, 46(1):181, 2015.

[35] B. Ohayon, G. Janka, I. Cortinovis, Z. Burkley, L. de Sousa Borges, E. Depero, A. Golovizin, X. Ni, Z. Salman, A. Suter, C. Vigo, T. Prokscha, and P. Crivelli. Precision measurement of the lamb shift in muonium. *Phys. Rev. Lett.*, 128:011802, Jan 2022.

[36] The pandas development team. pandas-dev/pandas: Pandas, February 2020.

[37] F. Pedregosa, G. Varoquaux, A. Gramfort, V. Michel, B. Thirion, O. Grisel, M. Blondel, P. Prettenhofer, R. Weiss, V. Dubourg, J. Vanderplas, A. Passos, D. Cournapeau, M. Brucher, M. Perrot, and E. Duchesnay. Scikit-learn: Machine learning in Python. *Journal of Machine Learning Research*, 12:2825–2830, 2011.

[38] C. M. Rawlins, A. S. Kadyrov, A. T. Stelbovics, I. Bray, and M. Charlton. Calculation of antihydrogen formation via antiproton scattering with excited positronium. *Phys. Rev. A*, 93:012709, Jan 2016.

[39] O. H. W. Siegmund, C. Ertley, J. V. Vallerga, E. R. Schindhelm, A. Harwit, B. T. Fleming, K. C. France, J. C. Green, S. R. McCandliss, and W. M. Harris. Microchannel plate detector technology potential for LUVOIR and HabEx. In Oswald H. Siegmund, editor, *UV, X-Ray, and Gamma-Ray Space Instrumentation for Astronomy XX*, volume 10397, page 1039711. International Society for Optics and Photonics, SPIE, 2017.

[40] T. Tanaka, Philipp Blumer, G. Janka, Ben Ohayon, Christian Regenfus, M. Asari, R. Tsukida, T. Higuchi, K. Tanaka, Paolo Crivelli, and N. Kuroda. Design of a microwave spectrometer for high-precision lamb shift spectroscopy of antihydrogen atoms. *Interactions*, 245, 03 2024.

[41] Tània Tomàs Ripollés. The size of the proton. *Dipòsit Digital de la Universitat de Barcelona*, 2019.

[42] Pauli Virtanen, Ralf Gommers, Travis E. Oliphant, Matt Haberland, Tyler Reddy, David Cournapeau, Evgeni Burovski, Pearu Peterson, Warren Weckesser, Jonathan Bright, Stéfan J. van der Walt, Matthew Brett, Joshua Wilson, K. Jarrod Millman, Nikolay Mayorov, Andrew R. J. Nelson, Eric Jones, Robert Kern, Eric Larson, C J Carey, İlhan Polat, Yu Feng, Eric W. Moore, Jake VanderPlas, Denis Laxalde, Josef Perktold, Robert Cimrman, Ian Henriksen, E. A. Quintero, Charles R. Harris, Anne M. Archibald, Antônio H. Ribeiro, Fabian Pedregosa, Paul van Mulbregt, and SciPy 1.0 Contributors. SciPy 1.0: Fundamental Algorithms for Scientific Computing in Python. *Nature Methods*, 17:261–272, 2020.

[43] M.J. Whiteley, J.F. Pearson, G.W. Fraser, and M.A. Barstow. The stability of csi-coated microchannel plate x-ray detectors. *Nuclear Instruments and Methods in Physics Research*, 224(1):287–297, 1984.

[44] W. et al. Xiong. A small proton charge radius from an electron–proton scattering experiment. *Nature*, 575(7781):147–150, 2019.

[45] Xuefei Yan, Douglas W. Higinbotham, Dipangkar Dutta, Haiyan Gao, Ashot Gasparian, Mahbub A. Khandaker, Nilanga Liyanage, Eugene Pasyuk, Chao Peng, and Weizhi Xiong. Robust extraction of the proton charge radius from electron-proton scattering data. *Phys. Rev. C*, 98:025204, Aug 2018.

[46] Kyoung-Hun Yoo, Seok-Ho Moon, Moses Chung, Dong Hwan Won, Kwan Hyung Park, Byungchan Lee, Sun Kee Kim, Eunhoon Lim, Eun-San Kim, Bong Ho Kim, Dirk van der Werf, Naofumi Kuroda, and Patrice Pérez. Design study of an antiproton trap for the gbar experiment. *Journal of Instrumentation*, 17(10):T10003, oct 2022.

Appendix

Scattering on the Carbon Foil from Meyer's Theory [33]

τ	0.2	0.4	0.6	0.8	1.0	1.2	1.4	1.6	1.8
$g_1(\tau)$	0.050	0.115	0.183	0.245	0.305	0.363	0.419	0.473	0.525
$g_2(\tau)$		1.25	0.91	0.79	0.73	0.69	0.65	0.63	0.61
τ	2.0	2.5	3.0	3.5	4.0	4.5	5.0	6.0	7.0
$g_1(\tau)$	0.575	0.689	0.799	0.905	1.01	1.10	1.19	1.37	1.54
$g_2(\tau)$	0.59	0.56	0.53	0.50	0.47	0.45	0.43	0.40	0.37
τ	8.0	9.0	10	12	14	16	18	20	
$g_1(\tau)$	1.70	1.85	1.99	2.27	2.54	2.80	3.05	3.29	
$g_2(\tau)$	0.34	0.32	0.30	0.26	0.22	0.18	0.15	0.13	

Table 1: Values of g_1 and g_2 taken from Meyer [33]. The functions are used to calculate the scattering half width angle in Equation(4.13).

η	1×10^{-4}	1.5×10^{-4}	2×10^{-4}	3×10^{-4}	4×10^{-4}	6×10^{-4}	8×10^{-4}
$f(\eta)$	0.0600	0.0696	0.0668	0.0796	0.0890	0.103	0.117
η	1×10^{-3}	1.5×10^{-3}	2×10^{-3}	3×10^{-3}	4×10^{-3}	6×10^{-3}	8×10^{-3}
$f(\eta)$	0.127	0.148	0.162	0.190	0.210	0.241	0.264
η	1×10^{-2}	1.5×10^{-2}	2×10^{-2}	3×10^{-2}	4×10^{-2}	6×10^{-2}	8×10^{-2}
$f(\eta)$	0.280	0.311	0.334	0.362	0.382	0.409	0.422
η	1×10^{-1}	1.5×10^{-1}	2×10^{-1}	3×10^{-1}	4×10^{-1}	6×10^{-1}	8×10^{-1}
$f(\eta)$	0.430	0.435	0.429	0.408	0.383	0.340	0.302
η	1	1.5	2	3	4	6	8
$f(\eta)$	0.275	0.221	0.184	0.137	0.109	0.0775	0.0605
η	10	15	20	>20			
$f(\eta)$	0.0495	0.0332	0.0250	$(2\eta)^{-1}$			

Table 2: Values of f taken from Meyer [33]. f is used to calculate $\Delta(z)$ in Equation(4.18)

$\tilde{\vartheta}$	$f_1^M(2.0, \tilde{\vartheta})$	$f_1^C(2.0, \tilde{\vartheta})$	$f_2^M(2.0, \tilde{\vartheta})$	$f_2^C(2.0, \tilde{\vartheta})$
0	2.71	2.67	2.75	2.86
0.4	1.87	1.84	5.85×10^{-1}	5.63×10^{-1}
0.8	8.23×10^{-1}	8.10×10^{-1}	-2.71×10^{-1}	-2.45×10^{-1}
1.2	3.19×10^{-1}	3.23×10^{-1}	-1.01×10^{-1}	-1.06×10^{-1}
1.6	1.33×10^{-1}	1.38×10^{-1}	-2.33×10^{-2}	-2.08×10^{-2}
2.0	6.24×10^{-2}	6.42×10^{-2}	-1.2×10^{-3}	-3.74×10^{-3}
2.4	3.35×10^{-2}	3.29×10^{-2}	2.68×10^{-3}	1.40×10^{-3}
2.8	1.90×10^{-2}	1.83×10^{-2}	2.61×10^{-3}	1.37×10^{-3}
3.0	1.47×10^{-2}	1.39×10^{-2}	2.06×10^{-3}	1.04×10^{-3}

Table 3: Values for f_1 and f_2 at different reduced angles $\tilde{\vartheta}$ and constant $\tau = 2.0$. f_1^M and f_2^M are the values given by Meyer in [33] and f_1^C and f_2^C are the values calculated for this analysis.

$\tilde{\vartheta}$	$f_1^M(2.0, \tilde{\vartheta})$	$f_1^C(2.0, \tilde{\vartheta})$	$f_2^M(2.0, \tilde{\vartheta})$	$f_2^C(2.0, \tilde{\vartheta})$
0	6.21	6.17	1.18×10^{1}	1.23×10^{1}
0.2	4.85	4.82	4.65	4.54
0.4	2.73	2.71	-3.14×10^{-1}	-5.94×10^{-1}
0.6	1.40	1.38	-8.20×10^{-1}	-7.76×10^{-1}
0.8	7.22×10^{-1}	7.11×10^{-1}	-3.76×10^{-1}	-3.55×10^{-1}
1.0	3.79×10^{-1}	3.79×10^{-1}	-1.34×10^{-1}	-1.28×10^{-1}
1.2	2.02×10^{-1}	2.10×10^{-1}	-3.69×10^{-2}	-5.48×10^{-2}
1.6	7.53×10^{-2}	8.33×10^{-2}	6.3×10^{-3}	5.04×10^{-3}
2.0	3.52×10^{-2}	3.48×10^{-2}	6.6×10^{-3}	3.31×10^{-3}

Table 4: Values for f_1 and f_2 at different reduced angles $\tilde{\vartheta}$ and constant $\tau = 1.2$. f_1^M and f_2^M are the values given by Meyer in [33] and f_1^C and f_2^C are the values calculated for this analysis.

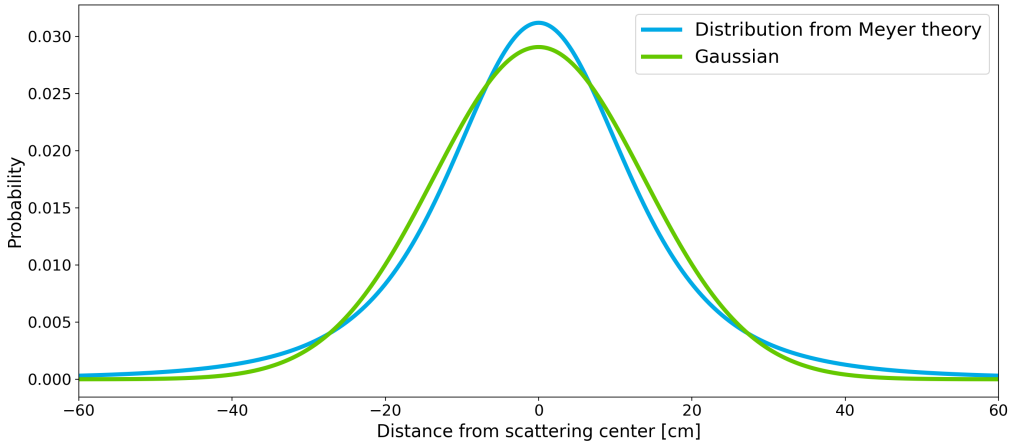

Figure 1: Comparison between the probability distribution we get when using Meyer's theory [33] in Section 4.3.2.1 and a Gaussian. Both distributions have a standard deviation of 13.7 cm.

Signals from the LEDs at the Lyman Alpha MCPs

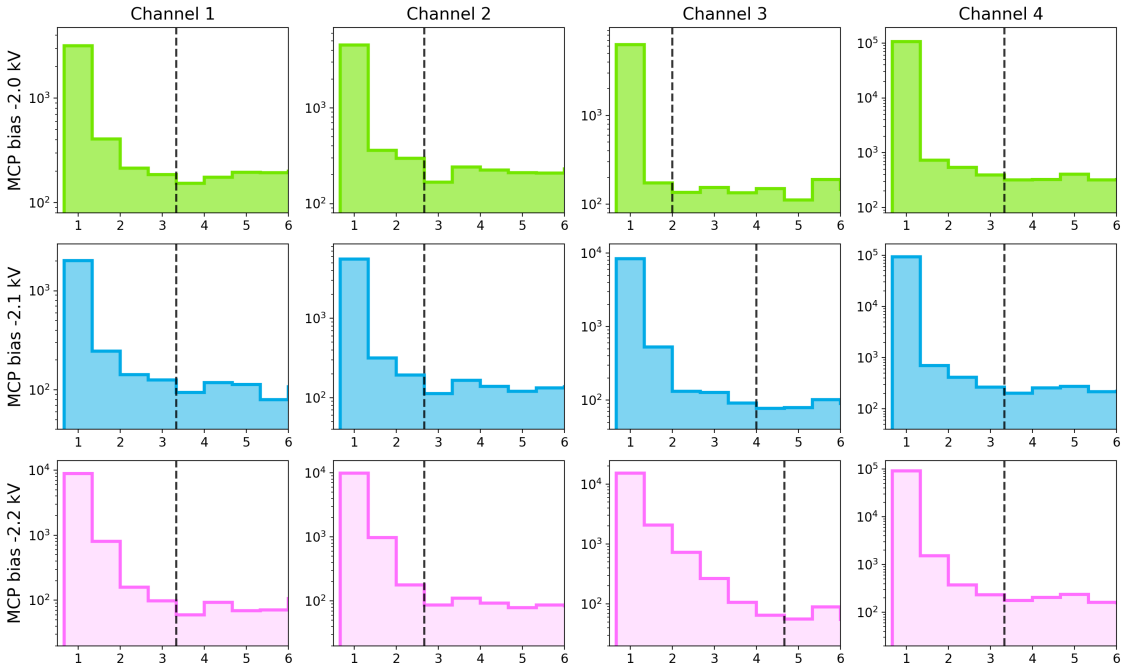

Figure 2: Pulse height distributions of the voltage of the Lyman alpha MCPs caused by 265 nm to 280 nm photons. We only look at pulses with a height lower than 6 mV. The MCP bias is at -2.0 kV for the top row, -2.1 kV for the middle row and -2.2 kV for the bottom row. The first column is for the channel 1, the second for channel 2, the third for channel 3 and the fourth for channel 4. The number of pulses drops off exponentially in the beginning of each distribution. This is because of the pulses from the noise in the voltage. The dashed line marks the spot in each distribution where this exponential decrease starts to be negligible.

Dataset 2 Plots

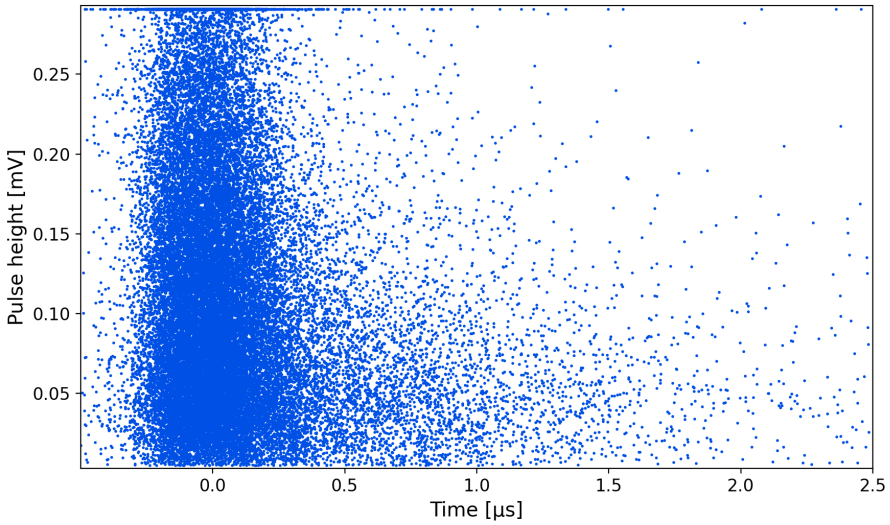

Figure 3: Scatter plot of the voltage pulses found for Dataset 2. The beam arrival can be seen as the large pulse bunch from -0.5 µs to 0.5 µs. The large number of pulses seen at the top at around 291 mV are the pulses that reach the maximum measured voltage of the MCPs. The tail of particles after the beam arrival most likely come from particles that lost a lot of energy in the carbon foil.

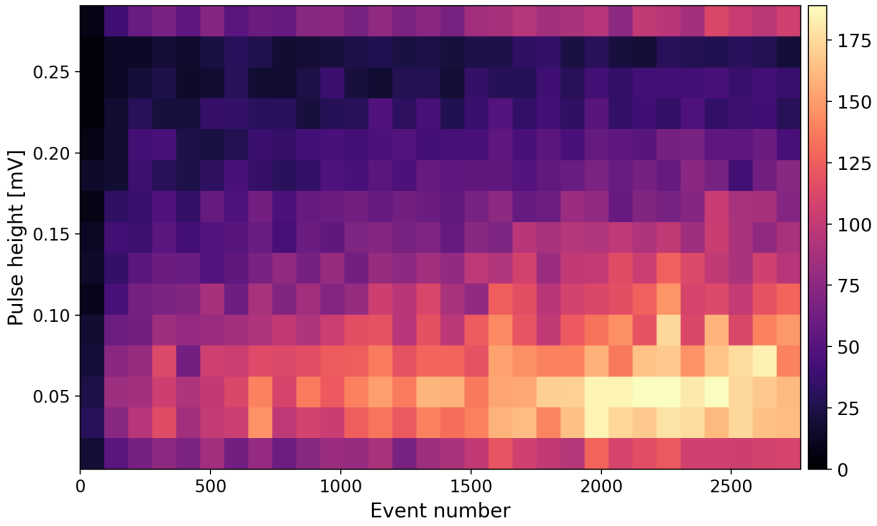

Figure 4: Two dimensional histogram with the pulses heights and the event numbers for Dataset 2. The increase in the number of pulses over time can clearly be seen. The lack of pulses at the beginning comes from mechanical problems in the experiment because of which there was no beam from around event 30 to 100.

Eidgenössische Technische Hochschule Zürich
Swiss Federal Institute of Technology Zurich

Declaration of originality

The signed declaration of originality is a component of every written paper or thesis authored during the course of studies. In consultation with the supervisor, one of the following three options must be selected:

- (●) I confirm that I authored the work in question independently and in my own words, i.e. that no one helped me to author it. Suggestions from the supervisor regarding language and content are excepted. I used no generative artificial intelligence technologies[1].
- ( ) I confirm that I authored the work in question independently and in my own words, i.e. that no one helped me to author it. Suggestions from the supervisor regarding language and content are excepted. I used and cited generative artificial intelligence technologies[2].
- ( ) I confirm that I authored the work in question independently and in my own words, i.e. that no one helped me to author it. Suggestions from the supervisor regarding language and content are excepted. I used generative artificial intelligence technologies[3]. In consultation with the supervisor, I did not cite them.

Title of paper or thesis:

Increased antiproton production in GBAR towards a first Lamb-Shift measurement in antihydrogen

Authored by:
If the work was compiled in a group, the names of all authors are required.

Last name(s):	**First name(s):**
Koller	Laurin Tim

With my signature I confirm the following:

- I have adhered to the rules set out in the Citation Guide.
- I have documented all methods, data and processes truthfully and fully.
- I have mentioned all persons who were significant facilitators of the work.

I am aware that the work may be screened electronically for originality.

Place, date	**Signature(s)**
Oberwil b. Zug, 8.9.24	L. Koller

If the work was compiled in a group, the names of all authors are required. Through their signatures they vouch jointly for the entire content of the written work.

[1] E.g. ChatGPT, DALL E 2, Google Bard
[2] E.g. ChatGPT, DALL E 2, Google Bard
[3] E.g. ChatGPT, DALL E 2, Google Bard